Neutron Scattering Study of the Cuprate Superconductor $HgBa_2CuO_{4+\delta}$

A THESIS
SUBMITTED TO THE FACULTY OF THE GRADUATE SCHOOL
OF THE UNIVERSITY OF MINNESOTA
BY

Yang Tang

IN PARTIAL FULFILLMENT OF THE REQUIREMENTS
FOR THE DEGREE OF
DOCTOR OF PHILOSOPHY

Prof. Martin Greven

August, 2018

Acknowledgements

I would like to first thank my advisor, Professor Martin Greven, for his guidance into the field of high-temperature superconductivity. I am grateful for his support of my travels to all the neutron scattering experiments, and for his encouragement during difficult times. Most importantly, I learned from him to think scientifically about fundamental physics problems, which constitues the foundation of my PhD research work.

I want to thank my University of Minnesota colleagues for their precious assistance in my research. A special thank you to Guichuan Yu, from whom I learned all the basic skills in the laboratory and data analysis techniques. I would like to express my thanks to Mun Chan, with whom I traveled to most of the neutron scattering experiments, and from whom I learned about how to design and perform the measurements. I also want to thank Wojciech Tabiś, from whom I learned X-ray scattering and transport sample preparation skills. Thank you to Neven Barišić, Yuan Li, Yangmu Li, Biqiong Yu, Zachary Anderson, and Licheng Wang for discussions about my thesis work, and to Vikram Nagarajan, Chelsey Dorow, Yang Ge, and Yang Lu for their help with the crystal growth and characterization work.

Thank you to all my collaborators at the Laboratory Léon Brillouin and Institut Laue-Langevin in France, and at Oak Ridge National Laboratory in the United States. Special thanks to Philippe Bourges and Yvan Sidis for their guidance during our neutron scattering experiments, to Lucile Mangin-Thro for her valuable comments and help with our experiments, and to Doug Abernathy for his help with the collection and analyis of our time-of-flight neutron scattering data.

Thank you to my best friends, Xin Li, Yang Luo, Qingyuan Zhao and Jiaming Zheng, for their help throughout my PhD life.

I also would like to thank my PhD committe members Allen Goldman, Andrey

Chubukov and Turan Birol, as well as the members of my oral committee, Rafael Fernandes and Chris Leighton, for their time and valuable comments.

Most importantly, thank you to my parents and Fei Chen for their love and companionship, and especially for their encouragement and support during the last year before my graduation.

Abstract

High-temperature superconductivity in the cuprates has been the subject of intense research since its discovery more than thirty years ago, yet no consensus regarding major parts of the cuprate phase diagram and the underlying superconducting pairing mechanism has been reached. One of the central issues is to clarify the interplay between superconductivity and other states, especially in the pseudogap region of the phase diagram. One of the possible pairing mechanisms involes antiferromagnetic spin fluctuations, which might furthermore drive other ordering tendencies. Another proposed mechanism involves intra-unit-cell charge currents that give rise to unusual magnetism. Consequently, there has been enormous interest in establishing the magnetic properties of the cuprates. The mercury-based compounds are ideal for such studies, as they possess the highest superconducting transition temperatures (T_c) and relatively simple tetragonal crystal structures. In this Thesis, I present a neutron scattering study of magnetic order and excitations of the simplest Hg-based cuprate, $HgBa_2CuO_{4+\delta}$, that reveals pivotal properties of the pseudogap phase.

The experimental technique that I used in this Thesis is neutron scattering, arguably the most powerful probe of the magnetic properties of materials. Single crytals were grown by a flux method developed in the Greven laboratory. A typical $HgBa_2CuO_{4+\delta}$ sample used in a neutron scattering experiment consists of 30-40 co-aligned single crystal pieces in order to achieve a large enough sample mass (and hence magnetic signal). Experiments were performed on both polarized and unpolarized triple-axis spectrometers at the Laboratoire Léon Brillouin and the Institut Laue Langevin, France, and on the time-of-flight spectrometer ARCS at the Spallation Neutron Scource, at Oak Ridge National Laboratory in Tennessee.

Chapter 1 gives a brief introduction of the history of the cuprates, with focus on their crystal structures and phase diagram, followed by an introduction to the neutron scattering technique. Chapter 2 contains experimental details relevant to this Thesis, including crystal growth, sample preparation, and neutron scattering data analysis procedures. The last three Chapters contain research results for the magnetic properties of the model cuprate $HgBa_2CuO_{4+\delta}$. Chapter 3 reports on the antiferromagnetic response,

which features a doping-dependent Y-shaped dispersion, a resonance feature, and an excitation gap. Chapter 4 reports on the measurement of intra-unit-cell magnetic order with unprecedented quantitative analysis and, in particular, on the spatial orientation of the magnetic moments. Finally, Chapter 5 presents a detailed study of the doping- and momentum-dependence of an unusual dispersionless excitation that previously was believed to be associated with the intra-unit-cell magnetism. In each of the latter three Chapters, possible microscopic explanations of our observations are discussed.

Contents

List of Tables

List of Figures

Chapter 1

Introduction

This Chapter contains a brief introduction to high-temperature superconductors in general, and to the Hg-based cuprates in particular, followed by an introduction to neutron scattering, the experimental technique used in this Thesis to study the mercury-based cuprate $HgBa_2CuO_{4+\delta}$.

1.1 The Cuprates

1.1.1 High-Temperature Superconductors

Superconductivity was first discovered in 1911 by Heike Kamerlingh Onnes, who observed that the resistance of the metal mercury (Hg) becomes immeasurably small below a temperature of approximately 4.2 K [1]. The phenomenon of superconductivity should be distinguished from the concept of a perfect conductor with zero resistance. Importantly, a perfect conductor does not exhibit the Meissner-Ochsenfeld effect, discovered in 1933 by Walther Meissner and Robert Ochsenfeld [2]. This effect, also known as perfect diamagnetism, is the phenomenon by which a superconductor expels an externally applied magnetic field.

Conventional superconductivity, as it occurs in ordinary metals such as Hg, was subsequently explained in the 1950s by John Bardeen, Leon Cooper and John Schrieffer (often referred to as the BCS theory) [4]. In their model, electrons are coupled by phonons (the quantized vibrations of the crystal lattice) to form Cooper pairs. As a

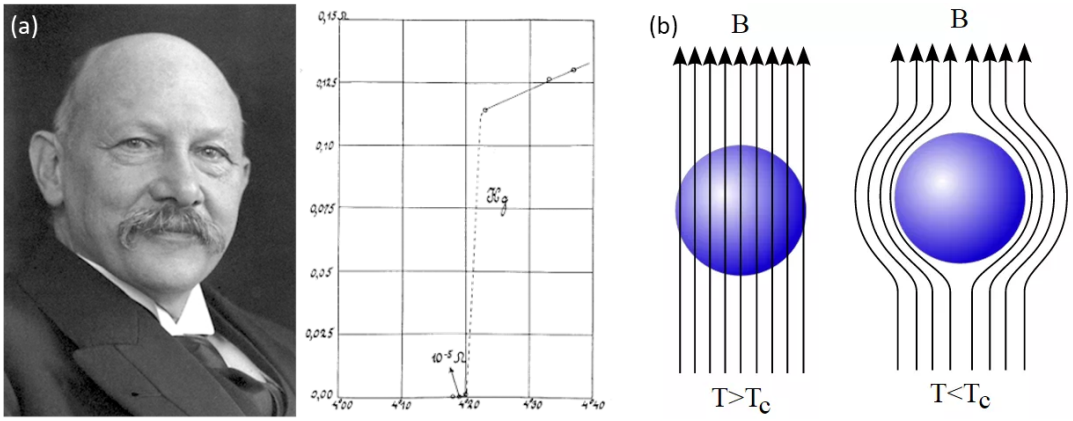

Figure 1.1: *Defining characteristics of superconductors [3]. (a) Heike Kamerlingh Onnes discovered that the electrical resistivity of elementary mercury becomes immeasurably small below a characteristic temperature, referred to as the superconducting transition temperature T_c. (b) Schematic of the Meissner-Ochsenfeld effect, by which a superconductor expels an externally-applied magnetic field.*

result, two spin-1/2 electrons which individually obey Fermi-Dirac statistics form an integer-spin electron pair which obeys Bose-Einstein statistics. As bosonic pairs, they can then condense into a macroscopic coherent superconducting state below a critical transition temperature, T_c. The magnitude of T_c is directly proportional to the energy gap between the superconducting ground state energy and the non-superconducting normal state, which was estimated as $\Delta_c \approx 2\hbar\omega_D e^{-1/(V_0 N(0))}$, where ω_D is the Debye phonon cutoff energy, $N(0)$ the electronic density of states at the Fermi level, and V_0 the electron-phonon coupling potential [4]. The transition temperature was estimated to have an upper bound of approximately 30 K within the adiabatic approximation. Exceptions can occur when there are very light atoms in the system (such as the H atom in H_2S), and then T_c is proportional to the square root of the coupling potential [5] and may exceed this limit (e.g., H_2S was discovered in 2015 to have $T_c \approx 203$ K at an extremely high pressure of 155 GPa [6]). Importantly, one needs to distinguish between the BCS theory and the BCS pairing mechanism: the former only states that Cooper pairs may form if there is an attractive interaction between electrons close to the Fermi surface, whereas the latter specifies that the pairs are formed due to electron-phonon

coupling.

An astonishing discovery was made by J. G. Bednorz and K. A. Müller in the 1980s [8], when they observed superconductivity in the complex oxide La-Ba-Cu-O with $T_c \approx 30$ K. This compound has a lamellar structure similar to that of perovskites. Related oxides were known to be poor conductors of electricity. In the following years, numerous such complex oxide superconductors were discovered, many with T_c values above the boiling point of nitrogen (77 K). These unexpected high T_c values, and the fact that liquid nitrogen is a very cheap coolant, triggered a tremendous amount of scientific and technological activities. The discovery by Bednorz and Müller was awarded the 1987 Nobel Prize in Physics and is considered one of the greatest scientific achievements of the past half-century [7]. There exist a number of other families of superconductors, such as the iron pnictides, and the heavy-fermion and organic superconductors (Figure 1.2) [9]. Many of these materials do not appear to be conventional superconductors, i.e., they cannot be described by the BCS phonon-based pairing mechanism, and it has been argued by many that BCS theory may not be applicable either. Among all of these unconventional superconductors, the cuprates possess the highest transition temperatures at ambient pressure, with T_c as high as 135 K (163 K under 30 GPa pressure) for $HgBa_2Ca_2Cu_3O_{8+\delta}$.

1.1.2 Crystal Structures

There exist well over 100 cuprate superconductors, and all of these complex oxides share a common structural unit: the two-dimensional CuO_2 plane (Figure 1.3). The planes are stacked and connected by intervening layers of other atoms (e.g., mercury, yitrium, barium, oxygen). The CuO_2 planes can be 'doped' with charge carriers via the introduction of interstitial atoms (typically oxygen) or via substitution of atoms in the intervening layers. For some cuprate families that share the same intervening layer, the number n of adjacent CuO_2 layers can vary; these compounds are referred to as n-layer cuprates. Usually T_c increases within the same cuprate family as n increases up to $n = 3$, and then decrease. For example, the one-, two- and three-layer Hg-based compounds have the chemical formulas $HgBa_2CuO_{4+\delta}$ (Hg1201), $HgBa_2CaCu_2O_{6+\delta}$ (Hg1212) and $HgBa_2Ca_2Cu_3O_{8+\delta}$ (Hg1223), and their maximum T_c at ambient pressure increases as 96 K, 126 K and 135 K, and then decreases for $n > 3$.

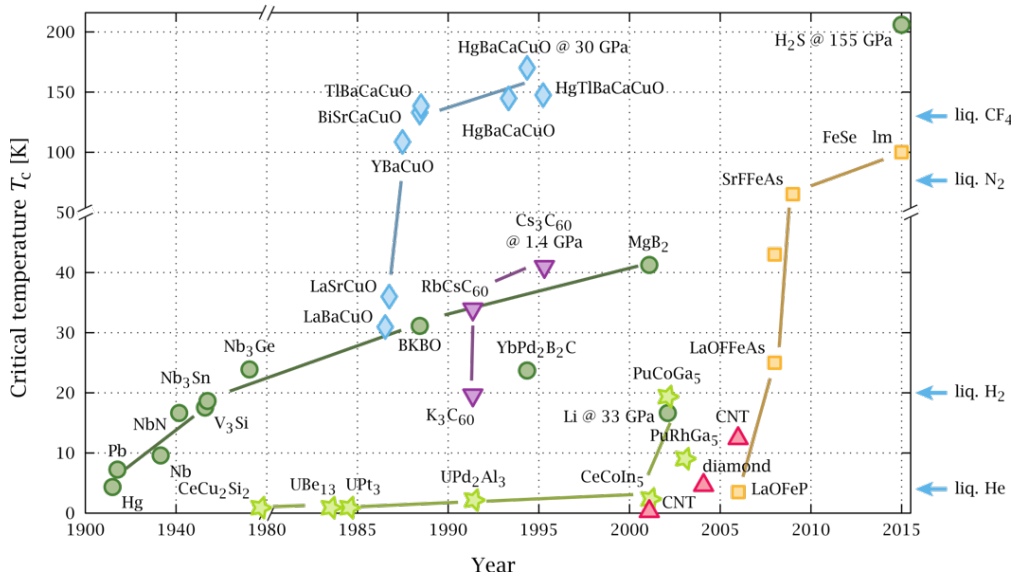

Figure 1.2: *Timeline of the discovery of superconducting materials [9]. Green circles, blue diamonds, yellow rectangles, green stars and purple triangles represent conventional superconductors, cuprates, iron pnictides, heavy fermion and organic superconductors. Among all these materials, the cuprates feature the highest transition temperature at atmospheric pressure (T_c =135 K) [10].*

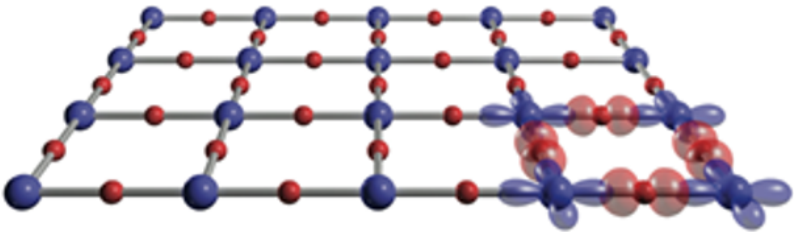

Figure 1.3: *Schematic of the* CuO_2 *plane. Blue and red spheres represent the Cu and O atoms, respectively. The overlap of the Cu* $3d_{x^2-y^2}$ *and O* $2p_{x,y}$ *electronic orbitals is illustrated in the right bottom corner.*

Figure 1.4 tabulates the most well-known cuprate compounds based on the number of CuO_2 layers (up to $n = 3$) and the position of the dopant/primary disorder site [11].

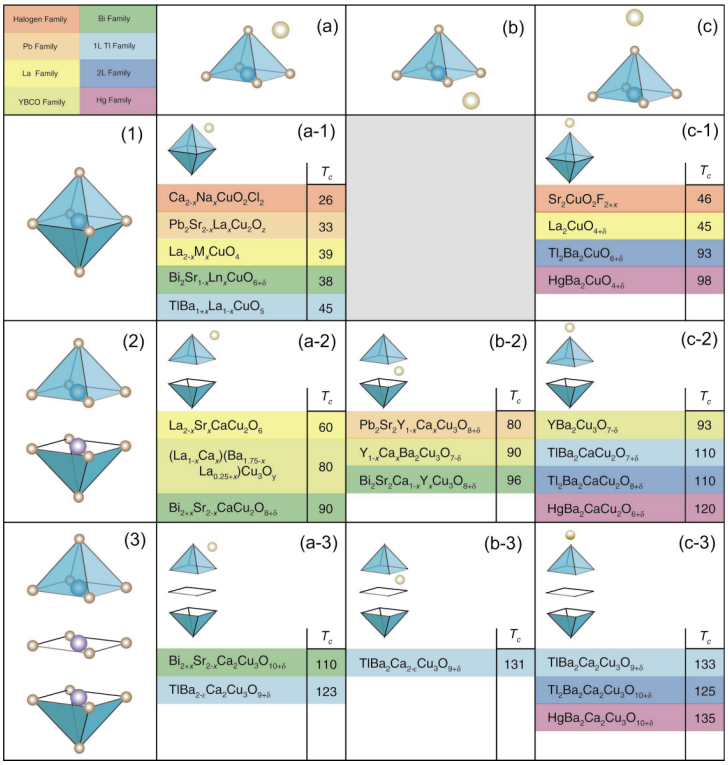

Figure 1.4: *Tabulation of structures and disorder types of cuprate superconductors [11]. Rows correspond to the number (n) of* CuO_2 *layers per primitive cell. Columns correspond to the most prevalent dopant-disorder type: (a) close to the apical oxygen atom, (b) between adjacent* CuO_2 *planes, and (c) relatively far away from the* CuO_2 *planes. Hg1201 is a single-*CuO_2*-layer cuprate (n = 1) and lies in category c-1, Hg1212 (n = 2) lies in c-2, and Hg1223 (n = 3), the cuprate with the highest optimal* T_c*, lies in c-3.*

Two of the most commonly studied compounds are $La_{2-x}M_xCuO_4$ (where M is alkaline earth element: Sr, Ca, Ba) and $YBa_2Cu_3O_{6+\delta}$ (YBCO).

1.1.3 Temperature-Doping Phase Diagram

The electronic properties of the cuprates are heavily influenced by the excess charge-carrier density p introduced via doping. In the undoped state ($p = 0$), the in-plane Cu^{2+} $3d_{x^2-y^2}$ obital is occupied by nine out of a possible total of ten electrons, giving rise to

a single unpaired electron. This missing electron is referred to as a hole. Conventional band theory of materials therefore predicts the existence of a half-filled conducting band, i.e., the undoped cuprates should be good metals. However, it turns out that they are very good insulators when undoped. This contradiction indicates the need for strong Coulomb interactions to be considered. The resulting insulator can be classified as a Mott-insulator or, more accurately, a charge-transfer insulator [17]. Moreover, the localized hole in the undoped cuprates has a spin-1/2 magnetic moment, and the system exhibits long-range antiferromagnetic (AF) order below about room temperature (the Cu spins are aligned anti-parallel to their nearest neighbors).

Upon doping the CuO_2 planes, the long-range AF order is quickly destroyed, and other phases emerge, including the superconducting phase. Instead of doping with holes, it is also possible to achieve superconductivity by introducing excess electrons into the CuO_2 planes. The former tend to reside on the planar oxygen orbitals, whereas the latter predominantly reside on copper. Depending on whether the introduced carriers are electrons or holes, the cuprates are referred to as electron- or hole-doped. In this Thesis, we focus on the hole-doped side of the phase diagram, which is shown in Figure 1.5 [7]. When p is zero, the system is an AF Mott-insulator, as discussed. As p increases, the system first exhibits the mysterious pseudogap (PG) phase characterized by a partial gap and the depletion of electronic states at the Fermi surface, and by various seemingly intertwined ordered states, including charge-density-wave (CDW), spin-density-wave (SDW), charge-spin stripe, and superconductivity (SC). At even higher doping, the system enters the so-called strange metal (SM) regime at temperatures above the SC phase, where peculiar T-linear planar resistivity dependence is observed. Finally, the system becomes a normal Fermi-liquid metal above $p \approx 0.3$. Evidence for Fermi-liquid charge transport also exists deep in the PG phase [12–16].

1.1.4 Basic Theoretical Approches

It is widely believed that the remarkable properties of the cuprates are rooted in the properties of the doped CuO_2 plane. Therefore, understanding the electronic structure of the CuO_2 planes is thought to hold the key to solving the 'high-T_c problem'. The electronic band structure of the cuprates near the Fermi energy involves hybridization of the planar Cu^{2+} $3d_{x^2-y^2}$ and O^{2-} $2p_{x,y}$ orbitals (see Figure 1.3). At zero doping, since

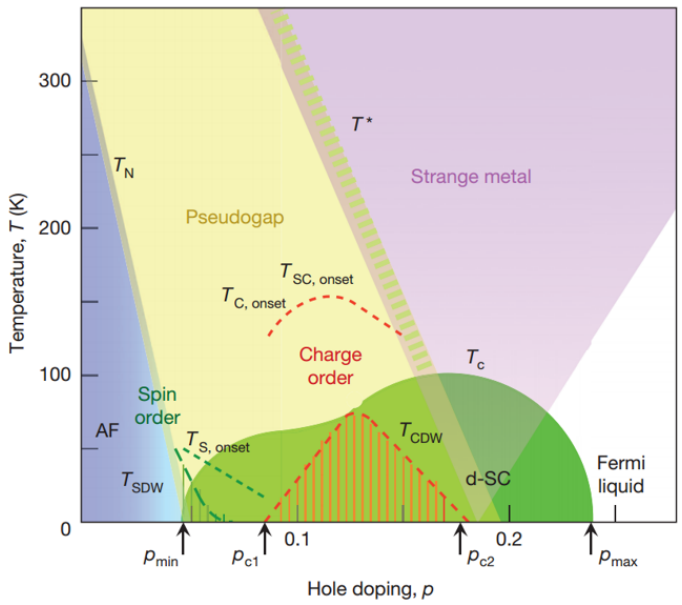

Figure 1.5: *Phase diagram of hole-doped cuprates [7]. Principal phases are marked in blue (antiferromagnetic), yellow (pseudogap), green (superconductivity) and purple (strange metal), with characteristic temperatures T_N, T^* and T_c marked at the boundaries. The undoped materials are Mott insulators, whereas at high hole-doping levels p they exhibit seemingly conventional Fermi-liquid metallic behavior. The spin-density-wave (SDW) and charge-density-wave (CDW) ordered states with characteristic temperatures T_{SDW} and T_{CDW} are indicated by green and red hatched areas. The SC phase emerges above $p_{min} \approx 0.05$ and vanishes at $p_{max} \approx 0.28$.*

the $3d_{x^2-y^2}$ orbital is occupied by a single electron, the conduction band is expected to be half-filled and the system should be a good metal based on the band theory described in standard solid-state physics textbooks such as [18]. Indeed, using a local density approximation (LDA) calculation of the band structure of undoped La_2CuO_4 (LCO), Mattheiss pointed out that the bands near the Fermi surface can be idenfied as bonding (B), nonbonding (NB) and antibonding(AB) bands, in the order of their energy scales. The Fermi energy intersects in the middle of the AB band, so LCO should be a metal (see Figure 1.6a) [19].

However, it turns out that LCO is a very good insulator. This stark discrepancy

arises due to the fact that, although two electrons in the antibonding band could be at the same site with antiparallel spin directions, which is allowed by the Pauli exclusion principle, their strong Coulomb repulsion (U) is an even larger energy scale than the width of the antibonding band itself. Within the Hubbard model, once U is taken into consideration, the calculated antibonding band separates into two bands: the upper and lower Hubbard band, denoted UHB and LHB, respectively, each with half the number of electronic states of the non-interacting band (see Figure 1.6c). Therefore, the Cu $3d$ electrons will fully fill the LHB and leave the UHB empty, and the system is an insulator. Strictly, the undoped cuprates are classified as charge-transfer insulators rather than Mott insulators [17]. The difference is that the gap between bands in the former case arises from the hybridization of different cation and anion orbitals, such as Cu $3d$ and O $2p$ in the case of cuprates, whereas in the latter it is due to hybridization within the same atom, such as V $4p$ and $3d$ orbitals in V_2O_3. The charge-transfer gap Δ usually is much smaller than U (see Figure 1.6b,c).

A model that considers all the three planar orbitals mentioned above (Cu $3d_{x^2-y^2}$, O $2p_{x,y}$) and strong electron-electron interactions is the three-band model firstly introduced by Emery to the high-T_c problem [20], in which the Hamiltonian is written as

$$H \;=\; \sum_{i,j,\sigma} \epsilon_{ij} c^{+}_{i\sigma} c_{j\sigma} \;+\; \frac{1}{2} \sum_{i,j,\sigma,\sigma'} U_{ij} c^{+}_{i\sigma} c_{i\sigma} c^{+}_{j\sigma'} c_{j\sigma'}, \tag{1.1}$$

where i and j label neighboring copper or oxygen sites, σ and σ' label spin states, the operators $c^{+}_{i\sigma}$ and $c_{i\sigma}$ create and annihilate holes with spin σ at site i, respectively, and ϵ_{ij} and U_{ij} are the hopping and interaction energies, respectively, between electrons on sites i and j. Although this model considers all three orbitals, it is very complicated and currently not solvable. It was suggested by Anderson [21] that one can effectively consider only the Cu $3d$ orbital, reducing Eq. 1.1 to the one-band Hubbard model,

$$H \;=\; -t \sum_{i,j,\sigma} c^{+}_{i\sigma} c_{j\sigma} \;+\; U \sum_{i} n_{i\sigma} n_{i\sigma'}, \tag{1.2}$$

where t and U are the hopping and interaction energies between nearest-neighbor sites, and $n_{i\sigma} \;=\; c^{+}_{i\sigma} c_{i\sigma}$ is the number operator. In this model, the cuprates are effectively

described as doped Mott-insulators, and the Zhang-Rice singlet band acts as the LHB (see Figure 1.6d) [22].

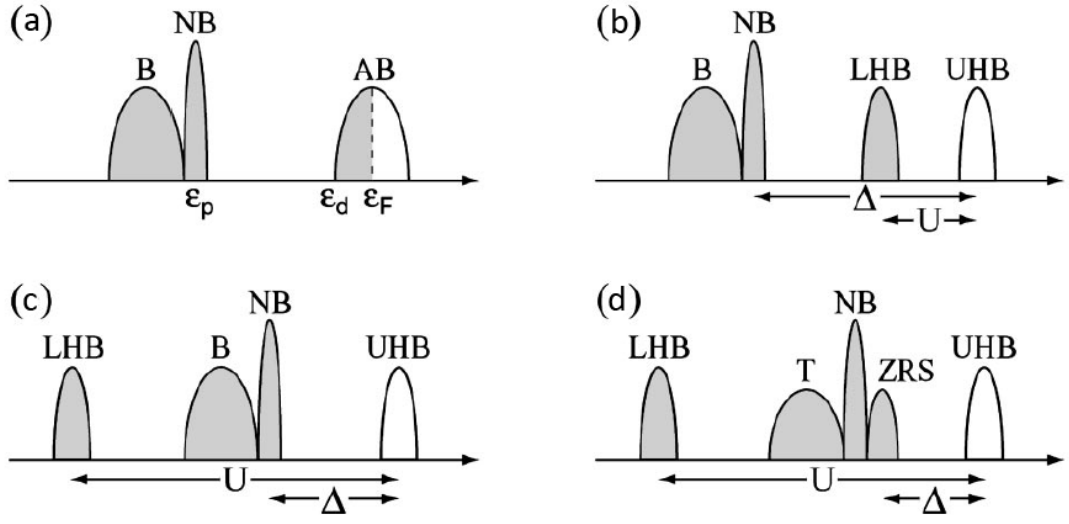

Figure 1.6: *Schematic of band structure. (a) The bonding (B), nonbonding (NB) and antibonding (AB) bands for the CuO_2 plane in the non-interacting limit, as discussed in [19]. (b)-(c) AB band split into lower and upper Hubbard bands (LHB and UHB), (b) with a gap energy scale U smaller than the difference Δ between NB and UHB in the case of the Mott-insulator, and (c) $U > \Delta$ in the case of the charge-transfer insulator. (d) NB splits into triplet and Zhang-Rice singlet states as calculated for the one-band Hubbard model. [23]*

In the strong-coupling limit ($U \gg t$), the doubly-occupied states, in which two electrons with antiparallel spins occupy the same site, are explicitly excluded from the Hilbert space of the one-band Hubbard model, and the Hamiltonian can be further simplified to the t-J model,

$$H = -t\sum_{i,j,\sigma}\widetilde{c}^{+}_{i\sigma}\widetilde{c}_{j\sigma} + J\sum_{i,j}\left(S_i\cdot S_j - \frac{n_i n_j}{4}\right), \tag{1.3}$$

where $\widetilde{c}_{i\sigma} = c_{i\sigma}\left(1-n_{i,-\sigma}\right)$ excludes the doubly-occupied states, $J = 4t^2/U$ is the nearest-neighbor antiferromagnetic exchange energy, and S_i is the electron spin operator

at site i. Both the one-band Hubbard model and the t-J model are widely used in theoretical calculations of the physical properties of the cuprates. A detailed derivation of the t-J model from the Hubbard model can be found in [24].

With these models, theoretical physicists have worked to describe the experimental observations for the cuprates and the phases discussed in the previous Section. In a 2012 review paper, Scalapino summarized the properties of AF spin fluctuations, pseudogap behavior, nematic correlations and stripes based on calculations for the one-band Hubbard and t-J models [25]. Importantly, he discussed an unconventional d-wave pairing mechanism that involves spin fluctuations as the superconducting pairing glue [25]. This is important in light of the fact that the superconducting order parameter of the cuprates has d-wave rather than conventional s-wave symmetry [7]. This magnetic pairing glue proposal dates back to 1973 [26], i.e., it predates the 1986 discovery by Bednorz and Müller, and inspired considerable theoretical and experimental efforts to understand the magnetic properties of the cuprates and to establish the connection between the magnetic degrees of freedom and the phases discussed in Section 1.1.4. On the experimental side, this has involved a wealth of magnetic neutron scattering studies [7,27–29]. In a relatively recent theoretical development, using the t-J model, Sachdev and colleagues [30] proposed that the AF fluctuations might drive density-wave order. Wang and Chubukov [31] subsequently confirmed this by showing that AF fluctuations can give rise to charge-density-wave (CDW) order. Together with the fact that existing neutron scattering studies have revealed considerable differences for the AF response of the most commonly studied cuprates $La_{2-x}Sr_xCuO_4$ and $YBa_2Cu_3O_{6+\delta}$ (especially below 60 meV), these and related theoretical findings motivated the work in Chapter 3. There exist numerous theoretical proposals for the cuprate phase diagram [32]. For example, Varma [33,34] proposed the existence of loop current order and associated translational symmetry preserving intra-unit-cell (IUC, or $\mathbf{q} = 0$) magnetic order. Fechner and colleagues [35], partially motivated by the work of Lovesey [36,37], predict a different type of translational-symmetry-preserving mechanism that involves electro-magnetic multipoles. Neutron diffraction experiments have indeed revealed the universal existence of IUC magnetic order in the PG state [38,39], and the spatial orientation the magnetic moments in Hg1201 is determined with unprecedent precision in Chapter 4. Varma predicted two collective modes associated with the IUC magnetic order [40,41], thought

to be the Ising-like modes observed in Hg1201 by neutron scattering [42, 43], which motivated the work in Chapter 5.

1.2 Neutron Scattering

1.2.1 Introduction

Following early experiments, such as the study of the antiferromagnetic order in MnO [44], neutron scattering quickly developed into one of the most commonly used probes of the magnetic properties of materials. Due to the fact that a neutron has spin, it is sensitive to the magnetic field inside materials. Magnetic neutron scattering is the most powerful probe of magnetic order and excitations in materials. Moreover, neutrons also interact with nuclei via the strong force, which makes them an ideal probe of crystal structures and lattice vibrations (phonons). Examples of the utility of neutron scattering include studies of structure of protein molecules, Li-based batteries and magnetic properties of semiconductor materials [45, 46].

From a quantum mechanical perspective, the neutron is both a particle and a wave. Modern neutron sources are broadly divided into three groups depending on the energy/wavelength range of the generated neutrons (see Table 1.1). The connection between neutron velocity (v), kinetic energy (E), wavevector (k), wavelength (λ) and temperature (T) is as follows:

$$\begin{aligned} E &= \frac{1}{2}m_n v^2 = k_B T = \frac{(\hbar k)^2}{2m_n}, \\ k &= \frac{2\pi}{\lambda} = \frac{m_n v}{\hbar}, \end{aligned} \tag{1.4}$$

where m_n is the neutron mass, k_B is the Boltzmann constant, and $\hbar$ is the Planck constant. The neutron interacts with materials via the strong force and the electromagnetic force. As neutrons are not sensitive to charge or electric fields, they can have a penetration depth as large as several centimeters, which is extremely desirable in the study of the bulk properties of materials. A typical neutron scattering process is shown in Figure 1.7. Assuming that the energy and momentum of incident and final (scattered) neutrons are (E_i,$\mathbf{k}_i$) and (E_f,$\mathbf{k}_f$), respectively, then due to the energy and momentum

conservation laws, the energy (typically written as $\hbar\omega$ or simply ω) and momentum ($\mathbf{Q}$) that a neutron transfers to a sample are described by $E = \hbar\omega = E_f - E_i$ and $\mathbf{Q} = \mathbf{k}_f - \mathbf{k}_i$. For example, if neutrons are scattered by phonons, then the energy and momentun transfer (ω,$\mathbf{Q}$) at which scattered neutrons are detected correspond to the dispersion relation of phonons.

Table 1.1: *Cold, thermal and hot neutrons.*

Neutron source	Energy (meV)	Temperature (K)	Wavelength (nm)
Cold	0.1 - 10	1 - 120	0.4 - 3
Thermal	5 - 100	60 - 1000	0.1 - 0.4
Hot	100 - 500	1000 - 6000	0.04 - 0.1

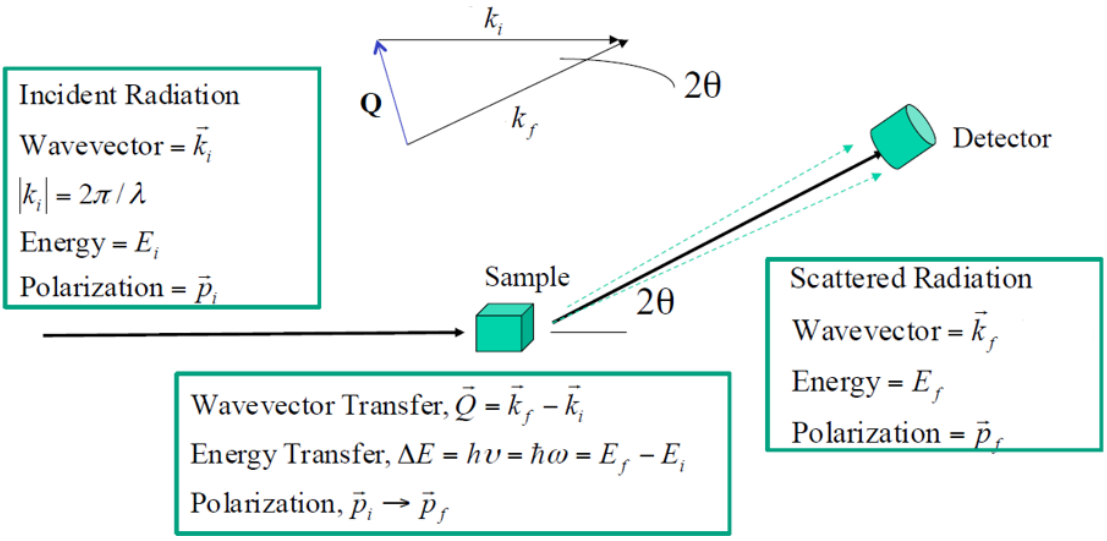

Figure 1.7: *Neutron scattering schematic. Neutrons with incident energy E_i and wavevector $\mathbf{k}_i$ interact with a sample and get scattered, which changes their energy and momentum. They reach the detector with a final energy E_f and wavevector $\mathbf{k}_f$. The scattering angle, defined as the angle between $\mathbf{k}_i$ and $\mathbf{k}_f$, is denoted as 2θ. In a polarized-neutron scattering experiment, one also specifies the incident ($\mathbf{p}_i$ or λ_i) and final ($\mathbf{p}_f$ or λ_f) polarization states.*

1.2.2 Scattering Cross Section

Given a constant incident flux ϕ of neutrons with momentum k_i, we are interested in how many neutrons scatter into a given solid angle $d\Omega$, in the direction of the final mometum $\mathbf{k}_f$, with a final energy between E_f and $E_f + dE_f$. This is defined as the partial differential scattering cross section. In this Section, we will introduce some useful equations and concepts regarding the neutron scattering cross section. A more detailed tutorial can be found in [47]. In this Thesis, we denote the momentum transfer by $\mathbf{Q} \equiv (H, K, L) \equiv H\mathbf{a}^* + K\mathbf{b}^* + L\mathbf{c}^*$, where $a^* = \frac{2\pi}{a}$, $b^* = \frac{2\pi}{b}$, and $c^* = \frac{2\pi}{c}$ are the reciprocal lattice constants. Since the crystal structure of $HgBa_2CuO_{4+\delta}$ is tetragonal, the a and b crystallographic directions are equivalent, so $a = b$ and $a^* = b^*$.

The scattering cross section can be obtained from Fermi's Golden Rule,

$$\frac{d^2\sigma}{d\Omega dE_f} = \frac{k_f}{k_f}\left(\frac{m_n}{2\pi\hbar^2}\right)^2 \langle \mathbf{k}_f\lambda_f|V|\mathbf{k}_i\lambda_i\rangle^2 \delta\left(\hbar\omega + E_i - E_f\right), \tag{1.5}$$

where $(\mathbf{k}_i\lambda_i)$ and $(\mathbf{k}_f\lambda_f)$ represent the initial and final neutron momenta and spin states, and V represents the interaction operator for neutrons with the sample. Let us start by considering nuclear scattering from a single atom. For a single atom, the extremely short-range real-space potential of nuclei can be simply captured by a delta function, so the potential in momentum space (the Fourier transform of the delta function) is simply a constant,

$$V\left(\mathbf{Q}\right) = \frac{2\pi\hbar^2}{m_n}b, \tag{1.6}$$

where b is the nuclear scattering length, which is usually a complex number. Assuming that b is constant, and inserting Equation 1.6 into Equation 1.5, we obtain the single-atom cross section:

$$\sigma = 4\pi|b|^2. \tag{1.7}$$

The scattering length differs for atoms of different elements, and even for different isotopes of the same element, or for different nuclear spin orientations of the same type of atom. Naturally occuring materials contain isotope mixtures as well as random nuclear spin orientations. Therefore, the cross section of an ensemble of single atomic

species usually is an average of Equation 1.7, which leads to to the averaged total cross section:

$$\sigma_{tot} \;=\; 4\pi\overline{|b|^2}. \tag{1.8}$$

We can divide the total cross section into two parts: the *coherent* cross section, which corresponds to the scattering related to the spatial correlations of the atoms, and the *incoherent* cross section, which is the remainder of σ_{tot} and correponds to the summation of the scattering cross section of individual atoms with random phases:

$$\begin{aligned} \sigma_{coh} &= 4\pi|\bar{b}|^2, \\ \sigma_{inc} &= \sigma_{tot} - \sigma_{coh}, \end{aligned} \tag{1.9}$$

Van Hove (1954) showed that, when N scattering centers are included and only *nuclear* scattering is considered, the cross section can be written as:

$$\frac{d^2\sigma}{d\Omega dE_f} \;=\; N\frac{k_f}{k_i}b^2 S\left(\mathbf{Q},\omega\right), \tag{1.10}$$

where

$$\begin{aligned} S\left(\mathbf{Q},\omega\right) &= \frac{1}{2\pi\hbar N}\sum_{ll'}\int_{-\infty}^{\infty} dt\ \langle e^{-i\mathbf{Q}\cdot\mathbf{r}_{l'}(0)}e^{-i\mathbf{Q}\cdot\mathbf{r}_{l}(t)}\rangle\ e^{-i\omega t} \\ &= \frac{1}{2\pi\hbar N}\int_{-\infty}^{\infty} dt\ e^{-i\omega t}\langle\rho_{\mathbf{Q}}\left(0\right)\rho_{-\mathbf{Q}}\left(t\right)\rangle \end{aligned} \tag{1.11}$$

is the dynamic structure factor. For coherent scattering of N scattering centers, one simply replaces b^2 by $|\bar{b}|^2$ in Equation 1.11.

The dynamic structure factor tells us about what the coherent neutron scattering cross section measures:

1. For inelastic scattering, the cross section reprensents the *time-dependent* pair correlation function of particles in real space, which measures the proability of finding a particle at position $\mathbf{r}$ and time t when there is a particle at position 0 and time 0, i.e., dynamic excitations in the system, such as phonons and spin waves.

2. For elastic scattering, the cross section represents the *static* pair correlation function of particles in real space and measures the probability of finding a particle at position **r** when there is simutaneously a particle at position 0, i.e., coherent elastic scattering probes information about static order, such as the periodic crystal structure of a material.

The above formula works for scattering from a perfectly rigid lattice. In practice, however, fluctuations of the atoms with respect to their equilibrium positions will cause a reduction of the scattering intensities, i.e, there is an extra factor on the right in Equation 1.10:

$$e^{-2W} \;=\; e^{-\langle \mathbf{Q}\cdot\mathbf{u}\rangle^2}, \tag{1.12}$$

where **u** is the instantaneous displacement of an atom from its equilibrium position. This factor is known as the Debye-Waller factor. When temperature is included, we need to introduce the Bose factor as well:

$$bose\,(T) \;=\; \frac{1}{e^{\hbar\omega/k_BT}-1} \tag{1.13}$$

This gives us the final expression for the *coherent, nuclear* neutron scatterng cross section:

$$\frac{d^2\sigma}{d\Omega dE_f} \;=\; \frac{1}{e^{\hbar\omega/k_BT}-1}e^{-2W}N\frac{k_f}{k_i}b^2S\left(\mathbf{Q},\omega\right). \tag{1.14}$$

So far, we have considered the nuclear scattering cross section. We will now consider the *magnetic* scattering scattering cross section, which can be deduced from Equation 1.5:

$$\frac{d^2\sigma}{d\Omega dE_f} \;=\; \frac{1}{e^{\hbar\omega/k_BT}-1}e^{-2W}\frac{N}{\hbar}\frac{k_f}{k_i}p^2[\sum_{\alpha,\beta}\left(\delta_{\alpha,\beta} \;-\; \hat{Q}_\alpha\hat{Q}_\beta\right)]S^{\alpha\beta}\left(\mathbf{Q},\omega\right), \tag{1.15}$$

where α and β are the initial and final spin states, the nuclear scattering length b is

replaced by the magnetic scattering length

$$\begin{aligned} p &= \left(\frac{\gamma r_0}{2} g f\left(\mathbf{Q}\right)\right), \\ f\left(\mathbf{Q}\right) &= \int \rho_s\left(\mathbf{r}\right) e^{i\mathbf{Q}\cdot\mathbf{r}} d\mathbf{r}, \end{aligned} \tag{1.16}$$

with $\frac{\gamma r_0}{2} = 0.2695 \times 10^{-12} cm$, the g-factor is $g = 2$ for spin only magnetic moment, and $f\left(\mathbf{Q}\right)$ is the magnetic form factor, which is the Fourier transform of the normalized unpaired spin density $\rho_s\left(\mathbf{r}\right)$ of an atom. The magnetic dynamic structure factor is

$$S^{\alpha\beta}\left(\mathbf{Q},\omega\right) = \frac{1}{2\pi}\int_{-\infty}^{\infty} dt\ e^{-i\omega t} \sum_l e^{i\mathbf{Q}\cdot\mathbf{r}_l} \langle S_0^{\alpha}\left(0\right) S_l^{\beta}\left(t\right)\rangle. \tag{1.17}$$

Similar to the non-magnetic situation, coherent elastic magnetic neutron scattering detects static magnetic order (e.g., the AF order in the cuprate parent compounds), and coherent inelastic magnetic neutron scattering detects magnetic excitations (e.g., spin waves).

In practice, theoretical calculations usually predict the linear susceptibility χ, whose imaginary part χ'' is connected with the neutron scattering cross section via

$$\frac{d^2\sigma}{d\Omega dE} \ = \ \frac{2\left(\gamma r_e\right)^2}{\pi g^2 \mu_B^2} \frac{k_f}{k_i} |f\left(\mathbf{Q}\right)|^2 \frac{\chi''\left(\mathbf{Q},\omega\right)}{1 - e^{-\omega/k_B T}}, \tag{1.18}$$

where the left side is the scattering cross section, $\gamma r_e = 0.2905$ barn $\cdot\, \mathrm{sr}^{-1}$ is constant, the spin g-factor is 2, μ_B the Bohr magneton, and $f\left(\mathbf{Q}\right)$ is the Cu^{2+} $3d^9$ magnetic form factor calculated using the formula given by [48]. Unlike for nuclear scattering, magnetic density is extended in real space and thus its Fourier transform decreases as $|\mathbf{Q}|$ increases.

In conclusion, the neutron scattering cross section is determined by three main factors: (1) the Bose factor and the thermal vibration Debye-Waller factor, both related to temperature; (2) the elemental single-particle scattering cross section, for nuclear scattering it is the nuclear scattering length b, whereas for magnetic scattering it is the magnetic form factor $f\left(\mathbf{Q}\right)$; (3) the dynamic structure factor $S\left(\mathbf{Q},\omega\right)$, which describes how the nuclei or magnetic moments are correlated in the sample.

1.2.3 Neutron Scattering Facilities

There are two ways to obtain neutrons for scattering experiments: reactor sources and spallation sources. In the former, neutrons are generated inside a nuclear reactor, then cooled in a moderator (e.g., heavy water), and guided with a tube inserted into the moderator. Depending on the temperature of the moderator, the neutrons will have different energy and velocity profiles (see Table 1.2). A common instrument at a reactor source is the so-called triple-axis neutron scattering spectrometer, which features three scattering events along the neutron path and thus is called 'triple-axis spectrometer' [47]. A schematic diagram and a picture of a triple-axis spectrometer are shown in Figure 1.8(a) and (b), respectively. The incident neutrons are first scattered elastically by a single crystal monochromater (e.g., graphite or copper) and, upon changing the scattering angle, the wavelength of scattered neutrons is selected via Bragg's law,

$$\lambda \;=\; \frac{2d\sin\theta}{n}, \tag{1.19}$$

where d is the relavent crystal lattice constant, θ is the scattering angle, and n is any positive integer. The neutrons then typically travel through a filter which blocks higher harmonics (smaller wavelength) neutrons ($n \;>\; 1$), resulting in a well-defined incident energy E_i and momentum $\mathbf{k}_i$. The incident beam then continues to the sample, gets scattered, and undergoes another energy/wavelength selection process via an analyzer crystal to obtain well-controlled final energy E_f and momentum $\mathbf{k}_f$. Finally, neutrons are counted by a detector, which measures the cross section at certain solid angles, as discussed in Section 1.2.2. For neutron-spin polarization analysis, one can use, e.g., Heusler crystals as monochromater and analyzer to resolve the spin state of the incident and outgoing neutrons.

Table 1.2: *Characteristics of triple-axis and time-of-flight spectrometers.*

Source type	Reactor (Triple-axis)	Spallation (Time-of-flight)
Flux	continuous	pulse
Detector type	point detector	2D detector bank
Signal-to-noise ratio	high	low

In a spallation source, neutrons are generated by bombarding a metal target (e.g., liquid Hg at the Spallation Neutron Source) with pulses of protons. The protons interact with the target via the strong nuclear force, which results in pulses of neutrons. The neutron pulses then pass through a long guide tube, and their energy/momentum is selected by Fermi-choppers, which are made of rotating neutron-absorbing blades with openings so that only neutrons with a certain velocity can pass through. The selected neutrons then arrive at the sample, get scattered, and subsequently detected by a large two-dimensional detector bank that consists of hundreds of detector tubes. This detector bank allows measurements of the cross section over a wide solid-angle range, and thus the efficient collection of information. The final energy is calculated from the time that the neutrons fly from sample to the detector bank, hence the name time-of-flight spectrometer. Schematics of a time-of-flight spectrometer are shown in Figure 1.8(c) and (d).

The time-of-flight spectrometer has high detector efficiency and allows the simultaneous measurement of the dynamic structure factor over a large portion of the ω-$\mathbf{Q}$ space, whereas the triple-axis spectrometer has more flexible control of measurement conditions, and usually higher signal-to-noise ratio if one wishes to obtain information at particular points or along specific lines in the ω-$\mathbf{Q}$ space. In other words, the two measurement techniques are highly complementary. This Thesis uses both techniques.

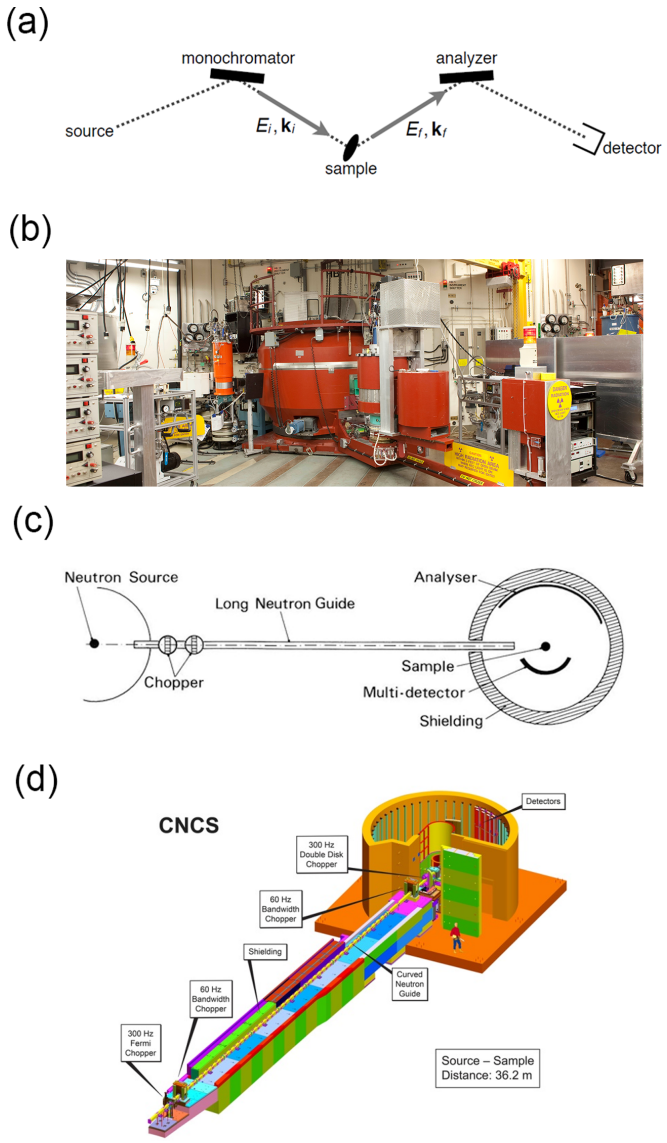

Figure 1.8: *Neutron scattering spectrometers. (a) Schematic of a triple-axis spectrometer. (b) The HB1 triple-axis spectrometer at HFIR, Oak Ridge National Laboratory. (c) Schematic of a time-of-flight spectrometer. (d) Model of the CNCS time-of-flight spectrometer at the SNS, Oak Ridge National Laboratory.*

Chapter 2

Experimental techniques

This Chapter introduces the Hg1201 sample preparation process (Section 2.1) and discusses aspects of the neutron scattering data analysis (Section 2.2) relevant to the subsequent Chapters.

2.1 Sample Preparation

2.1.1 Crystal Growth

Magnetic neutron scattering experiments on cuprates require sizable samples, as their quasi-two-dimensional structure (CuO_2 planes) and small spin-1/2 magnetic moment gives rise to strong quantum fluctuations, and hence to relatively weak coherent magnetic signal. Moreover, the neutron beam size is typically $1'' \times 1''$, so it is desirable to work with a large sample that takes full advantage of the neutron beam.

The growth of sizable Hg1201 single crystals proves to be remarkably difficult. A main challenge is to achieve the required high Hg partial pressure and to avoid exposure to toxic Hg vapor [49]. This excludes the commonly used traveling-solvent floating-zone (TSFZ) crystal growth method. Fortunately, previous members of our research group had successfully developed a stable flux method for the synthesis of Hg1201 single crystals [50]. The main chemical process of this method is the following solid-gas

reaction:

$$\mathrm{HgO\,(g)} \;+\; \mathrm{Ba_2CuO_{3+\delta}\,(s)} \;\Longrightarrow\; \mathrm{HgBa_2CuO_{4+\delta}}. \tag{2.1}$$

The synthesis process consists of several steps. First, CuO and $\mathrm{Ba\,(NO_3)_2}$ powders of 99.999% purity are weighed with molar ratio 1:2 and ground for three hours to achieve a very fine mixture. The mixture is then heated to 920 °C for 17 hours in a ZrO crucible, which is placed into in a quartz kettle with oxygen flow at a rate of four liters per minute (see Figure 2.1(a)). $\mathrm{Ba\,(NO_3)_2}$ decomposes at such high temperatures and releases NO_2 gas, which is flushed away by the oxygen flow. The remaining BaO will then react with CuO to form Ba_2CuO_3, and some O_2 from the oxygen rich atmosphere will also enter the system via following reation:

$$\mathrm{CuO} \;+\; 2\mathrm{BaO} \;+\; \frac{\delta}{2}\mathrm{O_2} \;\Longrightarrow\; \mathrm{Ba_2CuO_{3+\delta}}. \tag{2.2}$$

The excess oxygen in this 'precursor' can enter the Hg1201 product. The precursor is then ground into a powder and mixed with HgO powder. This step needs to be performed in a glovebox with N_2 atmosphere to avoid contamination of H_2O and CO_2 with air, and 0.3 gram of excess HgO is used to generate the high oxygen and Hg vapor pressure. This mixture is transferred into a ZrO cylinder crucible, sealed in vacuum inside a 10 cm long quartz tube (see Figure 2.1(b)), and placed into a high-temperature furnace for the final synthesis step (see Figure 2.1(c)&(d)). The final step involves the temperature profile shown in Figure 2.2. The whole system is heated to 820 °C in three hours, so that the HgO powder will gradually decompose into mercury and oxygen vapor, while the main reaction described in Equation 2.1 takes place and Hg1201 powder material is formed. The temperature is then kept constant for twenty hours to ensure that the reaction is complete. The Hg1201 powder is then heated to 1020 °C in 20 hours and becomes liquid. The system is kept at this high temperature for three hours, and then slowly cooled at 2 °C per hour to 900 °C. It is during this cooling step that Hg1201 single crystals form. Crytals grown with this method are underdoped with $T_c \approx 80$ K.

Single crystals of the double-layer sister compound Hg1212 can also be synthesized with the same method. What is different compared to the growth of Hg1201 is that the

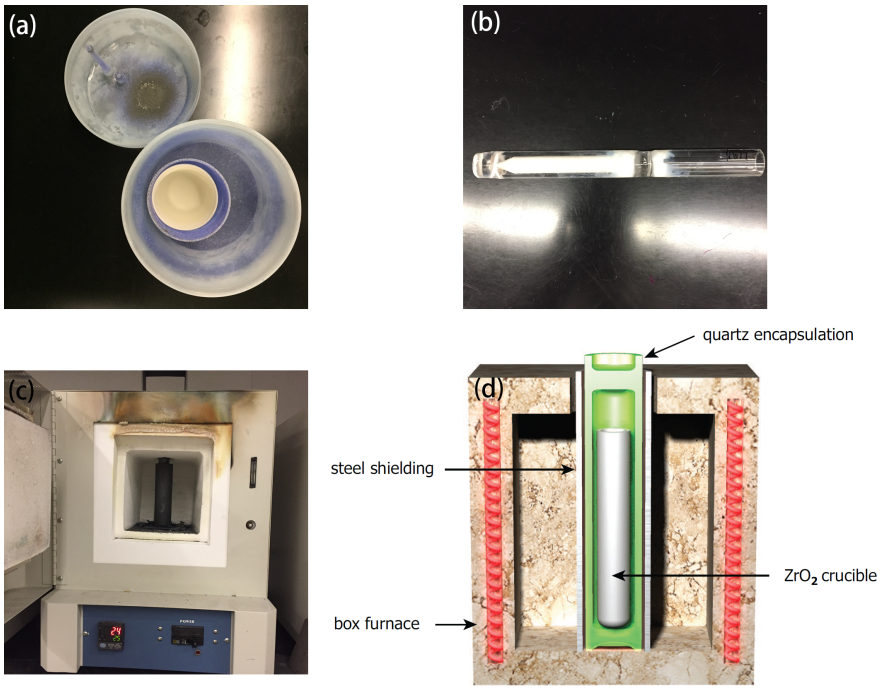

Figure 2.1: *Growth of Hg1201 and Hg1212 single crystals. (a) Kettle for precursor sintering. The short and long tubes on the lid (top left) are openings to allow for oxygen flow. The white crucible sits inside a quartz container, which in turn is placed inside the kettle body (bottom right). (b) White point-end crucible with mixed precursor and HgO powder (HgO and CaO in the case of Hg1212 growth), sealed inside a quartz tube. (c) Furnace used for the growth of Hg1201 and Hg1212. (d) Sketch of the setup in c.*

precusor undergoes the reaction:

$$2\mathrm{CuO} \;+\; 2\mathrm{BaO} \;+\; \frac{\delta}{2}\mathrm{O_2} \;\Longrightarrow\; \mathrm{Ba_2Cu_2O_{4+\delta}}. \tag{2.3}$$

The percursor is then mixed with HgO and CaO powders, and the final synthesis step is summarized in Figure 2.2. The main chemical reaction is:

$$\mathrm{HgO\,(g)} \;+\mathrm{CaO} \;+\; \mathrm{Ba_2Cu_2O_{4+\delta}\,(s)} \;\Longrightarrow\; \mathrm{HgBa_2CaCu_2O_{6+\delta}}. \tag{2.4}$$

Unfortunately, the ideal Hg vapor pressure required for the growth of Hg1212 is higher than that for Hg1201 and beyond the stability limit of the best quartz tubes.

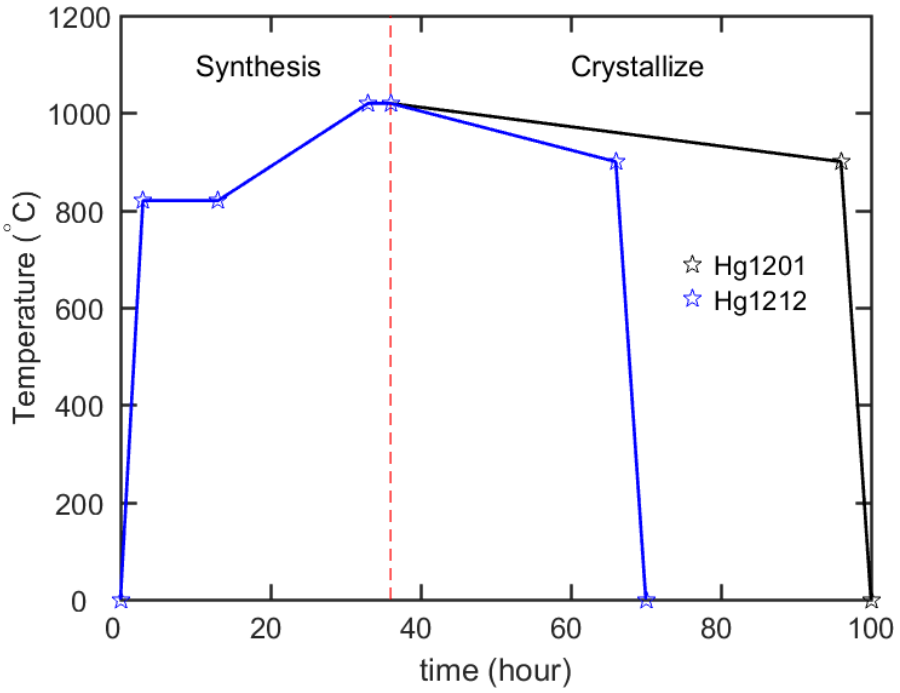

Figure 2.2: *Temperature profile for the growth of Hg1201 and Hg1212 single crystals.*

Therefore, the Hg1212 single crystals are usually considerably smaller than those of Hg1201.

Figure 2.3 shows Hg1201 and Hg1212 crystals grown by the above method, along with typical superconducting quantum interference device (SQUID) magnetometry measurement results. The sudden change in the magnetic susceptibility below T_c signifies the Meissner-Ochsenfeld effect (see Figure 1.1). A recent manuscript describes growth and characterization results of Hg1212 single crystals grown with this conventional method and with an improved high-pressure method developed in Yuan Li's labratory at Peking University [51].

2.1.2 Doping Control and Crystal Co-Mounting

As-grown Hg1201 single crystals are usually underdoped with a T_c of about 80 K and the interstitial oxygen atoms are not homogeneously distributed. In order to tune the doping level and achieve a homogeneous oxygen dopant distribution, heat treatments

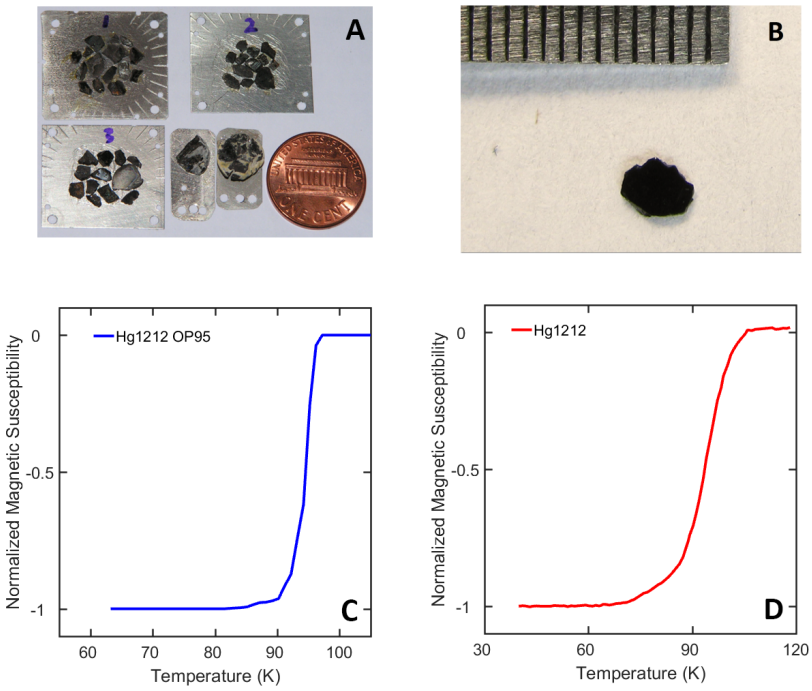

Figure 2.3: *Pictures of crystals and magnetic susceptibility data. (a) Co-aligned Hg1201 crystals for a neutron scattering experiment with a penny coin as reference. (b) Single crystal of Hg1212. The black stripes on silver background is are the 1 mm marks of a ruler. (c) and (d) show corresponding SQUID measurement of the samples in a and b. The susceptibility magnitude is normalized to -1 at low temperature.*

(anneals) at various temperatures and atmospheres were performed. A list of some anneal conditions and final T_c values is shown in Table 2.1. In what follows, we will use the abbreviations OV, OP and UD to denote overdoped, optimally-doped and underdoped crystals. For example, OV88 denotes an overdoped crystal with $T_c = 88$ K, and UD55 denotes an underdoped crystal with $T_c = 55$ K. Unless indicated otherwise, T_c is chosen to be the centerpoint of the superconducting transition determined from magnetic susceptibility measurements. We note that the crystal quality (e.g., impurity inclusions, structural defects) depends on various aspects, such as the growth furnace used and, correspondingly, the anneal conditions to achieve a certain T_c value summarized in Table 2.1 depend on different growth batches. However, this dependence is relatively subtle.

Table 2.1: *Summary of anneal conditions for Hg1201 crystals. Final T_c values after anneals under the specified conditions. OV: over-doped; OP: (nearly) optimally-doped; UD: underdoped*

Anneal Condition	Final T_c (K)
300 °C, 6 bar O_2	92 (OV)
300 °C, O_2 flow	95 (OP)
450 °C, air	80 (UD)
480 °C, N_2 flow	71 (UD)
500 °C, air	65 (UD)
500 °C, 3 mTorr vacuum	55 or lower (UD)

Moreover, the vacuum level during reduction is not precisely controlled and may vary somewhat among the anneal furnaces, which results in slightly different hole doping levels and T_c values.

After the anneal, the crystals are suitable for use in neutron scattering measurements, yet as noted, a single piece of crystal is not enough. The typical lateral dimension of the neutron beam at the sample position is 2.5 cm, and the neutron penetration depth is comparable. However, it is less in Hg1201 than, e.g., in LSCO, due to the high neutron absorption cross section of Hg. Therefore, to fully use the neutron beam and obtain a good signal, it is desirable to work with large samples (0.1 - 1 cm^3 or 1 - 10 gram). No other standard experimental technique in condensed matter physics requires such large samples (e.g., the typical sample mass for a synchrotron X-ray scattering experiment is a few miligrams with linear dimension of less than 1 mm). The typical mass of the Hg1201 single crystals grown in our laboratory is a few tens of miligrams. In order to achieve a large enough sample size for a state-of-art neutron scattering experiment, 30-40 single crystals are co-oriented on several aluminum plates, so they form a large sample mosaic. Aluminum is chosen due to small absorption cross section and its relatively small incoherent scattering cross section compared to other materials commonly used in cryogenic experiments.

In order to co-mount the crystals, crystal surfaces parallel to the CuO_2 planes (also

denoted ab-planes) need to be polished, so that when the crystals are glued to the aluminum plates, their ab-planes are parallel. Moreover, it is also necessary to carefully align the crystals laterally along the tetragonal a-axis. A picture of such a sample is shown in Figure 2.3a.

2.2 Neutron Scattering Data Analysis

We typically first aligned the sample on the Bragg peaks (0 0 4) and (1 1 0). Program sequences were written to obtain data as a function of energy transfer ω, momentum transfer $\mathbf{Q}$, and temperature T. Data files were saved to the spectrometer database, which records neutron counts in the detectors and configuration parameters. The data files were usually written in different formats for different spectrometers. The typical data structure and analysis methods are introduced in this Section, for both unpolarized and polarized triple-axis measurements, and for the time-of-flight spectrometer ARCS.

2.2.1 Triple-Axis Spectometer

In a typical experiment with a triple-axis spectrometer, either a so-called momentum-scan ($\mathbf{Q}$-scan) or energy-scan (ω-scan) is performed at a certain temperature. For a $\mathbf{Q}$-scan, the energy transfer is kept constant, the value of momentum transfer is varied, and at each momentum transfer a point detector counts for a certain time and record the cross section. Therefore, an intensity versus momentum transfer plot is obtained. For an ω-scan, it is the other way around, and an intensity versus energy transfer plot is obtained. In other words, each $\mathbf{Q}$- or ω-scan corresponds to measuring the cross section along a line-trajectory in the four-dimensional energy-momentum space. According to linear response theory [52], an enhancement of the cross section (Section 1.2.2) is expected if there is structural or magnetic order (Bragg peaks, $\omega = 0$) at characteristic $\mathbf{Q}$ values, or for excitations (e.g., phonons or spin waves) with a characteristic ω-$\mathbf{Q}$ dispersion. These intensity (and hence susceptibility) peaks are broadened by the imperfection of the instrumentation, which is referred to as the instrument resolution. They are also broadened (in $\mathbf{Q}$) if the spatial correlation length of the order is short-ranged, or (in ω) as a result of the finite life-time of excitations.

Figure 2.4a shows a plot of measured intensity versus energy-transfer for a typical

ω-scan for Hg1201 in a wide energy-transfer range, from about 20 meV to 65 meV. At 4 K, a weaker peak at 32 meV and a stronger peak at 54 meV are seen from the raw data, on top of a non-linear background. Figure 2.4b shows the temperature difference of such data, i.e., the data at high temperature are subtracted from those at low temperature. Magnetic signal is usually stronger at low temperatures, whereas most of the background signal (such as phonons) is usually stronger at high temperature, or independent of temperature. Therefore, the temperature difference of the measured intensity removes some background effects and highlights magnetic signal.

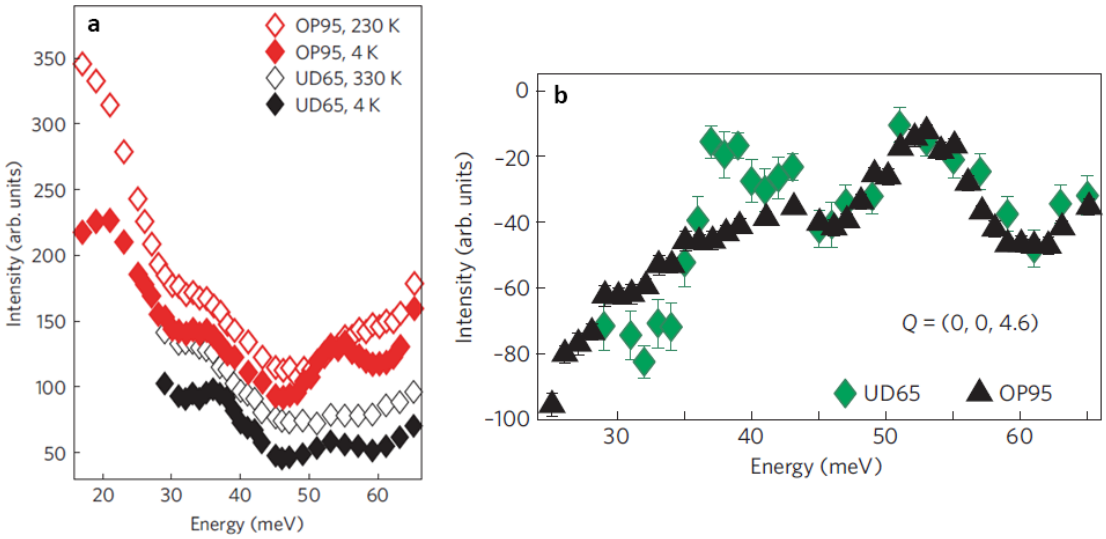

Figure 2.4: *Example of ω-scans in a triple-axis spectromenter measurement [43]. (a) ω-scan from about ω = 20 meV to 65 meV for two Hg1201 samples UD65 (black) and OP95 (red) at low (closed diamonds) and high (open diamonds) temperatures. The momentum transfer is* $\mathbf{Q}$ *= (0 0 4.6). (b) Temperature difference of the data in a. The two peaks for UD65 and the high-energy peak for OP95 are much clearer after subtraction of the high-temperature data.*

2.2.2 Polarized Triple-Axis Spectometer

With a polarized triple-axis spectrometer, additional information about the spin state of a system can be obtained. There are two types of cross sections: spin-flip (SF) and

non-spin-flip (NSF). For SF scattering, the neutron spin polarization direction is flipped during the scattering process, i.e., one observes magnetic signal. For NSF scattering, the spin polarization direction remains unaltered (if the incident neutron-spin polarization is parallel to $\mathbf{Q}$), and one measures non-magnetic (nuclear) signal. It is important to note that due to the unavoidable imperfections of the instrument, the SF and NSF signals results are not perfectly separated. There will be leakage of the typically much stronger nuclear NSF scattering in the nominal SF geometry, causing an increase in the observed intensity. One usually refers to the so-called flipping ratio (FR), which is defined as $FR \equiv I_{NSF}/I_{SF}$, where I_{NSF} and I_{SF} are the NSF and SF intensities. In the case of an anticipated magnetic phase transition with magnetic Bragg peaks that coincide with nuclear Bragg peaks (e.g., in ferromagnets or in the case of the unusual IUC magnetic order exhibited by the cuprates), one can use the FR at high temperature (where no magnetic Bragg signal is expected) to estimate the NSF leakage at low temperature, and the pure magnetic signal should then be:

$$I_{mag} = I_{SF} - \frac{I_{NSF}}{FR}. \tag{2.5}$$

Figure 2.5 gives an example of such a measurement of IUC magnetic order. In Figure 2.5a-d, the NSF intensities are scaled by the FR estimated at high temperature. Note that the FR for these different polarization geometries in Figure 2.5a-c are found to be nearly the same (theoretically, they should be identical) and approch 100, which is a very high value (and implies relatively small leakage). We note that such measurements for the cuprates have only been successful at a few facilities world-wide (LLB and ILL, France) due to the stringent experimental requirements. The polarization-averaged, FR corrected signal in Figure 2.5d exhibits order-parameter-like temperature dependence below $T_{mag} \approx 300$ K, which corresponds to the PG temperature of the studied sample.

Another very useful tool to analyze polarized-neutron data obtained with a triple-axis spectrometer is the so-called longitudinal polarization analysis (LPA). This analysis takes advantage of the following relation between the magnetic cross section, neutron spin $\mathbf{P}$, momentum transfer $\mathbf{Q}$, and magnetic moment $\mathbf{M}$:

$$I_{SF} \propto \mathbf{M} \cdot (\mathbf{P} \times \mathbf{Q}) \tag{2.6}$$

It is clear from Equation 2.6 that only the magnetic moment component that is both

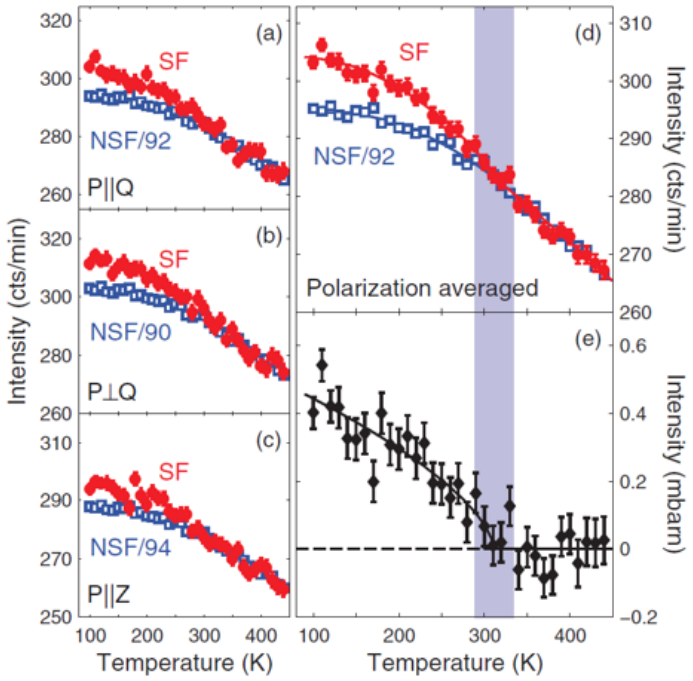

Figure 2.5: *Example of a polarized-neutron triple-axis spectromenter measurement [86]. The Hg1201 sample has T_c = 71 K (UD71). (a)-(c) SF (red circles) and NSF (blue squares) intensity measured at the (1 0 1) reflection for three orthogonal incident neutron-spin polarization directions, which are marked on the left bottom corner of each panel. NSF intensities are scaled by the FR estimated at high temperature as indicated. (d) Average of the data in a-c. (e) Extracted pure magnetic signal shown as the difference between the SF intensity and the scaled NSF intensity. The onset of the IUC magnetic order at $T_{mag} \approx 300$ K coincides with the pseudogap temperature T^* obtained from planar resistivity measurements.*

perpendicular to **P** and **Q** will contribute to the SF intensity. Therefore, for a fixed value of **Q**, one can obtain information about the projection of the moment by chosing the direction of **P**. A typical choice for **P** is the **xyz** basis, where **x** is the momentum transfer direction, **z** the direction perpendicular to the scattering plane, and **y** the direction perpendicular to both of **x** and **z**. In Figure 2.5, **P** $\parallel$ **Q**, **P** $\perp$ **Q** and **P** $\parallel$ **z** correspond to **x**, **y** and **z**, respectively. With this basis, and with the decomposition

$\mathbf{M} = \mathbf{M_x} + \mathbf{M_y} + \mathbf{M_z}$, one has:

$$\begin{aligned} I^x_{SF} &= I_{BG} + I(\mathbf{M_y}) + I(\mathbf{M_z}), \\ I^y_{SF} &= I_{BG} + I(\mathbf{M_z}), \\ I^z_{SF} &= I_{BG} + I(\mathbf{M_y}), \end{aligned} \tag{2.7}$$

where $I^{x,y,z}_{SF}$ are the SF intensities measured with incident neutron-spin polarization along $\mathbf{x}$, $\mathbf{y}$ and $\mathbf{z}$, respectively; I_{BG} is the background noise which is expected (and generally measured to be) the same for all three configurations, and $I(\mathbf{M_{x,y,z}})$ are the magnetic cross sections due to scattering from magnetic moment components $\mathbf{M_{x,y,z}}$. One can either extract the background signal I_{BG},

$$I_{BG} = I^y_{SF} + I^z_{SF} - I^x_{SF}, \tag{2.8}$$

or the pure magnetic signal $I(\mathbf{M_y}) + I(\mathbf{M_z})$ without background,

$$I^{SF}_{mag} = 2I^x_{SF} - I^y_{SF} - I^z_{SF}. \tag{2.9}$$

Moreover, one can also work with data obtained in the NSF channel, using similar notation one has

$$\begin{aligned} I^x_{NSF} &= I_{BG}, \\ I^y_{NSF} &= I_{BG} + I(\mathbf{M_y}), \\ I^z_{NSF} &= I_{BG} + I(\mathbf{M_z}), \end{aligned} \tag{2.10}$$

where $I^{x,y,z}_{NSF}$ are the NSF intensities measured with incident neutron spin polarization along $\mathbf{x}$, $\mathbf{y}$ and $\mathbf{z}$, respectively. The pure magnetic signal $I(\mathbf{M_y}) + I(\mathbf{M_z})$ is then calculated via:

$$I^{NSF}_{mag} = I^y_{NSF} + I^z_{NSF} - 2I^x_{NSF} \tag{2.11}$$

Figure 2.6 shows the result of a constant $\omega = 48$ meV momentum scan through the two-dimensional (2D) AF wave vector $\mathbf{q}_{AF} = (0.5, 0.5)$ using LPA. In Figure 2.6a, the background intensity is estimated using Equation 2.8, and compared to I^x_{SF}. In Figure

2.6b, the magnetic signal is estimated using both Equation 2.9 and 2.11. The data consistently show magnetic signal centered at $\mathbf{q}_{AF}$.

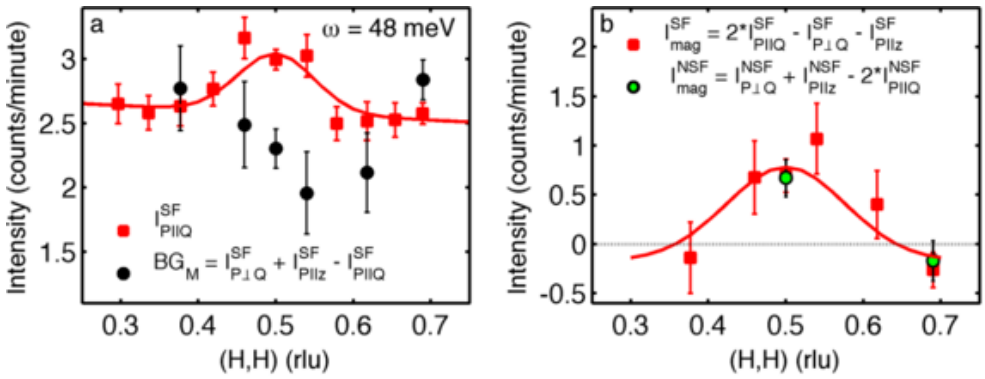

Figure 2.6: *LPA of a polarized-neutron triple-axis spectromenter measurement [78]. The Hg1201 sample studied has T_c = 55 K. (a)* **Q***-scan across the two-dimensional AF wave vector* $\mathbf{q}_{AF}$ *(H = 0.5) at* ω *= 48 meV and T = 5 K. Red squares show data collected with incident neutron spin polarization parallel to* **Q***, i.e.,* I^x_{SF} *in the notation used in this Chapter; black circles are the background estimated using Equation 2.8. (b) Similar data as in a, but the plots now show pure magnetic signal estimated using Equation 2.9 (red squares) and Equation 2.11 (green squares).*

2.2.3 Time-of-Flight Spectrometer

In a time-of-flight (TOF) experiment, one usually does not move the sample and collects neutron counts for extended periods of up to several days. The reason for this is that a TOF spectrometer has a 2D detector bank that allows one to resolve the final neutron energy by measuring the time that neutrons travel from the sample to the detector. Therefore, for each neutron pulse that hits the sample at the nominal time $t \equiv 0$ that can be calculated from the Fermi-chopper configuration upstream, the detector bank collects data with energy transfers that range from $\omega = 0$ up to close to the incident neutron energy, and for each energy transfer ω, it collects wide range of momentum transfers **Q** (a surface in the 3D momentum space). However, the signal at each point in

ω-$\mathbf{Q}$ space is significantly weaker than for a triple-axis spectrometer, and therefore longer counting times are required. The data collected with a TOF spectrometer are usually stored on the spectrometer computer work station, and special software is required to access the data; for example, DAVE is used at the ISIS Neutron and Muon Source in Great Britain and at the Spallation Neutron Source. We denote the three components of momentum transfer as $\mathbf{Q} = (H,\ K,\ L)$, and analyze cuts or slices of the 3D data (effectively, 3D ω-$\mathbf{Q}$ segments of the 4D ω-$\mathbf{Q}$ space are probed): a 1D cut (cross section versus H or ω, similar to triple-axis spectrometer data), or a 2D slice (cross section versus H and K at fixed ω). At fixed 2D momentum transfer $(H,\ K)$, L is coupled to ω due to the momentum and energy conservation laws. We do not consider this implicit L-dependence of our data, since the dynamic magnetic response of the lamellar cuprates is known to be essentially two-dimensional, i.e., nearly independent of L. Figure 2.7a shows an example of a 2D slice of data obtained with the TOF spectrometer ARCS. The slice corresponds to the shaded surface in 3D momentum-energy space shown in Figure 2.7f. The peak at the magnetic Brillouin zone center indicates a non-zero AF response, which is clearer after the removal of an estimated azimuthally-symmetric background (Figure 2.7b,c). The data can then be converted from the measured intensity to the magnetic susceptibility using Equation 1.18, and then fit to a 2D Gaussian (Figure 2.7d,e). Such TOF data will be discussed in detail in Chapter 3.

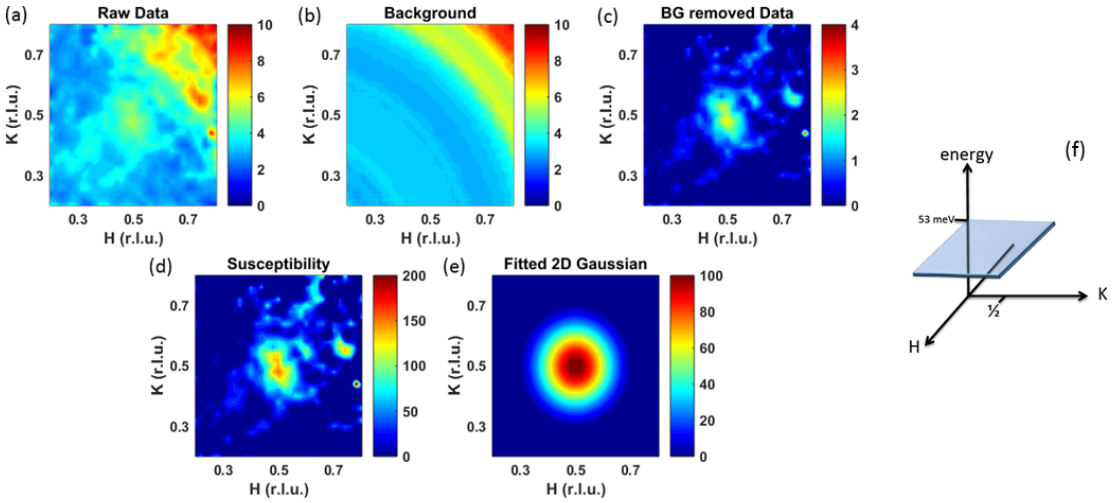

Figure 2.7: *Demonstration of TOF data analysis. (a) Constant-energy (ω = 30 meV) slice of raw data for sample Hg1201 UD71 in the first Brillouin zone, as measured on ARCS. Data are preprocessed by the spectrometer database, including rescaling data counted by different detector tubes that have different efficiencies. (b) The first Brillouin zone is divided into ring-like areas. The background is estimated by averaging data in each ring, excluding data within 0.1 r.l.u. from* $\mathbf{q}_{AF}$*. (c) Background-removed data. (d) Suceptibility obtained from scaling the data in c using Equation 1.18. (e) Result of a two-dimensional Gaussian fit to the result in d. (f) Schematic constant-ω slice in 3D energy-momentum (ω, H, K) space; L is coupled to ω and not considered, since the magnetic response of the lamellar crystals only weakly depends on the momentum transfer component perpendicular to the* CuO_2 *planes.*

Chapter 3

Antiferromagnetic Response

The temperature-doping phase diagram of the hole-doped cuprates was briefly introduced in Chapter 1. This and the following Chapter focus on the mysterious pseudogap (PG) phase and its magnetic properties. In this Chapter, a systematic study of the antiferromagentic response of the CuO_2 plane in Hg1201 is presented. As shown schematically in Figure 3.1, at zero doping, there exist localized spin-1/2 magnetic moments at all the Cu sites, with a tendacy to align antiparallel to their nearest neighbors. This state is an antiferromagnetic (AF) charge-transfer insulator. As holes are added to the system, they predominately occupy the planar oxygen $2p_{x,y}$ orbitals, and frustrate the AF state, so that the long-range AF order is broken. However, substantial AF fluctuations are still observed in the PG and superconducting (SC) phases. The experimental and theoretical study of the AF response of the CuO_2 planes has been of tremendous interest, in particular because spin fluctuation might be the glue that bounds holes into Cooper pairs [25]. More generally, understanding the connection between magnetic degrees of freedom and the PG and SC phases might hold the key to the solution of the cuprate high-T_c problem.

3.1 Previous Measurements

Studies of the AF response of the cuprates have mostly focused on the two compounds $La_{2-x}Sr_xCuO_4$ (LSCO) and $YBa_2Cu_3O_{6+x}$ (YBCO), for which the required sizable single crystals have been available since the early days of cuprate research. As discussed

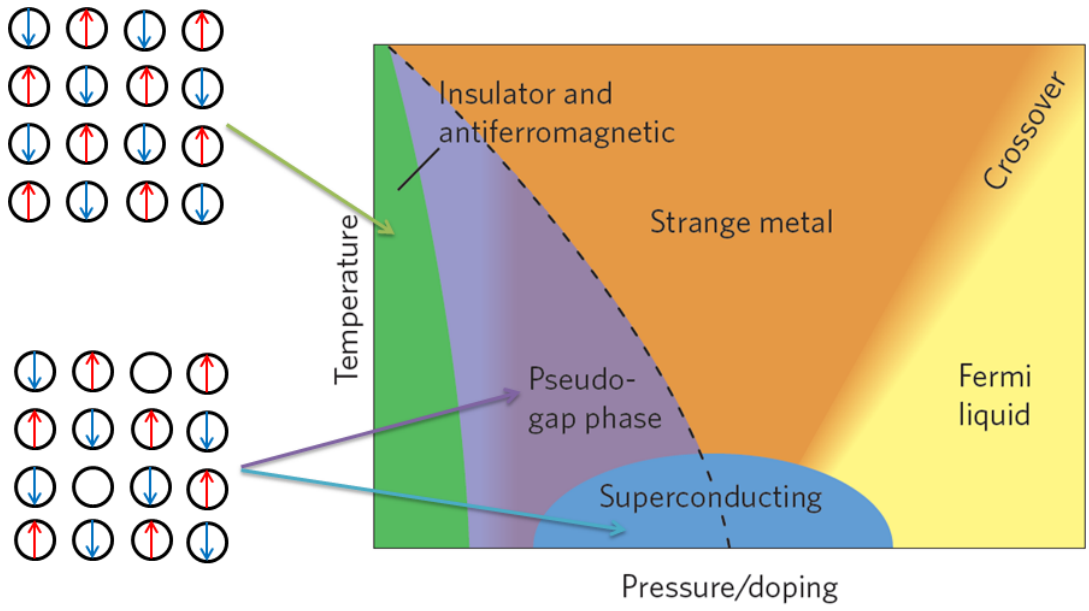

Figure 3.1: *Schematic cuprate phase diagram. Main figure: the phase diagram of hole-doped cuprates (from Ref [56]). The phases are indicated by different colors. To the left of the phase diagram: schematic of the spin location and alignment on the Cu site, with long-range AF order (top) pointing to the AF phase, and short-range AF fluctuations (bottom).*

in Chapter 1, the undoped parent compounds are AF Mott (charge-transfer) insulators rather than band metals. Early neutron scattering work demonstrated Néel order below room temperature [53] and strong two-dimensional AF spin fluctuations [54]. As shown in Figure 3.2, subsequent work identified robust spin waves in undoped La_2CuO_4 with a very large superexchange energy $J \sim 130$ meV ~ 1500 K, comparable to the melt temperature of these complex oxides [57]. It was also established early on that the doped SC compound LSCO exhibits significant dynamic AF correlations [27]. Extensive subsequent neutron scattering work has been performed and reviewed [27–29]. Given that the materials are doped AF insulators and that the magnetic energy scale is so large, it is natural to think of a spin-fluctuation mediated pairing mechanism. This Thesis does not provide direct evidence for this scenario. Rather, it constitutes the first

systematic study of the AF response in the model cuprate Hg1201 in the SC doping range.

The AF response of the SC compounds has been found to exhibit three characteristic features, summarized in Sections 3.1.1, 3.1.2, and 3.1.3.

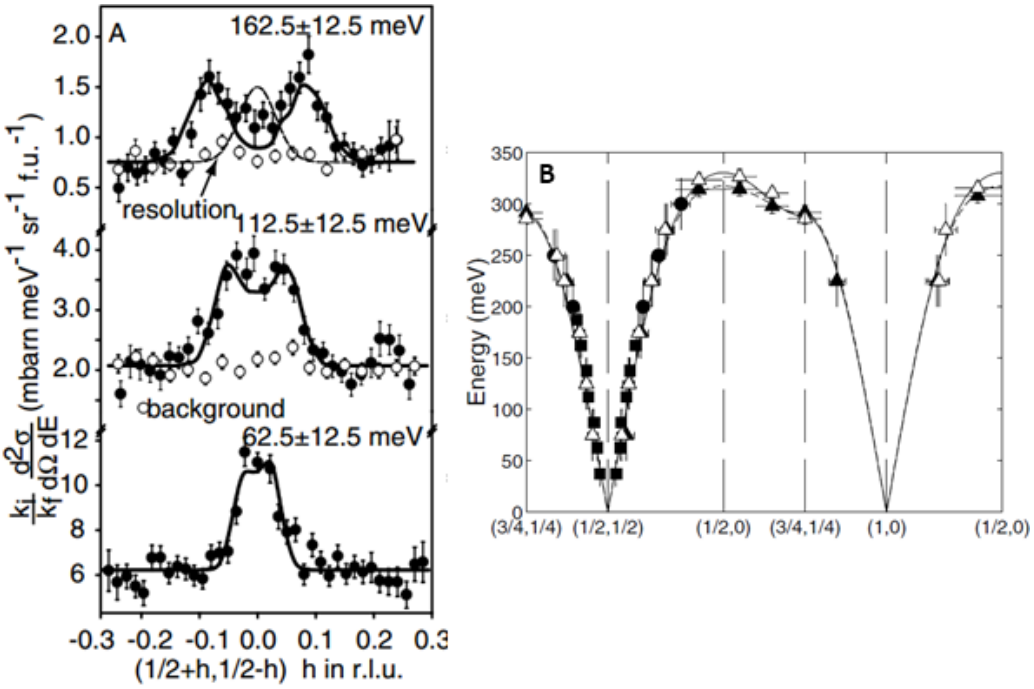

Figure 3.2: *Spin-wave dispersion of undoped* La_2CuO_4 *[57]. (a) Momentum scans across the AF wave vector* $\mathbf{q}_{AF}$ *= (0.5 0.5) at three different energy transfers. Horizontal axis indicates the distance between the reduced two-dimensional momentum transfer* $\mathbf{q}$ *and* $\mathbf{q}_{AF}$*. The peaks in the cross section indicate the spin-wave signal. (b) The energy-momentum dispersion along high-symmetry directions in the magnetic Brillouin zone. The large (linear) slope and zone boundary energy signify a very large superexchange energy of* $J \sim 130$ *meV.*

3.1.1 Hourglass Dispersion

A seemingly universal feature of the AF response of the doped cuprates is the so-called hourglass dispersion: the energy (ω) and two-dimensional momentum ($\mathbf{q}$) dependent dynamic magnetic susceptibility $\chi''(\mathbf{q},\omega)$ disperses with increasing energy from incommensurate wave-vectors at $\omega \approx 0$ toward the antiferromagnetic wave vector $\mathbf{q}_{AF} =$ (0.5, 0.5) (in reciprocal lattice units; this is often also written as $\mathbf{q}_{AF} = (\pi,\pi)$, with $a \equiv b \equiv 1$), and then outward again at higher energies, resulting in an hourglass $\mathbf{q}$-ω shape. Figure 3.3(a) shows data for an energy-momentum slice through $\mathbf{q}_{AF}$ for LSCO, $La_{2-x}Ba_xCuO_4$ (LBCO), YBCO and $Bi_2Sr_2CaCu_2O_{8+\delta}$ (Bi2212) [28]. Similar results have also been obtained for $Bi_2Sr_2CuO_{6+\delta}$ (Bi2201) [58], and it has been thought that the hourglass dispersion is a universal property of the hole-doped cuprates. We note that LSCO, LBCO and Bi2201 are single-CuO_2-layer compounds, whereas YBCO and Bi2212 are double-layer compounds.

Considerable efforts have been made to understand the microscopic nature of the hourglass dispersion [28,29]. The upper part of the dispersion (above the commensurate 'neck' position) is believed to be a remnant of the high-energy spin-wave excitations of the undoped system [59]. Indeed, as shown in Figure 3.3(b), the two roughly agree, with a smaller effective spin-wave velocity (or J) of the doped system. However, the microscopic origin of the lower part of the dispersion (below the neck) has been under debate. While the upper part is universal among all cuprates studied so far, the lower part is not. For example, in LSCO, the lower part of the dispersion is incommensurate at temperatures both below and above T_c, whereas it undergoes a change from incommensurate to commensurate upon warming across T_c in one of the two inequivalent in-plane directions in underdoped orthorhombic YBCO [60]. Two dinstinct pictures have been proposed for the explanation of the lower part of the dispersion.

In LSCO, the low-energy dispersion can be understood within the local-moment picture, in which modulated AF stripes are formed of copper spins, separated by periodically-spaced domain walls (Figure 3.4) [61]. It is worth to note, that although very alike, the stripe order is distinct from conventional charge-density-wave (CDW) or spin-density-wave (SDW) order. Conventional CDW or SDW order results from nesting of reciprocal space points on the Fermi surface. The stripe order is a special order, as the ground state of doped system favors real space alignment in which charges form

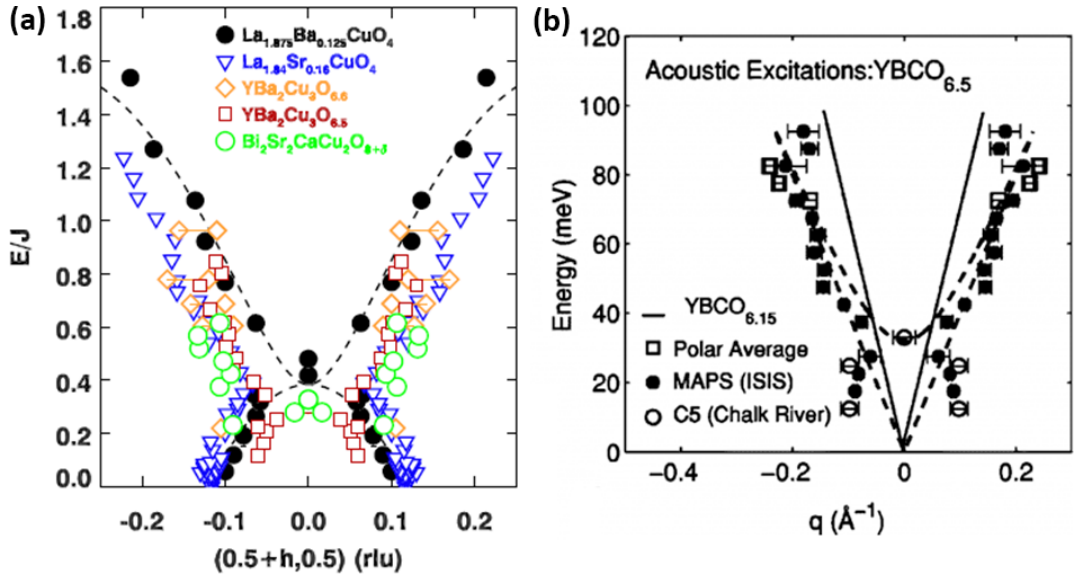

Figure 3.3: *Hourglass magnetic dispersion. (a) 2D slice through the hourglass-shaped* $\mathbf{q}$-ω *dispersion for LBCO, LSCO, YBCO and Bi2212. The horizontal axis marks the distance from* $\mathbf{q}_{AF}$*, whereas the vertical axis marks energy in units of the nearest-neighbour AF superexchange energy (*$J \sim$ *120 - 130 meV) [28]. (b) Comparison of the upper hourglass dispersion of SC* $YBCO_{6.5}$ *to the spin-wave dispersion of nominally undoped* $YBCO_{6.15}$ *(solid line). Data for* $YBCO_{6.5}$ *were collected on different spectrometers (marked by different symbols) [59].*

stipe-like antiphase domain walls for the magnetic stripes. This can also be viewed as coupled CDW-SDW order and has been observed in neutron scattering measurements of LSCO and related compounds (Figure 3.4a-c) [28, 61].

For YBCO, an itinerant picture is considered, in which magnetic excitations are created by transferring an electron from an occupied state to an empty state, with a flip of the spin (the so-called electron-hole or *e-h* spin-flip exciton [29]). In this senario, the momentum of the AF response is the vector that connects two nested points on the Fermi surface. For example, the vector that connects the intersection of the Fermi surface and the AF Brillouin zone boundary (the *hot spots*) is equal to $\mathbf{q}_{AF}$; and the vector that connects the two anti-nodal points on the Fermi surface (the *cold spots*) is

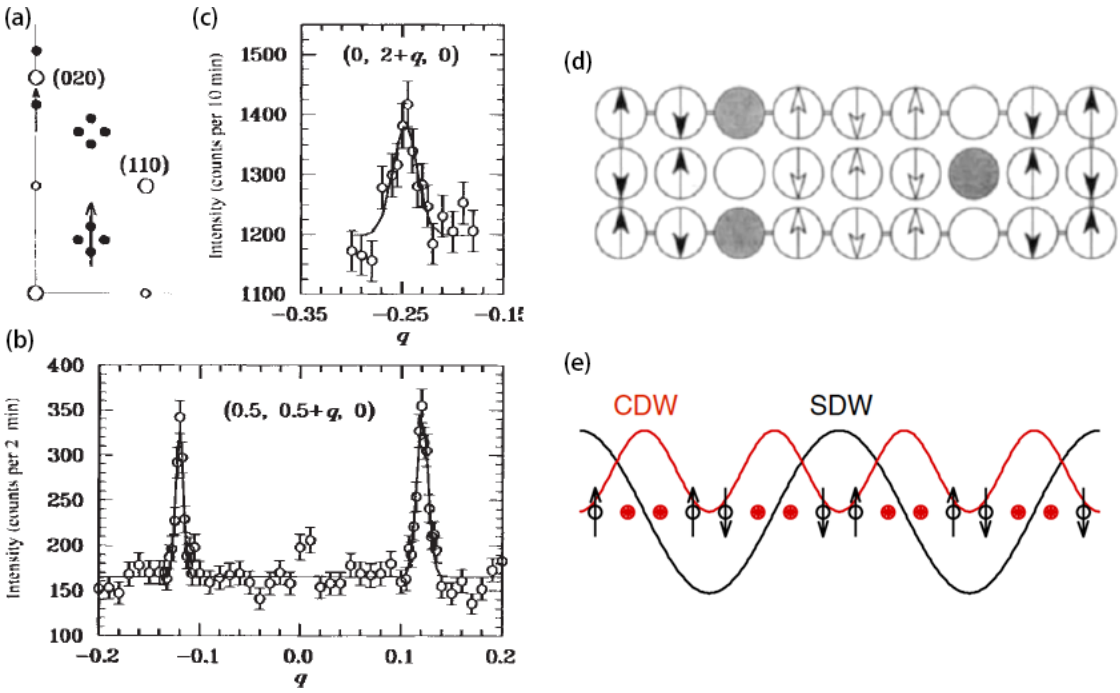

Figure 3.4: *Incommensurate AF response and stripe picture [61]. The data are for Nd-doped LSCO: (a) Reciprocal space diagram, open circles indicate nuclear Bragg peaks, closed circles indicate the spin- and charge- stripe peaks. Arrows indicate the momentum scans in (b) and (c) performed in the neutron scattering experiment. (b)-(c) Momentum scans as indicated by the arrows in (a). The peaks clearly show the existence of (b) magnetic and (c) nuclear/charge components of stripe order. Solid lines are Gaussian fits. (d) Hypothesized stripe pattern within the CuO_2 plane. Only the Cu atoms are shown (circles); arrows indicate the orientation of magnetic moments on Cu atoms, which are locally antiparallel; filled cirles denote the presence of a charge carrier (hole), although the charge density may be uniform along a domain wall. (e) Schematic to show that the stripe order can also be thought of as a coupled spin-density-wave (SDW) and charge-density-wave (CDW).*

defined as $\mathbf{q}_n$ (Figure 3.5b). Spin excitons can can only exist below the *e-h* spin-flip continum, since otherwise they decay into elementary *e-h* excitations. The energy of the continuum can be either calculated or measured by angle-resolved photoemission

spectroscopy (ARPES). As shown in Figure 3.5(a), the lower bound of the continuum energy, ω_c, is maximized at $\mathbf{q}_{AF}$, with a downward dispersion as the 2D momentum $\mathbf{q}$ moves away from $\mathbf{q}_{AF}$, reaching zero at $\mathbf{q}_n$. Therefore, near $\mathbf{q}_{AF}$, the AF response roughly follows ω_c and disperse downward. Further awary from $\mathbf{q}_{AF}$, ω_c reappears at higher energy and creates an upward dispersion. A theoretical simulation, shown in Figure 3.5(c), is roughly in consistent with the experimental results in Figure 3.5(a).

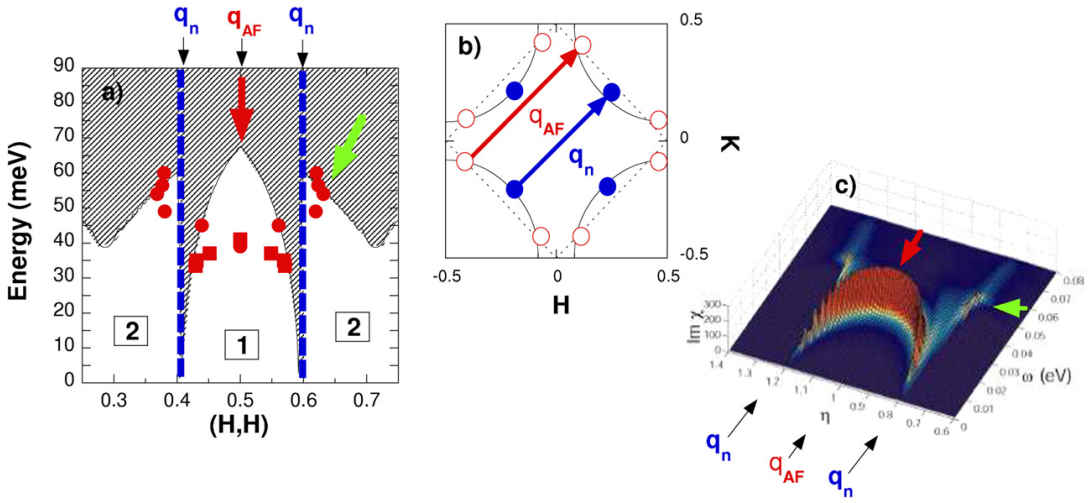

Figure 3.5: *Itenerant picture of AF response [29]. (a) In weakly underdoped* $YBa_2Cu_3O_{6.85}$ *(T_c = 89 K), the acoustic resonant spin excitations disperse downward (squares) and upward (circles). The dashed region indicates the location of the electron-hole spin-flip continuum, determined from ARPES measurements of* $Bi_2Sr_2CaCu_2O_{8+\delta}$ *for a similar doping level. (b) Sketch of the Fermi surface. The red circles correspond to hot spots, that can be connected by the AF wave vector* $\mathbf{q}_{AF}$*, where the superconducting gap is almost maximum. The blue circles indicate cold spots, where the superconducting gap vanishes on the Fermi surface. Along the diagonal directions, the cold spots are connected by the wave vector* $\mathbf{q}_n$*. (c) Computation of the imaginary part of the dynamical magnetic susceptibility in the superconducting state within the spin-exciton scenario, suggests the existence of two distinc branches (red and green arrows).*

3.1.2 Resonance

A prominent characteristic of the AF response of SC YBCO is the magnetic resonance, a large and abrupt susceptibility increase at $\mathbf{q}_{AF}$ at a well-defined energy ω_r upon cooling below T_c [63, 64]. This excitation was first observed in YBCO [63], and later confirmed in Bi2212 [65] and $Tl_2Ba_2CuO_6$ (Tl2201) [66] (Figure 3.6), as well as in optimally-doped Hg1201 [67]. However, it is not seen in LSCO or in conventional superconductors. The resonance is thought to be significant because it is a magnetic excitation correlated with the SC phase, and its energy scale roughly scales with the superconducting gap Δ_{sc} [68]. Although at some point it was considered a candidate for the pairing glue [62], the resonance has since been considered to be a general consequence of superconductivity in materials such as the cuprates (which exhibit d-wave superconductivity) with an order parameter that undergoes a sign change along the Fermi surface (see, e.g., [68]).

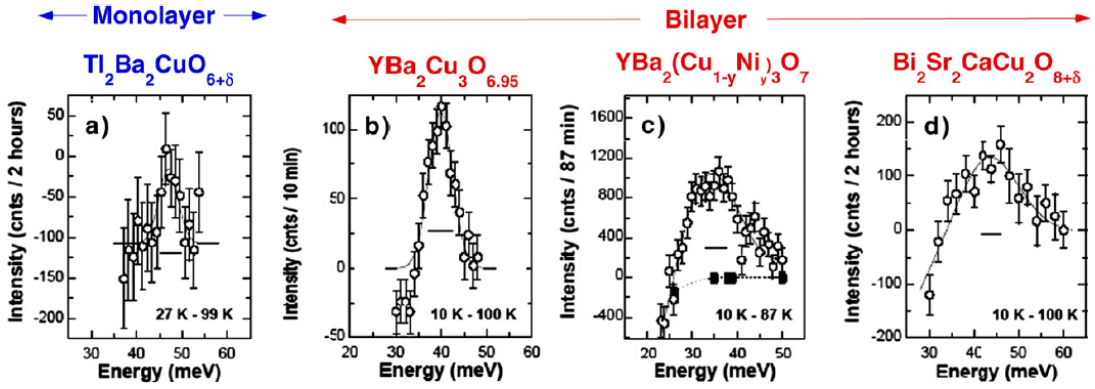

Figure 3.6: *Magnetic resonance in three different cuprates. The magnetic resonance is the enhancement of the magnetic response in the superconducting state at/near* $\mathbf{q}_{AF}$*. The magnetic resonance peak can be extracted from the difference between measurements performed at low temperature in the superconducting state and just above* T_c *in the normal state. In the differential spectra, the magnetic resonance peak appears as a positive net signal at* $\mathbf{q}_{AF}$ *and a well defined energy. The figure shows such difference spectra for: (a)* $Tl_2Ba_2CuO_{6+\delta}$ *(*$T_c \approx 90$ *K); (b)* $YBa_2Cu_3O_{6.95}$ *(*$T_c = 93$ *K); (c)* $YBa_2(Cu_{1-y}Ni_y)_3O_7$ *(*$T_c = 80$ *K); (d)* $Bi_2Sr_2CaCu_2O_{8+\delta}$ *(*$T_c = 91$ *K). Data are fitted to Gaussian profiles. The solid bars indicate the energy resolution [29].*

3.1.3 Gap Structure

The AF response may exhibit a gap (i.e., $\chi''(\mathbf{Q},\omega)$ goes to zero) below a certain characteristic energy Δ_{AF}. In LSCO, such a gap is not seen in underdoped samples. In 1995, a small gap at the incommensurate wave vectors was observed to open upon cooling into the SC state for a optimal-doped sample [69]. For moderately underdoped YBCO the gap appears at temperatures below T_c, and vanishes (or partially vanishes) upon warming across T_c (Figure 3.7(a)-(b) [64]), which indicates that, as for optimally-doped LSCO, it is connected to the SC gap. For highly underdoped SC $YBCO_{6.45}$ ($T_c = 35$ K), no gap is observed [71]. Instead similar to underdoped LSCO, SDW order is seen [71]. Point disorder and an applied magnetic field have been shown to create in-gap status or wash out the gap entirely [29].

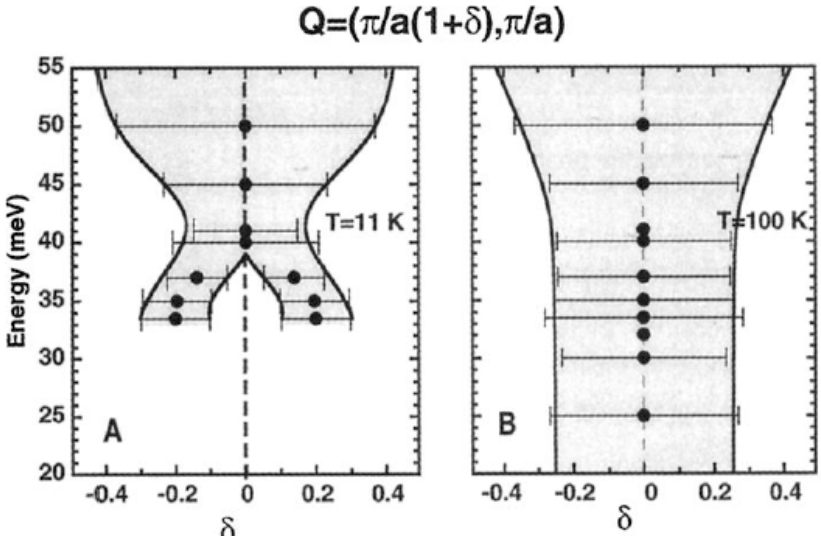

Figure 3.7: *Gap in the AF response of YBCO [64]. Overall momentum dependence of the magnetic response in* $YBCO_{6.85}$ *(T_c = 89 K) obtained (a) in the SC state at T = 11 K and (b) in the normal state at T = 100 K. No magnetic signal is disernible below $\Delta_{AF} \approx$ 32 meV at 11 K; the gap is (at least partially) filled at 100 K.*

3.2 Antiferromagnetic Response in Hg1201

Recent theoretical advances indicate that AF correlations may drive not only the d-wave superconductivity, but potentially also PG electronic instabilities such as charge order (CDW, bond-density wave), translational-symmetry-preserving loop-current order, and pair-density-wave order [30, 31, 74, 75]. These developments raise the prospect that much of the cuprate phase diagram may be understood as driven by AF correlations. It is therefore imperative to determine the detailed magnetic response in a structurally simple compound. Such measurements might also help illuminate the relevance of the seemingly universal hourglass response.

Hg1201 features the highest optimal T_c ($T_{c,max} = 97\ K$) of all single-CuO_2-layer cuprates, a simple tetragonal crystal structure, and minimal disorder effects [76]. Similar to the recent demonstration of the validity of Kohler's rule for the magnetoresistance in the PG phase [16], these model-system characteristics of Hg1201 can be expected to most clearly reveal the inherent magnetic fluctuation spectrum of the quintessential CuO_2 layers.

In what follows, we present both polarized and unpolarized neutron scattering results for the magnetic excitations in four underdoped Hg1201 samples with $T_c \approx 45$ K, 55 K, 71 K and 88 K, corresponding to approximate hole doping levels $p \approx 0.057$, 0.064, 0.090 and 0.115, and denoted as UD45, UD55, UD71 and UD88. Following the presentation of the time-of-flight data analysis method in Section 3.2.1, these results will be presented in chronological order of the measurements: first UD71 [78] (Section 3.2.2), then UD88 [79] (Section 3.2.3), then UD55 (Section 3.2.4), and then UD45 (Section 3.2.5).

3.2.1 Time-of-flight Data Analysis Method

The majority of our measurements of the AF response in Hg1201 were performed with the time-of-flight spectrometer ARCS at the Spallation Neutron Source at Oak Ridge National Laboratory. The samples were mounted such that the incoming beam was parallel to the crystallographic c-axes. This means that for a particular in-plane wave vector $\mathbf{q} = (H,\ K)$, the out-of-plane component L depends on the energy transfer. Usually, two incident energies were used, a lower one (e.g., 70 meV) with higher flux and better energy-momentum resolution at low energy transfers; and a higher one (e.g.,

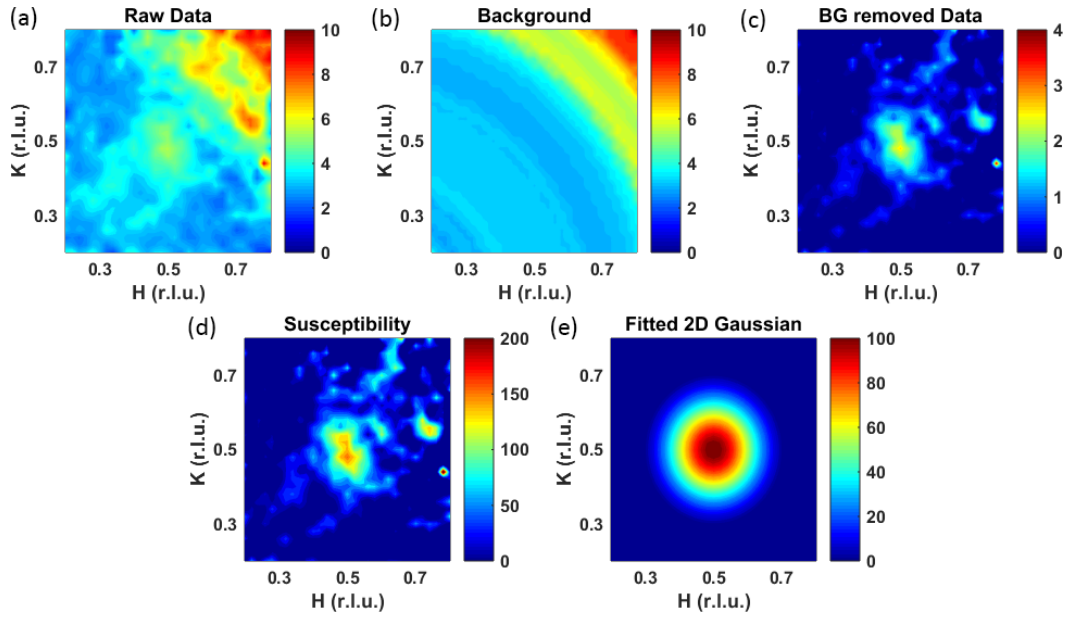

Figure 3.8: *Time-of-flight data analysis. (a) Raw data for UD55 at 10 K obtained on ARCS with E_i = 50 meV, binned in the range $\omega = 36 \pm 3$ meV. Only part of the first Brillouin zone is shown, which is the interesting region around $\mathbf{q}_{AF}$. The incoherent background has been estimated from a Vanadium test measurement and removed. (b) Ring-like background, estimated by averaging raw data within $|\mathbf{Q}|$-rings; data too close to $\mathbf{q}_{AF}$ (distance $\leq$ 0.1 r.l.u.) were not included in the average. (c) Data with ring-like background removed. (d) Magnetic susceptibility, obtained from (c) using Equation 3.1. (e) 2D Gaussian fit to (d), which describes the original data quite well. Colorbar to the right of each contour plot shows the respective scale.*

100 or 130 meV) with lower flux, in order to reach higher energy transfers.

Raw data were obtained from the ARCS database. The incoherent background was estimated by measureing the neutron scattering cross section of a piece of Vanadium with similar mass as the sample in a white incident beam (i.e., incident neutrons with a wide range of energies) and removed from the counted cross section. A factor that accounts for detector tube efficiency was applied to data collected with different detector tubes.The resultant 'raw' data were processed in three steps under the assumptions that the magnetic response arises from the quintessential CuO_2 planes, and hence is

quasi-two-dimensional, and that corrections for the weak L dependence can be made by accounting for the Cu magnetic form factor (see Section 1.2.2). The first step was to take constant-energy slices from database (see Section 2.2.3), and to isolate the AF response by removing an estimated background. The background mainly originates from ring-like powder scattering lines of the aluminum sample holder and from acoustic phonons, both of which depend on the magnitude of the wave-vector $\mathbf{Q}$. Therefore, the background is estimated by averaging the intensity of circular momentum slices, each centered at a given wave-vector magnitude $|\mathbf{Q}|$, at fixed energy transfer (Figure 3.8(b)); second, the background-removed data were normalized by the magnetic form factor and by the Bose population factor to obtain the magnetic susceptibility $\chi''(\mathbf{Q},\omega)$ (Figure 3.8c), according to Equation 1.18:

$$\frac{d^2\sigma}{d\Omega dE} = \frac{2(\gamma r_e)^2}{\pi g^2 \mu_B^2}\frac{k_f}{k_i}|f(\mathbf{Q})|^2\frac{\chi''(\mathbf{Q},\omega)}{1-e^{-\omega/k_BT}} \tag{3.1}$$

where the left side is the partial differential scattering cross section, $\gamma r_e = 0.2905$ barn $\cdot$ sr^{-1} is constant, the spin g-factor is 2, μ_B is the Bohr magneton, k_f and k_i are the final and incident neutron wave-vectors, $|f(\mathbf{Q})|^2$ is square of the magnetic form factor, and $1-e^{-\omega/k_BT}$ is the Bose factor. Finally, the susceptibility was fitted to the following azimuthally-symmetric 2D Gaussian function:

$$\begin{aligned}\chi''(\mathbf{Q},\omega) &= \chi_0'' e^{-4\ln 2\frac{R^2}{(2\kappa)^2}},\\ R &= |\sqrt{(H-0.5)^2+(K-0.5)^2}-\delta|,\end{aligned} \tag{3.2}$$

where δ parameterizes the incommensurability away from $\mathbf{q}_{AF}$ and 2κ is the full-width-at-half-maximum (FWHM). An example of such a fit is shown in Figure 3.8d for comparison with the experimentally-determined susceptibility χ'' in Figure 3.8c.

3.2.2 UD71

The work discussed in this Section was published in [78]. Whereas the published work shows analysis results by Mun Chan, in this and the following Sections all results are based on data analysis performed by the Thesis author. The two analysis results are highly consistent with each other. Figure 3.9(a)-(f) shows contour plots of the momentum dependence of the magnetic susceptibility χ'' in the first Brillouin zone for discrete

energy slices, extracted from raw neutron scattering data using the method described in Section 3.2.1. No signal is seen at low energies (e-f), whereas a strong commensurate peak appears at intermediate energies (c-d), and incommensurate ring-like features are observed at high energies (a-b).

Figure 3.9(g)-(l) shows the {1, 0}-dependence of magnetic susceptibility, extracted by averaging data along [1, 0] and [0 1] across $\mathbf{q}_{AF}$. The data were fit to an incommensurate 1D Gaussian function, $G_{1D} = \chi_0'' e^{-4\log 2(H-\delta)^2/FWHM^2}$, which is shown as solid lines; the incommensurability δ converges to zero at lower energy transfers. No peak is seen below the gap energy $\Delta_{AF} \approx 27$ meV, above which a commensurate peak appears at $\mathbf{q}_{AF}$ and finally disperses out at higher energies. These plots confirm the qualitative analysis based on the contour plots.

Data such as those in Figure 3.9(a)-(f) (ranging from $\omega = 6$ meV to 100 meV) were fit to Equation 3.2, and the detailed energy dependence of χ_0'', 2κ and δ was obtained. Due to the relatively weak signal at 220 K and 350 K, we did not attempt to extract FWHM and δ, but rather fixed these parameters to their average 5 K and 85 K values to obtain the amplitude χ_0''. Above Δ_{AF}, the low-energy magnetic response in UD71 is initially commensurate with $\mathbf{q}_{AF}$, i.e., $\delta = 0$ was found to give the best fit to the data. The confidence of the fit was calculated by its Jacobian, and an upper bound of $\delta \approx 0.03$ r.l.u. was estimated, consistent with the instrumental momentum resolution (the latter is indicated as white circles in the left most contour panels). The high-energy magnetic response is incommensurate, with increasing δ as ω increases. Rather than an hourglass shape, both in the SC and non-SC state the $\mathbf{q}_{2D}$-ω response of UD71 has a gapped wine-glass shape; its 2D $\mathbf{q}$-ω projection is Y-shaped rather than X-shaped.

Figure 3.10a shows the energy dependence of the magnetic susceptibility amplitude χ_0'' at four temperatures. A comparison of the data at 5 K and 85 K reveals hardly any effect of superconductivity. This is highlighted in Figure 3.10b, which shows the change $\Delta\chi_0''$ between these two temperatures. In order to better ascertain the temperature dependence of magnetic excitations, the response at $\omega_p \approx 51$ meV and $\mathbf{q}_{AF}$ was measured on a triple-axis spectrometer from 4 K to above room temperature (Figure 3.11(c)). Consistent with Figure 3.10, the response does not exhibit an abrupt change across T_c, which confirms the lack of a magnetic resonance. However, a marked increase occurs below the PG temperature T^*, similar to the IUC magnetic order (see Chapter 4), which

indicates that the strength of the AF response is correlated with the PG phase. Figure 3.10(c)-(d) shows results for the momentum-integrated local susceptibility,

$$\chi''_{loc}(\omega) = \frac{\int \chi''(\mathbf{Q},\omega)\, d^2q}{\int d^2q}. \tag{3.3}$$

As for χ''_0, χ''_{loc} reveals a much more significant enhancement in the PG state than upon cooling into the SC state. The magnetic nature of the response was confirmed through a spin-polarized triple-axis neutron scattering experiment: Figure 3.11(a)-(b) show pure magnetic signal extracted via LPA (see Section 2.2.2). The experiment was performed on the polarized spectrometer IN20 at Institut Laue Langevin.

Figure 3.12 shows the contour plot of $(H, 0)$-ω dependence of the AF response, data are generated by the 2D Gaussian fit results. We note that as the high temperature data at 220 K and 300 K have worse signal-noise ratio, the incommensurability δ and FWHM were fixed to be the same as those at 70 K during the fit process, and the 5 K, 85 K and 220 K data were collected with $E_i = 70$ meV and 130 meV, whereas the 300 K data were collected only with $E_i = 70$ meV, so only low energy transfers at 300 K are shown.

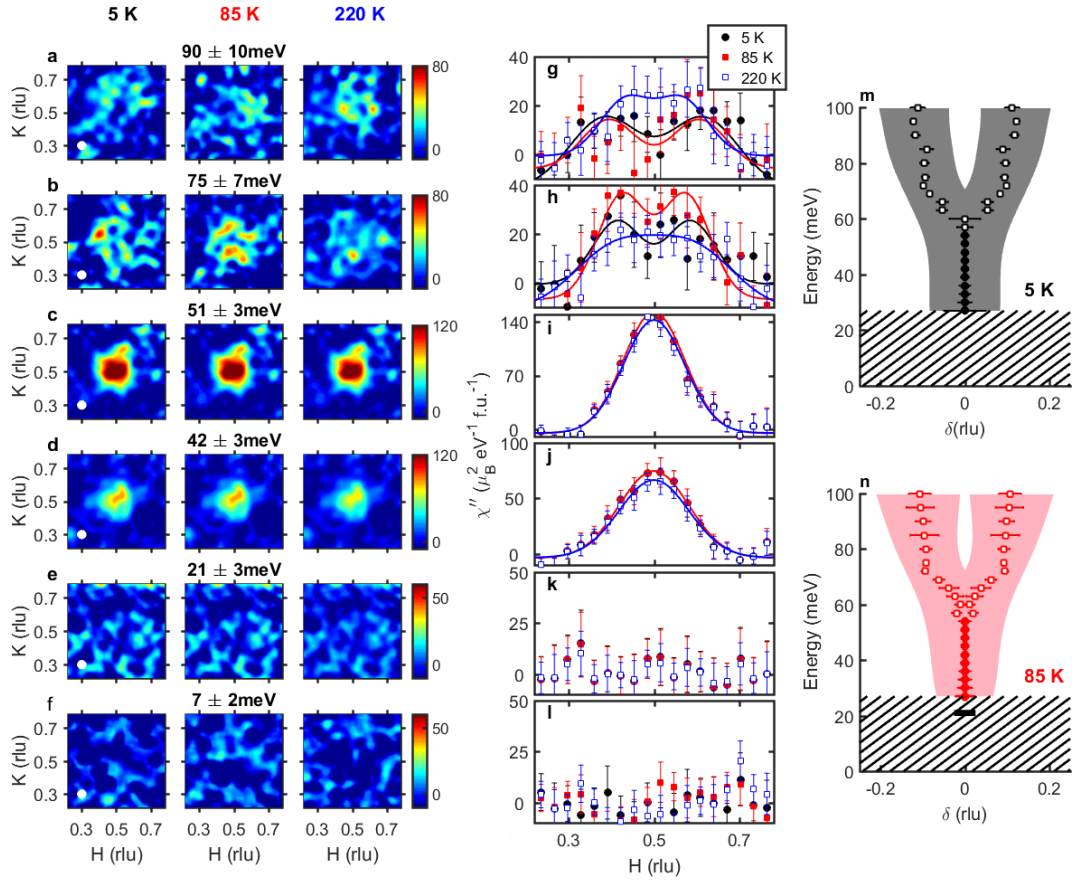

Figure 3.9: *AF response of UD71. (a-f) Constant-energy images of magnetic susceptibility at T = 5 K (left), 85 K (middle) and 220 K (right), in units of* $\mu_B^2 eV^{-1} f.u.^{-1}$. *Data are sliced at indicated energy transfers* ω *and averaged within indicated energy windows. White dots (left-most panels): FWHM momentum resolution at each value of* ω. *(g-l) Corresponding constant-*ω *cuts across* $\mathbf{q}_{AF}$, *averaged over [1, 0] and [0, 1] trajectories. Solid lines: 1D Gaussian fits to data convolved with the momentum resolution. The apparent magnitude of the susceptibility peak value is slightly lower than the actual value due to the averaging over the binning ranges K(H) = [0.38, 0.62] r.l.u. (m,n) Energy dependence of incommensurability* δ *at 5 K (black) and 85 K (red), extracted from 2D Gaussian fits to constant-*ω *data such as those in a-f. Horizontal error bars: fit uncertainties for* δ. *Filled circles and open squares: data taken with incident neutron energy* $E_i = 70\ meV$ *and 130 meV, respectively. Grey and pink regions: FWHM of the response. Grey hatched area: magnetic excitation gap* ($\Delta_{AF} \approx 27\ meV$). *Horizontal black bar in n: FWHM momentum resolution at* $\omega = 20\ meV$.

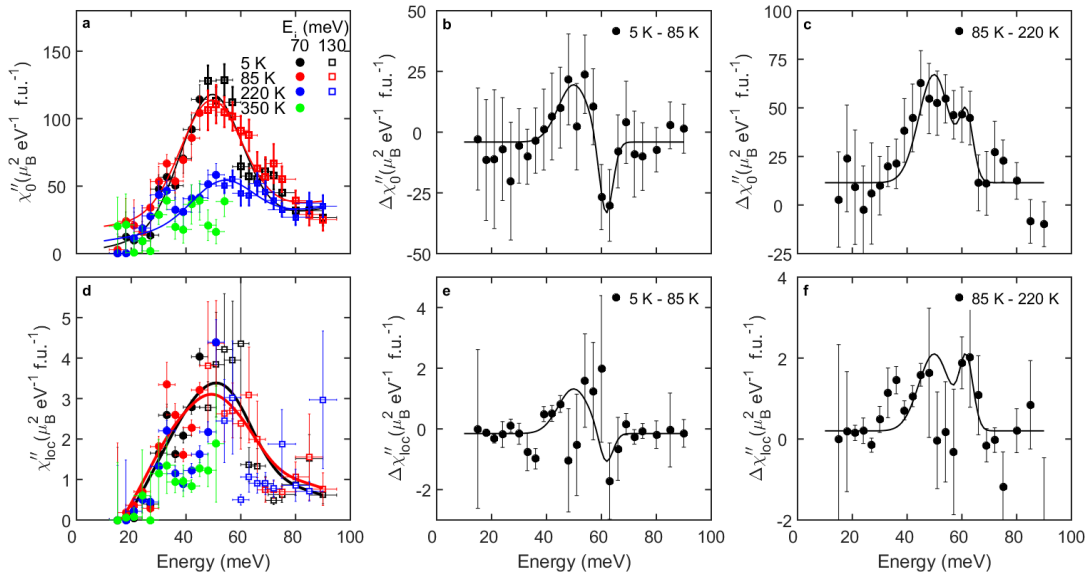

Figure 3.10: *Magnetic susceptibility amplitude and local susceptibility for UD71. (a) Energy dependence of the magnetic susceptibility amplitude χ_0'', determined from 2D fits to background-corrected data such as those in Figure 3.9(a)-(f). Circles: E_i = 70 meV. Squares: E_i = 130 meV. Solid black and red lines: Gaussian fits to 5 K and 85 K data. (b) Difference of χ_0'' at 5 K, deep in the superconducting state, and at 85 K, 14 K above T_c. No obvious resonance is seen, but an S-shaped feature appears at about the neck energy (see Figure 3.9m,n). Solid line: guide to eyes. (c) Difference of χ_0'' at 85 K and 220 K, which highlights the evolution of the response in the PG state ($T^* \approx$ 300 K) for this sample (see also Figure 3.11c). Solid line: guide to eyes. (d-f) Similar results for the local susceptibility χ_{loc}''. The spike at $\sim$ 30 meV is possibly the result of complications due to additional phonon scattering (see [78] for detailed information). Solid lines: guide to eyes.*

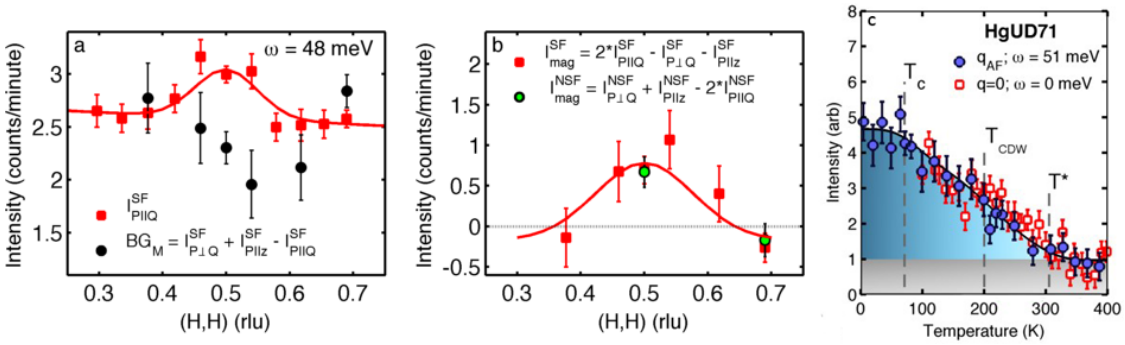

Figure 3.11: *Triple-axis specterometer measurements of AF response in UD71. (a) Rocking-scan of spin-flip (SF) scattering about* $\mathbf{Q}$ *= (0.5, 0.5, 3.5) at* ω *= 48 meV and* T *= 2 K (red squares) for initial neutron spin polarization* $P \parallel \mathbf{Q}$*. The background level for magnetic scattering is determined from LPA (black circles) through additional measurements in the two other principal geometries,* $P \parallel z$ *and* $P \perp \mathbf{Q}$*. Excess magnetic scattering above the background level is clearly observed at* $\mathbf{q}_{AF}$*. (b) The intensity measured in the three SF geometries can be used to extract the pure magnetic scattering (red squares). This is confirmed through a corresponding NSF measurement (green circles). (c) Temperature dependence of inelastic magnetic scattering at* $\mathbf{q}_{AF}$ *and* ω_p *= 51 meV and of the IUC magnetic order (Chapter 4) measured on separate Hg1201 samples with similar doping levels (*T_c *= 71 K and 75 K, respectively). The* $\mathbf{q}$ *= 0 signal appears below* $T_{q=0}$ *=320* $\pm$ *20 K, whereas the increase of inelastic signal at* $\mathbf{q}_{AF}$ *occurs below* T_{AF} *= 300* $\pm$ *15 K. Both temperatures coincide with the pseudogap temperature* T^* *from transport measurements [13]. The magnetic response appears to be unaffected by the appearance of CDW order, which occurs below* $T_{CDW} \approx$ *200 K at the studied doping level [72, 73].*

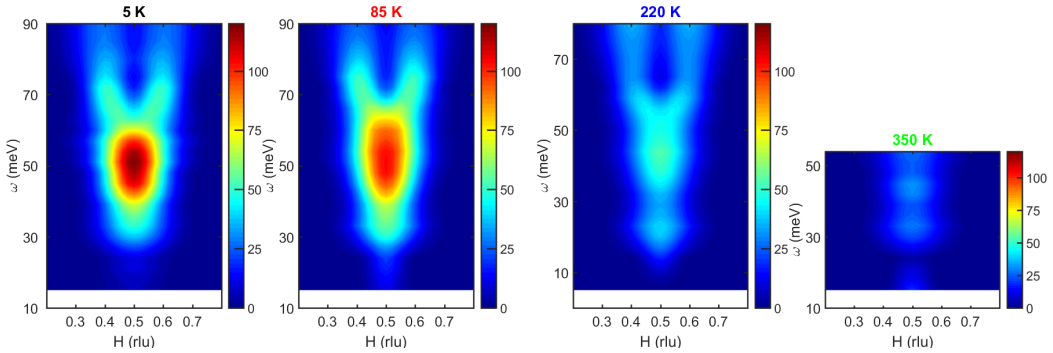

Figure 3.12: *Dispersion of AF response in UD71.* $\chi_0''(H,\omega)$ *contours are determined from 2D Gaussian fit to data such as those shown in Figure 3.9 for (a) 5 K; (b) 85 K; (c) 220 K and (d) 350 K. At 220 K and 350 K, the incommensurability* δ *and FWHM were fixed to be the same as those at 85 K. The 350 K data were collected with* $E_i = 70$ *meV, so only low energy transfers are shown.*

3.2.3 UD88

The work discussed in this Section was published in Ref. [79]. As for UD71, the data analysis in the published work was performed by Mun Chan, whereas the analysis in this Section was performed by the Thesis author; the two results are highly consistent with each other. Figure 3.13 shows contour plots of constant-ω slices, cuts averaged over [1, 0] and [0 1], and a summary of the dispersion deep in the SC state at 5 K, and just above T_c at 100 K. The figure is analogous to Figure 3.9 for UD71. Unlike for UD71, for UD88 at 5 K the gapped spectrum evolves with increasing energy from an incommensurate ring that disperses toward $\mathbf{q}_{AF}$ and then outward again, and thus exhibits an hourglass dispersion (Figure 3.13m). At $T = 100$ K, however, the low-energy response is commensurate, resulting in a wineglass dispersion (Figure 3.13n). The gap $\Delta_{AF} \approx 42$ meV and is unchanged across T_c. Finally, at $T = 250$ K, just above $T^* \approx 220$ K, the response is considerably weaker than deep in the PG state at 100 K. Moreover, the response at $\omega \approx 60$ meV, where the upward dispersion begins, is significantly larger at 5 K than at 100 K, which indicates the restoration of a resonance at this doping level, consistent with previous work on optimally-doped ($T_c \approx 95$ K) Hg1201 [67]. Indeed, an obvious resonance feature is seen in the ω-dependence of both the peak and local susceptibilities, as shown in Figure 3.14. Figure 3.15 shows contour plots analogous to Figure 3.12, determined from the 2D Gaussian fit results. The hourglass dispersion and resonance in the SC state are consistent with the AF response of moderately underdoped YBCO [29, 64].

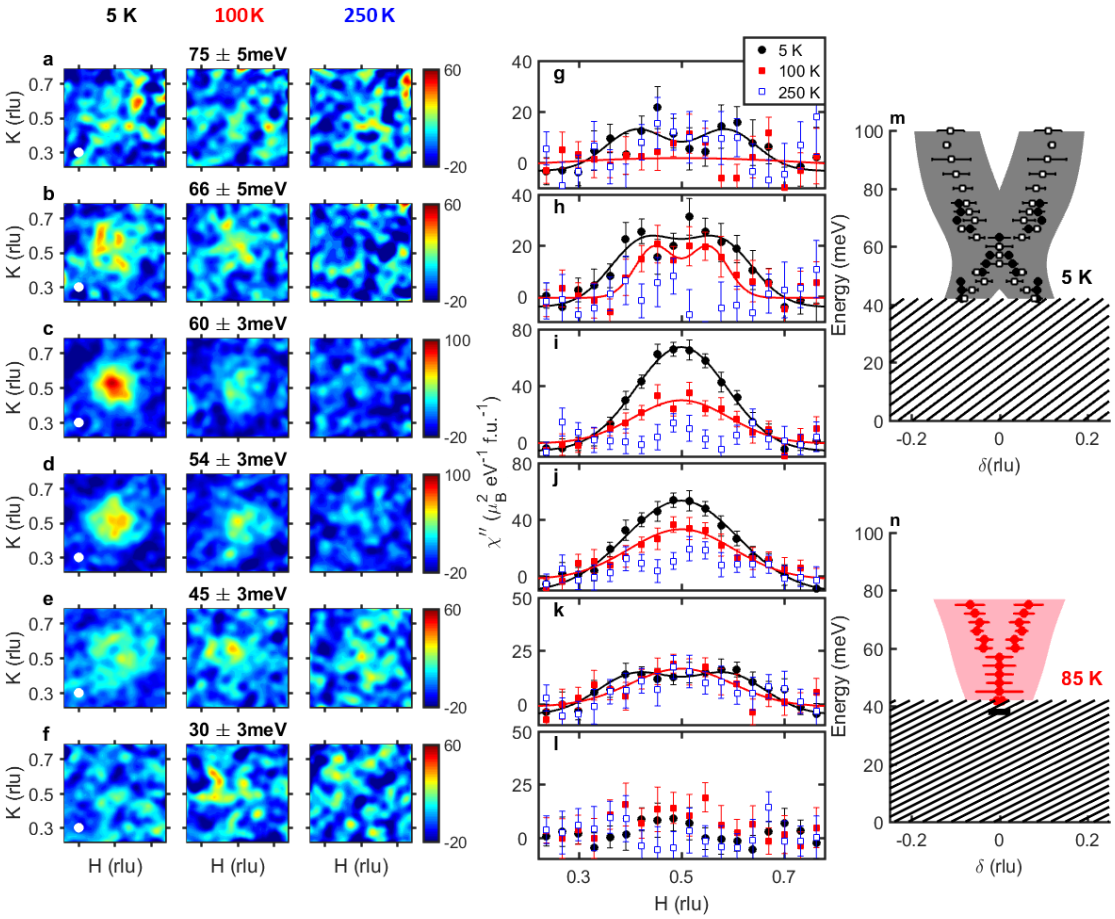

Figure 3.13: *AF response of UD88. This figure is closely analogous to Figure 3.9 for UD71. (a-f) Constant-energy images of magnetic susceptibility at T = 5 K (left), 100 K (middle) and 250 K (right). (g-l) Corresponding constant-ω cuts across* $\mathbf{q}_{AF}$*, averaged over [1, 0] and [0, 1] trajectories. Solid lines: 1D Gaussian fits to data convolved with the momentum resolution. (m,n) Energy dependence of incommensurability δ at 5 K (black) and 100 K (red).*

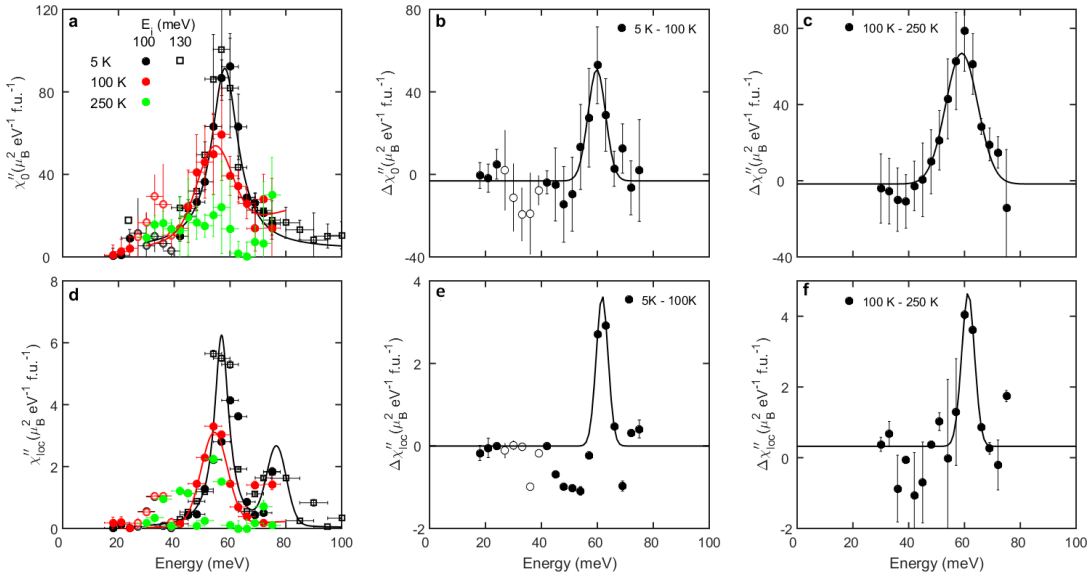

Figure 3.14: *Magnetic susceptibility amplitude and local susceptibility for UD88. This figure is closely analogous to Figure 3.10 for UD71. (a) Energy dependence of* χ_0''*. Circles:* $E_i = 100$ *meV. Squares:* $E_i = 130$ *meV. Solid black and red lines: Lorentzian fit to 5 K and 100 K data. (b) Difference of* χ_0'' *at 5 K and at 100 K. A strong resonance peak is seen. The solid line is a Gaussian fit with magnitude* $= 54.1 \pm 11.2\ \mu_B^2 eV^{-1} f.u.^{-1}$*, center* $= 59.8 \pm 0.8$ *meV, FWHM* $= 7.4 \pm 1.5$ *meV. (c) Difference of* χ_0'' *at 100 K and at 250 K. The solid line is a Gaussian fit with magnitude* $= 68.7 \pm 8.4\ \mu_B^2 eV^{-1} f.u.^{-1}$*, center* $= 59.0 \pm 0.5$ *meV, FWHM* $= 13.6 \pm 1.7$ *meV. (d-f) Similar results for the local susceptibility* χ_{loc}''*. Solid lines in e and f are Gaussian fits with (e) magnitude* $= 3.63 \pm 0.95\ \mu_B^2 eV^{-1} f.u.^{-1}$*, center* $= 61.7 \pm 5.54$ *meV, FWHM* $= 4.97 \pm 0.92$ *meV; and (f) magnitude* $= 4.34 \pm 0.29\ \mu_B^2 eV^{-1} f.u.^{-1}$*, center* $= 61.3 \pm 0.24$ *meV, FWHM* $= 5.43 \pm 0.48$ *meV. For* $E_i = 100$ *meV, the energy resolution at* $\omega \approx 60$ *meV is approximately 3 meV (FWHM).*

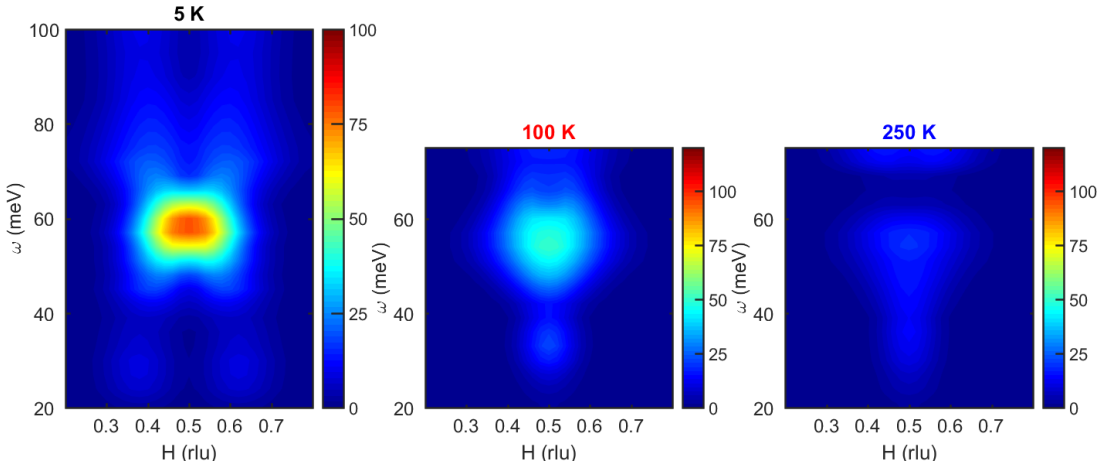

Figure 3.15: *Dispersion of AF response in UD88.* $\chi_0''(H,\omega)$ *contours are determined from 2D Gaussian fit results to data such as those shown in Figure 3.13 for (a) 5 K; (b) 100 K and (c) 250 K. At 250 K, the incommensurability* δ *and FWHM were fixed to be the same as those at 85 K. The 85 K and 250 K data were collected with lower incident energy.*

3.2.4 UD55

This sample has a particularly interesting doping level ($p \approx 0.064$). In light of the unusual result for UD71 (Section 3.2.2), it is important to extend previous study of the AF response of Hg1201 to lower doping and check if the features observed in UD71 are unique to that doping level. Moreover, it has been shown that CDW correlations are weak for underdoped samples with T_c below 60 K [72, 73], so we can rule out the possibility that such correlations significantly influence the magnetic response. As such, the observed behaviour in UD55 signifies the unmasked response of the quintessential CuO_2 planes in the PG and SC states near the undoped AF Mott-insulating state.

In this Section, we report a detailed neutron scattering study of UD55 and uncover the fundamental AF response of the CuO_2 planes below 140 meV in close proximity to the parent insulating state. As in the prior work on UD71 and UD88, we primarily report time-of-flight measurements. In order to confirm the magnetic nature of the response, we present complementary triple-axes data with neutron polarization analysis.

The ring-like background is estimated using the same method as for UD71 and UD88, and removed from the raw data. This is demonstrated for $\omega = 15$ meV, 30 meV and 95 meV in Figures 3.16, 3.17, and 3.18, respectively. We note that the background subtraction method does not entirely remove contributions of phonons or Ising-like modes (see Chapter 5). Therefore, one sees a spike in the energy dependnece of FWHM and χ''_{loc} for UD55 (see Figure 3.23d) at about 30 meV, whereas χ''_0 is not affected (see Figure 3.23a).

The background-subtracted data were fit to a 2D Gaussian function, as described in the main text, in order to extract the peak susceptibility, incommensurability δ and FWHM $= 2\kappa$ of the magnetic response. Due to the relatively weak signal at 410 K, the $E_i = 70$ and 200 meV data were fit with 2κ and δ fixed to their average 5 K and 70 K values to obtain the amplitude. Contour plot of the background-subtracted data and corresponding fit results for $\omega = 15$ meV, 30 meV and 95 meV are shown in Figure 3.19.

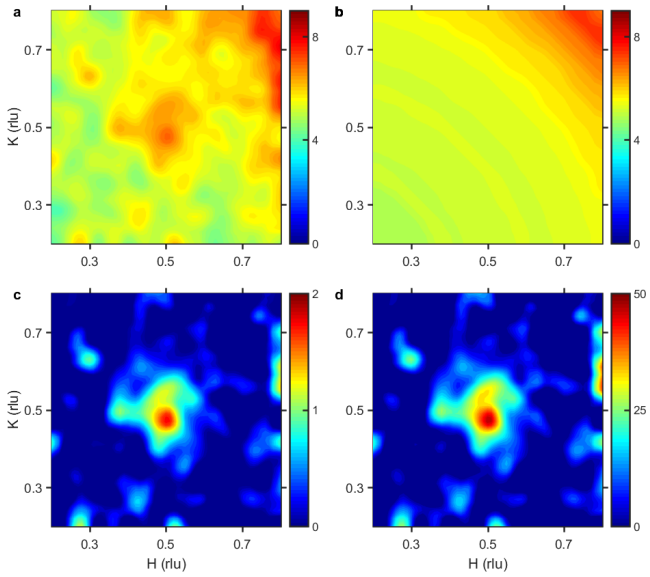

Figure 3.16: *TOF data processing for UD55 - example 1: E_i = 70 meV, ω = 15 ± 3 meV, T = 70 K. (a) Constant-energy slice (ω = 15 ± 3 meV) of the raw data in the first Brillouin zone shows the cross section in arbitrary units. (b) 'Background' estimate $BG(\omega, \mathbf{Q})$, determined as described in Section 2.2.3 and 3.2.1. (c) Resultant net intensity. (d) $\chi''(\mathbf{Q}, \omega)$ in absolute units, obtained as describe in Section 2.2.3 and 3.2.1.*

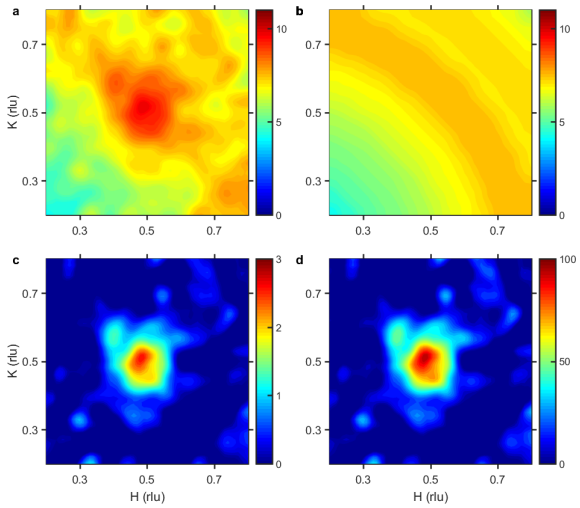

Figure 3.17: *TOF data processing for UD55 - example 2: E_i = 70 meV, ω = 30 $\pm$ 3 meV, T = 70 K. (a) - (d) Similar to Figure 3.16.*

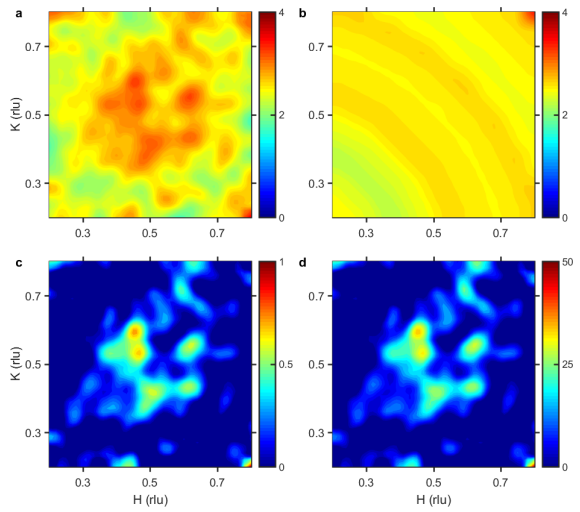

Figure 3.18: *TOF data processing for UD55 - example 3: E_i = 200 meV, ω = 95 $\pm$ 10 meV, T = 70 K. (a) - (d) Similar to Figure 3.16 and 3.17.*

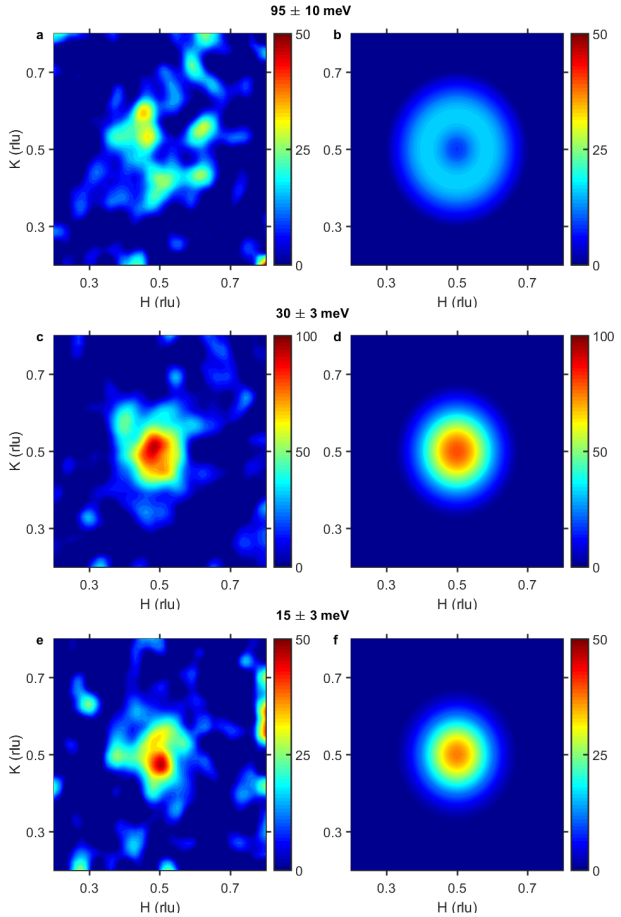

Figure 3.19: *2D Gaussian fits to background-subtracted data. (a) Same data as Figure 3.18: $\omega = 95 \pm 10$ meV at $T = 70$ K. (b) Result of fit to 2D incommensurate Gaussian function convoluted with the instrument momentum resolution for data in (a). (c)-(d) Corresponding data (same as Figure 3.17) and fit for $\omega = 30 \pm 3$ meV at $T = 70$ K. (c)-(d) Corresponding data (same as Figure 3.16) and fit for $\omega = 15 \pm 3$ meV at $T = 70$ K.*

We analyzed data at various energy transfers: from $\omega = 9$ meV to 54 meV in 3 meV steps, with a $\pm$ 3 meV bin range; from $\omega = 60$ meV to 75 meV in 5 meV steps, with a $\pm$ 7 meV bin range; from $\omega = 85$ to 95 meV in 10 meV steps, with a $\pm$ 10 meV bin range; from $\omega = 115$ to 130 meV in 15 meV steps, with a $\pm$ 15 meV bin

range. Figures 3.20, 3.21 and 3.22 show extensive data at T = 5 K, 70 K and 410 K. Figures 3.21f,l and 3.22g,n demonstrate that no coherent AF signal is discernible at ω = 9 meV and 6 meV, respectively, whereas Figures 3.21e and 3.22f demonstrate nearly resolution-limited commensurate AF signal at ω = 18 meV and 15 meV, respectively. As seen from these figures, the response remains commensurate up to ω = 54 meV, and then disperses outward and takes on a ring-like shape at high energy transfers. We emphasize that the FWHM of the AF signal centered at $\mathbf{q}_{AF}$ decreases with decreasing ω and approaches the instrument resolution (shown by white dots in the left panels of all these figures). This demonstrates that the low-energy AF response is indeed commensurate. Also shown in these figures are constant-ω cuts across $\mathbf{q}_{AF}$, averaged over [1, 0] and [0, 1] with bin range 0.4 - 0.6 r.l.u., along with Gaussian fits. At lower energies, the fits coverge to a commensurate Gaussian. The energy dependences of 2κ and δ are shown in Figure 3.22o-p. It is clear from both the contour plot and the energy dependence of δ that the AF response at 5 K and 70 K is commensurate at energy transfers below $\omega_c \approx 55$ meV and approaches the momentum-resolution limit at low ω. The results at 410 K are consistent with these observations, e.g., a weak commensurate signal is seen at 30 meV, whereas the response at 75 meV is incommensurate. As before, we fixed 2κ and δ at high temperature (410 K) to the low temperature value (average of 5 K and 70 K results) to obtain the amplitude χ_0''. We do not see a difference between the response at 5 K and 70 K, except for $\omega \sim 30$ meV (where χ_0'' is largest; Figure 3.22l), which indicates the potential existence of a weak resonance in the SC state. Figures 3.22g,n reveal a $\Delta_{AF} \approx 6$ meV gap at both 5 K and 70 K, which we define here as the energy below which there is no discernible signal in the present experiment. Above $\omega \sim 90$ meV, the response is relatively weak and rather similar at all three temperatures.

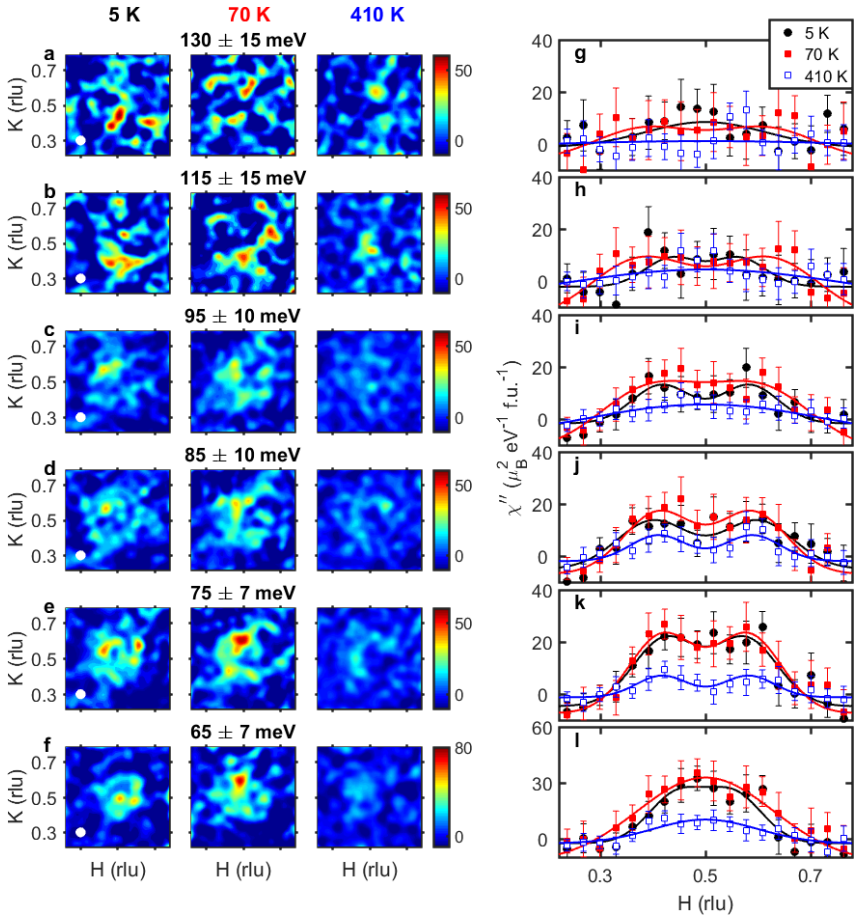

Figure 3.20: *Magnetic excitations in UD55 - high energy transfers (E_i = 200 meV). (a)-(f) Constant-energy contours of magnetic susceptibility at T = 5 K, 70 K and 410 K. Data centered at indicated energies are averaged within indicated energy windows. White dots (left-most panels): momentum resolution. Right panels: Corresponding constant-energy cuts averaged over [1 0] and [0 1] trajectories across* $\mathbf{q}_{AF}$ *within momentum transfer binned from 0.4 to 0.6 r.l.u.. Solid lines: Gaussian fits to data convolved with the momentum resolution. Due to the averaging over momentum, the apparent signal in the right panels is slightly lower than the actual values shown in the contour plots.*

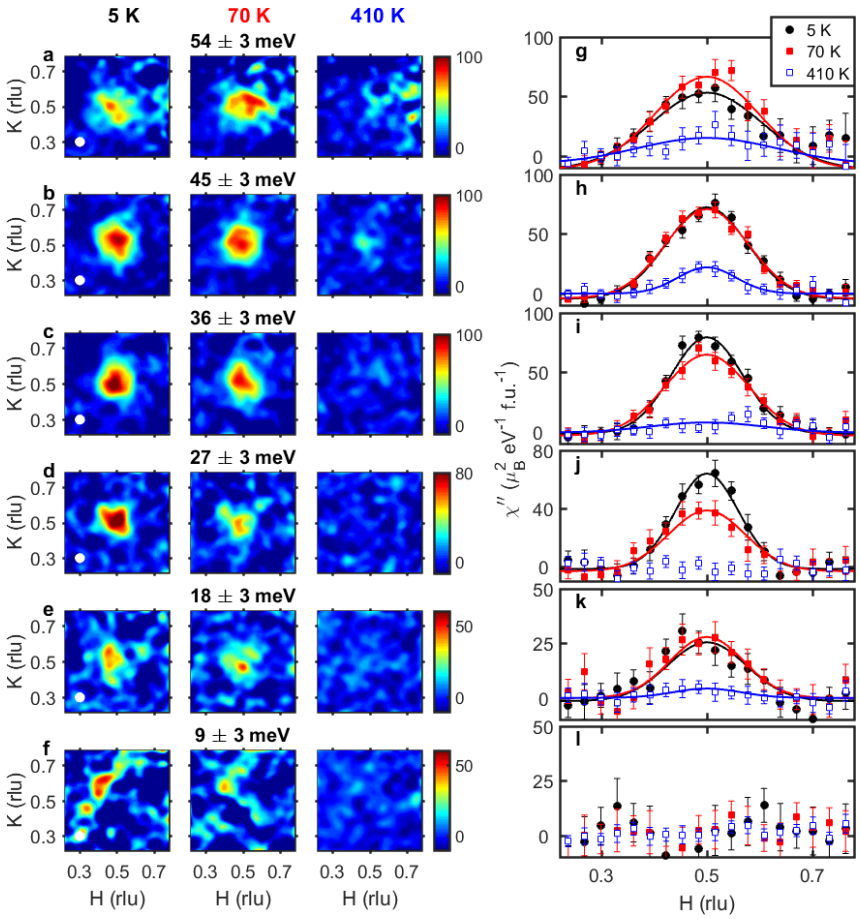

Figure 3.21: *Magnetic excitations in UD55 - low energy transfers (E_i = 70 meV). This figure is analogous to Figure 3.20 for E_i = 200 meV.*

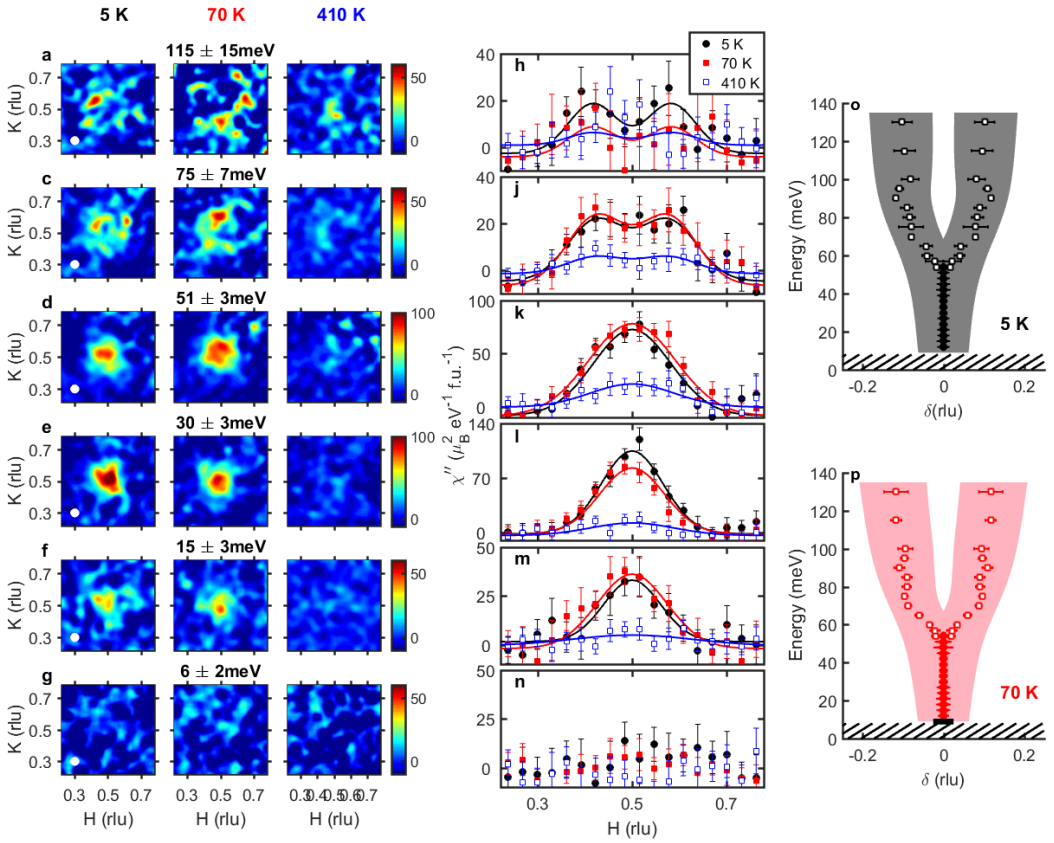

Figure 3.22: *AF response of UD55. This Figure is analogous to Figure 3.9 and Figure 3.13 for UD71 and UD88. (a-f) Constant-energy images of magnetic susceptibility at $T = 5$ K (left), 70 K (middle) and 410 K (right). (g-l) Corresponding constant-ω cuts across $\mathbf{q}_{AF}$, averaged over [1 0] and [0 1] trajectories. Solid lines: Gaussian fits to data, convolved with the momentum resolution. (m,n) Energy dependence of incommensurability δ at 5 K (black) and 70 K (red).*

Figures 3.23a-c show, respectively, the amplitude $\chi_0''(\omega)$ at 5 K, 70 K and 410 K (obtained with incident neutron energies $E_i = 70$ and 200 meV) and the corresponding change $\Delta\chi_0''(\omega)$ across T_c and T^*. Figures 3.23d-f show the corresponding results for the momentum-integrated local susceptibility and its change $\Delta\chi_{loc}''(\omega)$ across T_c and T^*. The large spike at ~ 30 meV in the local susceptibility is seen to result from a corresponding spike in the width of the response (Figure 3.23d inset), which we ascribe

to additional phonon scattering [78] or the flat mode (see Chapter 5). While phonon-related contamination in the 30 - 36 meV range affects the local susceptibility, this does not seem to be the case for $\chi_0''(\omega)$. In contrast to the resonance-like enhancement of the peak susceptibility in the 24 - 39 meV range, there exists an overall spectral weight loss upon cooling into the SC state: the local susceptibility undergoes a pronounced decrease in the 48 - 65 meV range, i.e., approximately centered at the characteristic energy $\omega_c \approx 55$ meV of the wine-glass-shaped response. Energy-integration of the local susceptibility up to 135 meV yields a total susceptibility of about 0.144 ± 0.012 and $0.171 \pm 0.016\ \mu_B^2$ at 5 K and 70 K, respectively, i.e., a small decrease upon cooling into the SC state.

Figure 3.24a shows $\chi_0''(\omega)$ at a number of temperatures in the commensurate region below 45 meV, obtained with $E_i = 50$ meV. As already seen in Figure 3.23a for 5 K and 70 K, this observable exhibits smooth non-monotonic energy dependence at all temperatures. It is fairly well fit with the heuristic damped-oscillator function $\chi_0'' = Re(\chi)\,\omega\Gamma\frac{\omega_0^2}{\left(\omega^2-\omega_0^2\right)^2}$. Figure 3.24b illustrates the difference between the damped-oscillator fit and the simple smooth function in Figure 3.23a. The main difference is around 30 meV, where the damped-oscillator model gives a very strong peak, whereas the smooth function in Figure 3.23a, which is based on more extensive data up to higher energy, shows a much broader peak.

A comparison of time-of-flight results and polarized triple-axis results is shown in Figure 3.24c. The magnetic signal at $\mathbf{q}_{AF}$ extracted from LPA from both momentum and energy scans agrees nicely with the magnetic susceptibility measured on the time-of-flight spectrometer. Figure 3.24d shows an elastic ($\omega = 0$) momentum scan across $\mathbf{q}_{AF}$, with the scattering path shown in inset. The blue crosses in both the main figure and inset indicate the position where strong spin-density-wave (SDW) correlations appear at low doping levels for YBCO and LSCO. In UD55, we do not see any signature of SDW order. Using the known cross section of the (0 0 4) nuclear Bragg peak (which is 4.2 barn) for comparison, we estimate the upper bound of a possible elastic AF signal to be 0.4 mbarn.

We performed a measurement of the temperature dependence of the susceptibility at 30 meV, where the enhancement of χ_0'' is largest (see Figure 3.23). The result is shown in Figure 3.25. We counted the intensity at $\mathbf{q}_{AF}$ in 5 K steps from 5 K to 450 K, and

also performed full-range rocking scans across $\mathbf{q}_{AF}$ in the first Brillouin zone at select temperatures. The background was determined from an average of the intensities at momentum transfers far away from $\mathbf{q}_{AF}$ from these rocking scans, and then smoothed to a line as a function of temperature. In order to better view the data, we averaged the intensities at $\mathbf{q}_{AF}$ every 20 K, and subtracted the corresponding background intensity given by the smooth background line. The temperature dependence of the subtracted susceptibility is shown in Figure 3.25b, along with the results from 2D Gaussian fits of the ARCS data. We see that the two results agree with each other within the errorbars. Evidence for a possible weak resonance is seen across T_c.

Figure 3.26 shows a contour plot of the (H-ω) dependence of the AF response, similar to Figure 3.12 for UD71. We see a clear Y-shaped dispersion at all three temperatures.

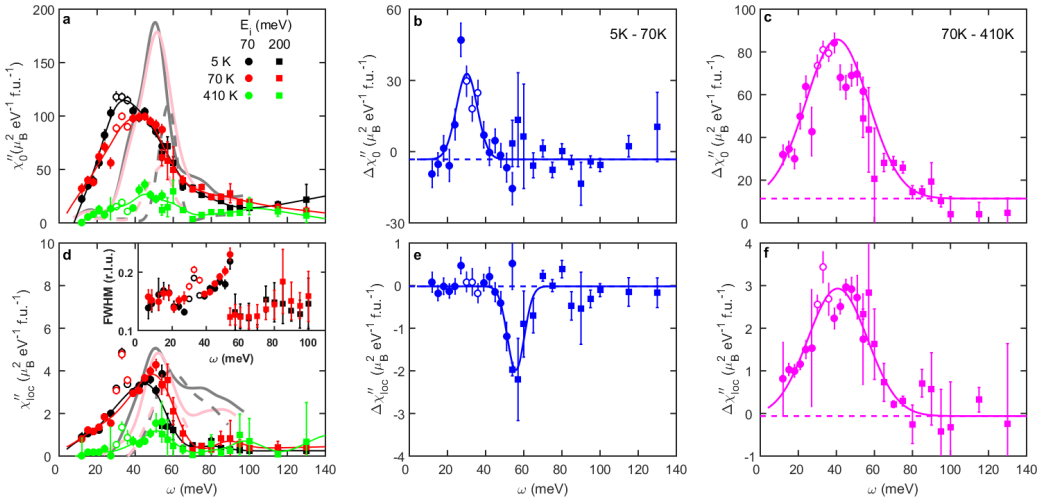

Figure 3.23: *Magnetic susceptibility amplitude and local susceptibility for UD55. This Figure is analogous to Figure 3.10 and Figure 3.14 for UD71 and UD88. (a) Energy dependence of* χ_0''*. Circles:* E_i *= 70 meV. Squares:* E_i *= 200 meV. Solid lines: smooth fit to the data. (b) Difference of* χ_0'' *at 5 K and at 70 K. A weak resonance peak is seen. Gaussian fit parameters: magnitude = 36.1 ± 5.6* $\mu_B^2 eV^{-1} f.u.^{-1}$*, center = 30.1 ± 0.9 meV, FWHM = 12.9 ± 2.3 meV. (c) Difference of* χ_0'' *at 70 K and at 410 K. Solid line is a Gaussian fit with parameters: magnitude = 74.5 ± 4.4* $\mu_B^2 eV^{-1} f.u.^{-1}$*, center = 40.4 ± 0.8 meV, FWHM = 38.9 ± 2.5 meV. (d-f) Similar results for the local susceptibility. The spike at* $\sim$ *30 meV in d is possibly a result of complications due to additional phonon scattering (see [78] for detailed information about this phonon), which is also captured by the FWHM as shown in inset. Solid lines in (e) and (f) are Gaussian fits with fit parameters for (e) magnitude = -1.97 ± 0.33* $\mu_B^2 eV^{-1} f.u.^{-1}$*, center = 55.8 ± 1.5 meV, FWHM = 10.4 ± 2.5 meV; and (f) magnitude = 2.99 ± 0.23* $\mu_B^2 eV^{-1} f.u.^{-1}$*, center = 40.7 ± 0.82 meV, FWHM = 36.8 ± 3.9 meV.*

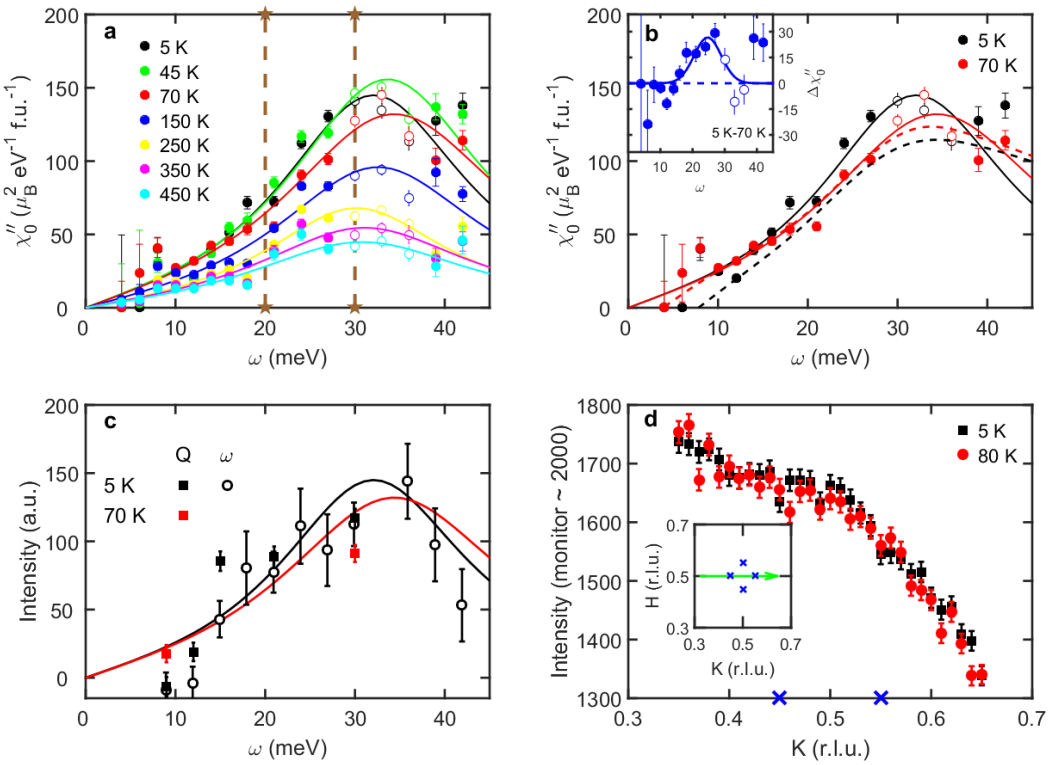

Figure 3.24: *Temperature dependence, polarized neutron result, and search for quasistatic magnetism in UD55. (a) Temperature dependence of χ_0'' measured with E_i = 50 meV up to ω = 42 meV. Solid lines: fits to the damped-oscillator function as described in the text, which does not account for the gap. (b) Comparison of the damped-oscillator fit (solid lines, same as in a) and smoothed fit (dashed lines; same as in Figure 3.23a). Inset: Gaussian fit to the difference between 5 K and 70 K data in a, with peak magnitude 26.7 ± 6.7 $\mu_B^2 eV^{-1} f.u.^{-1}$, peak center 24.7 ± 1.3 meV, and FWHM 9.9 ± 3.0 meV. (c) Comparison of energy dependence of AF response (solid lines are same as in a) with a polarized-neutron triple-axis scattering result. Black and red squares: χ_0'' obtained from momentum scans at chosen constant energies. Blue open circles: energy scans at $\mathbf{q}_{AF}$ and two background momentum transfers. Time-of-flight data are obtained in absolute units; triple-axis data are scaled to match the former. The combined data demonstrate the AF nature of the signal and the absence of a phonon contamination of χ_0''. (d) Momentum scan along [0 1 0] across $\mathbf{q}_{AF}$ at 5 K (black squares) and 80 K (red circles). Blue crosses: the locations where SDW/stripe order is observed at a similar doping level in LSCO (x = 0.06) [80]. Inset: schematic of the momentum-scan range (green line) and characteristic wave vector in LSCO at x = 0.06 (blue crosses).*

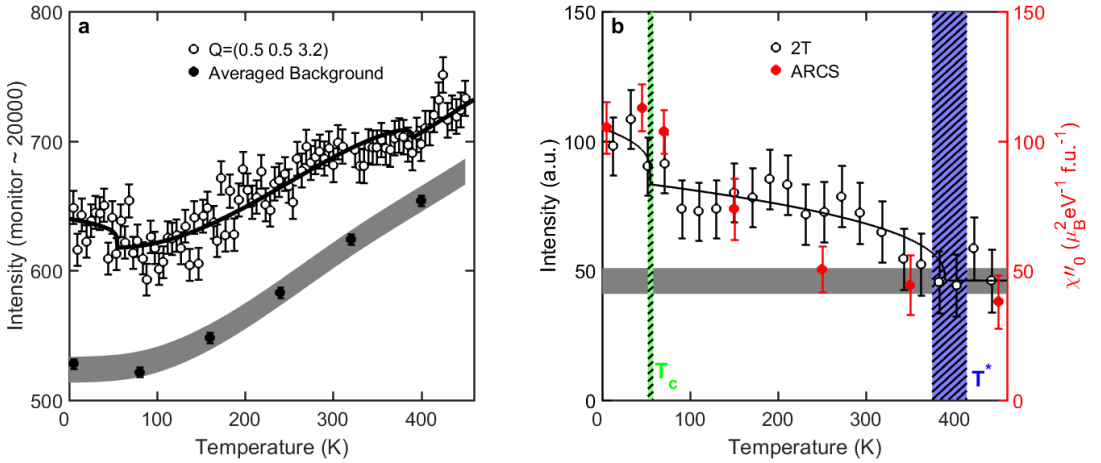

Figure 3.25: *Temperature dependence of the intensity at 30 meV energy transfer. (a) Open circles: intensity at* $\mathbf{Q} = (0.5\ 0.5\ 3.2)$. *Closed circles: background intensity averaged within* $H = 0.3 \pm 0.1$ *r.l.u. (away from* $\mathbf{q}_{AF}$*) from full* $H = 0.2$ - 0.8 *r.l.u. rocking scan. Grey shaded band is the estimated background; the width of the band represents the estimated uncertainty. Data obtained on the 2T triple-axis spectrometer at LLB. (b) Temperature dependence of the magnetic intensity. Red closed circles: time-of-flight neutron data from Figure 3.24, with the averaged range indicated by brown lines and stars in Figure 3.24a . Black open circles: 2T data, extracted by subtracting estimated background from the intensities at* $\mathbf{q}_{AF}$ *(see a). Black solid line: guide to the eyes. Horizontal grey band: uncertainty of the signal baseline due to the uncertainty in background in a; Vertical green and blue bands indicate estimates of* T_c *and* T^**, respectively [13].*

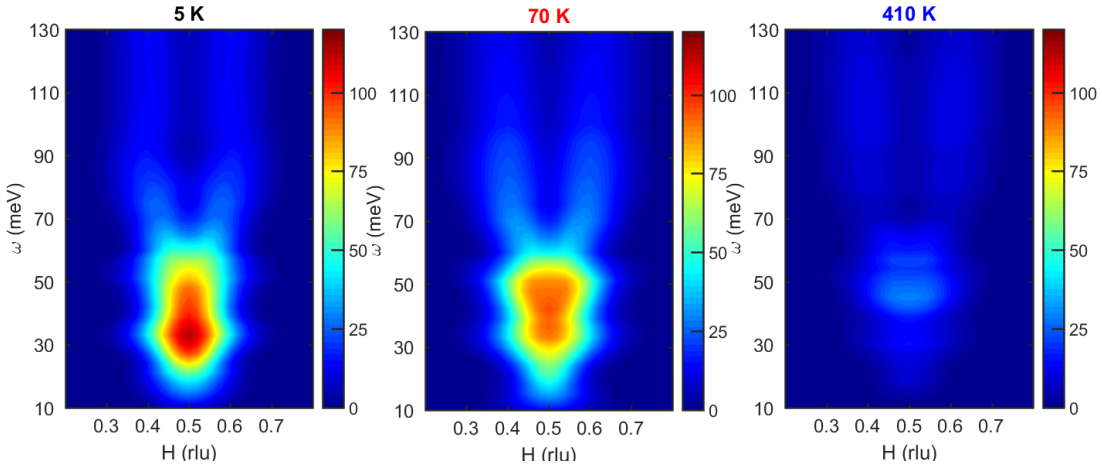

Figure 3.26: *Dispersion of AF response in UD55.* $\chi_0''(H,\omega)$ *contours are determined from 2D Gaussian fit results to data such as those shown in Figures 3.20, 3.21 and 3.22 for (a) 5 K; (b) 70 K and (c) 410 K. The incommensurability* δ *and* 2κ *for the fit to the 410 K data were fixed to be the same as those at 70 K.*

3.2.5 UD45

This sample exhibits similar properties as UD55 and UD71, as seen from Figure 3.27: a wineglass-shaped dispersion with $\Delta_{AF} \approx 6$ meV is observed both below and above T_c. As for the other two samples, the FWHM of the AF response decreases as ω decreases. At $\omega = 9$ meV, it approaches the instrument momentum resolution. Figure 3.28 shows that there is possibly a weak resonance at ~ 21 meV, well below the neck of the dispersion.

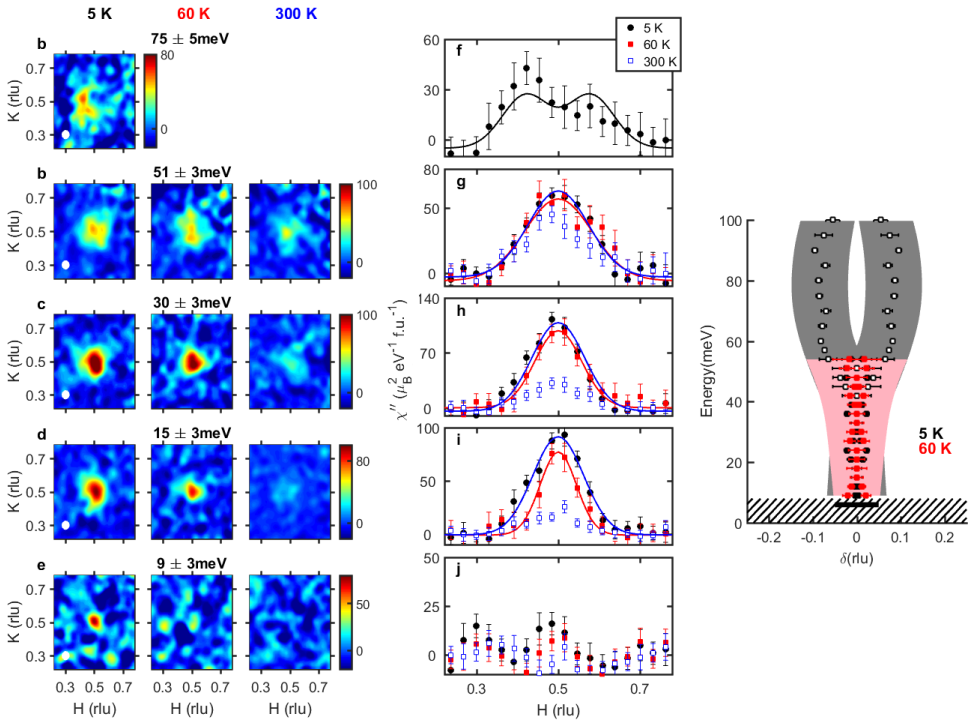

Figure 3.27: *AF response of UD45. This figure is analogous to Figures 3.9, 3.13 and 3.22. (a-f) Constant-energy images of magnetic susceptibility at $T = 5$ K (left), 60 K (middle) and 300 K (right). (g-l) Corresponding constant-ω cuts across $\mathbf{q}_{AF}$, averaged over [1 0] and [0 1] trajectories. Solid lines: Gaussian fits to data convolved with the momentum resolution. (m,n) Energy dependence of incommensurability δ at 5 K (black) and 100 K (red).*

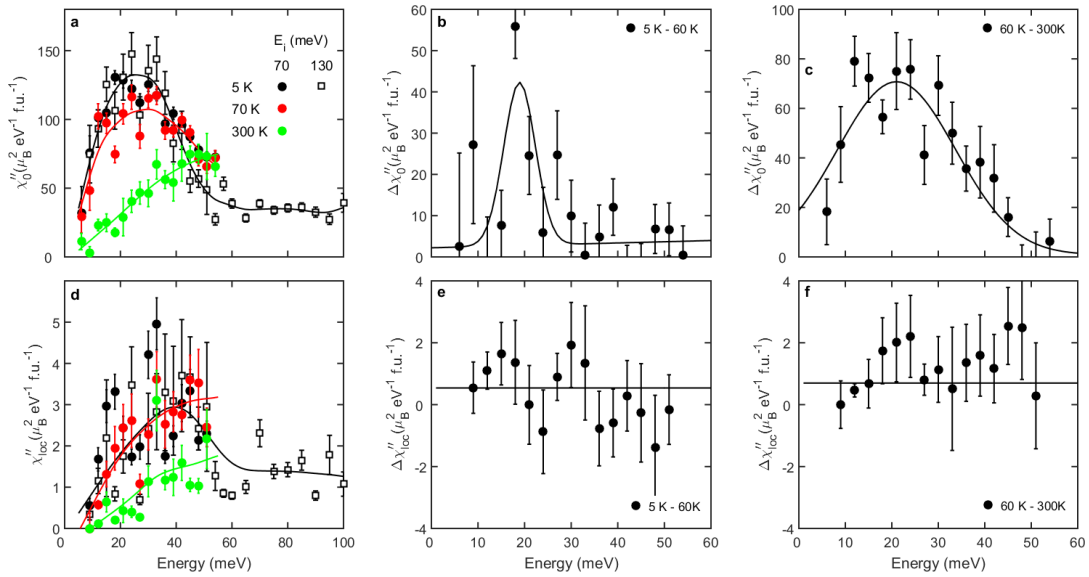

Figure 3.28: *Magnetic susceptibility amplitude and local susceptibility for UD45. This figure is analogous to Figures 3.10, 3.14 and 3.23. (a) Energy dependence of* χ_0''*. Circles:* E_i *= 70 meV. Squares:* E_i *= 130 meV. Solid lines: smooth fits to the data. (b) Difference of* χ_0'' *at 5 K and at 60 K. A weak resonance is seen. Gaussian fit parameters: magnitude =* $39.6 \pm 11.4\ \mu_B^2 eV^{-1} f.u.^{-1}$*, center = 18.9 ± 1.0 meV, FWHM = 8.0 ± 1.6 meV. (c) Difference of* χ_0'' *at 60 K and at 300 K. Solid line is Gaussian fit, with parameters: magnitude =* $69.9 \pm 10.0\ \mu_B^2 eV^{-1} f.u.^{-1}$*, center = 21.0 ± 1.6 meV, FWHM = 30.5 ± 5.8 meV. (d-f) Similar results for the local susceptibility; solid lines indicate the average of data (weighted by error): no peak is observed.*

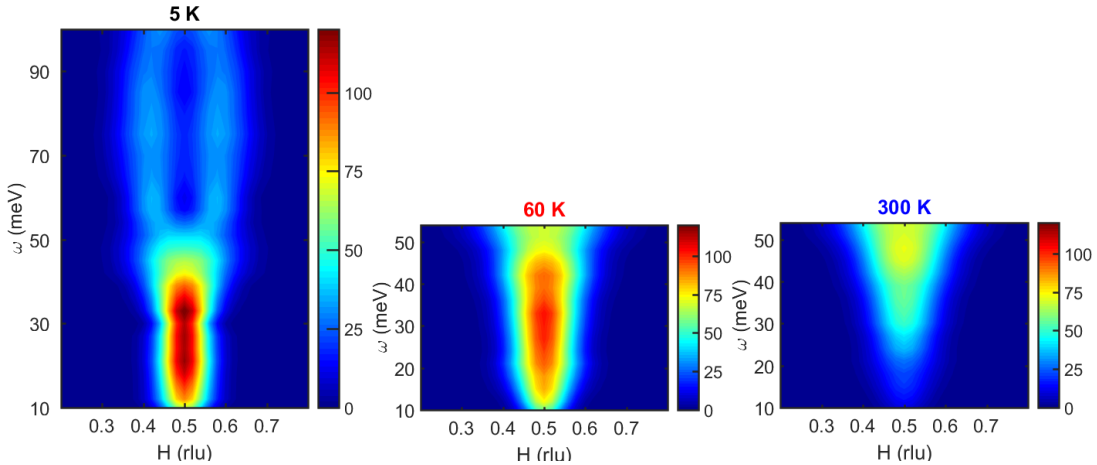

Figure 3.29: *Dispersion of AF response in UD45.* $\chi_0''(H,\omega)$ *contours are determined from 2D Gaussian fit results of energy slices such as those shown in Figure 3.27 for (a) 5 K; (b) 60 K and (c) 300 K. The incommensurability* δ *and FWHM for 300 K data were fixed to be the same as those at 60 K. The data at 60 K and 300 K were collected only with lower incident energy (*E_i *= 70 meV), so only lower energy transfers are shown.*

3.3 Doping Dependence

Close to optimal doping, the AF response of Hg1201 is very similar to moderately underdoped YBCO and can possibly be explained within an itenerant picture [29]. However, as the doping level decreases, the AF response of Hg1201 is distinctly different from prior results for other cuprates. In particular, we observe (1) a wineglass-shaped dispersion both below and above T_c; (2) a very weak or no resonance, with a resonance energy ω_r well below the neck of the wineglass dispersion; (3) a gap Δ_{AF} that does not change across T_c. These results are summarized in Table 3.1 and Figure 3.30. Possible theoretical explanations observed AF response in Hg1201 are briefly discussed in Section 3.4. The gap Δ_{AF} has an almost linear dependence on doping. Since the gap does not change across T_c, it is a signature of the PG state.

Table 3.1: *Summary of AF properties of Hg1201. The shape of dispersion relation is denoted by 'X' for hourglass and 'Y' for wineglass. The gap energy is defined as the energy below which no disernible AF signal is seen; it is the same below and above T_c.*

Sample	Dispersion ($< T_c$)	Dispersion ($>\approx T_c$)	Resonance	Gap energy
UD45	Y	Y	weak	6 meV
UD55	Y	Y	weak	8 meV
UD71	Y	Y	no	27 meV
UD88	X	Y	strong	42 meV

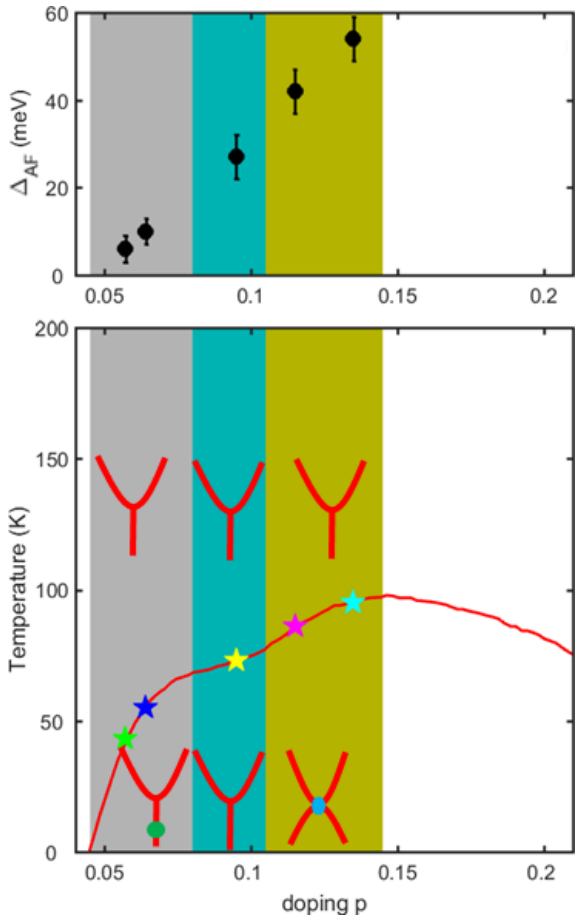

Figure 3.30: *Phase diagram with AF dispersion and gap. Strongly underdoped, moderately-doped, and (nearly) optimally-doped regimes are indicated in grey, turquoise, and olive and correspond to five samples (T_c values marked by stars): UD45, UD55, UD71 and UD88 studied in this Chapter, and a T_c = 95 K sample (OP95, [67]). Measured dispersion (Y- or X-shaped) and resonance (circles) are indicated schematically.*

3.4 Possible Theoretical Explanations

The results summarized in the previous Sections demonstrate that the AF response in Hg1201 is significantly enhanced below the PG temperature T^* and dominated by the PG formation. This suggests that neither the spin-stripe picture nor the itenerant

picture can explain the AF response in Hg1201. As Hg1201 is a model cuprate system [13,15,16,77], the present data can serve as benchmark results for theoretical predictions. Here, we briefly discuss two recent theoretical works, both of which predict a wineglass-shaped dispersion for underdoped cuprates.

Onufrieva [81] starts with a spiral spin state microscopically, and calculates the quantum fluctuations upon doping the AF insulator. The spiral order of localized spins induces an off-diagonal order of mobile charges and a gap Δ which is proportional to the spiral incommensurability wave vector. This gap then produces a feedback to the coherent spin excitation spectrum, resulting in a spin-wave like upper part and a slightly downward dispersed lower part (approximately wineglass-shaped, see Figure 3.31). No prominant effect of superconductivity is found in this calculation. It is also shown that the static spiral state becomes unstable at higher doping, which would explain why UD88 resembles underdoped YBCO and approaches the itenerant picture.

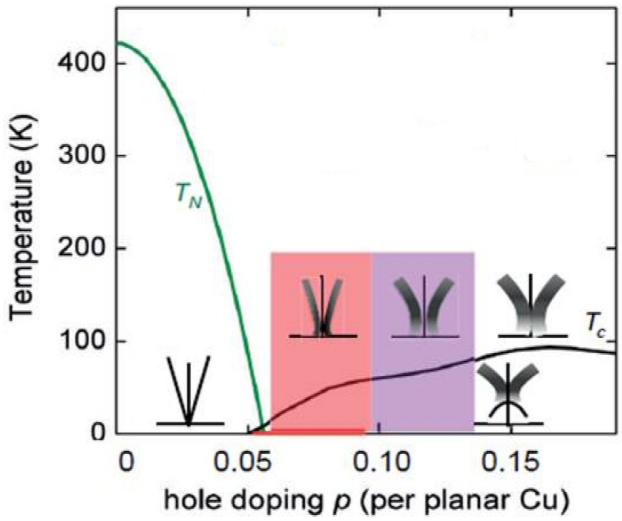

Figure 3.31: *Spiral-spin order simulation of the AF response. Schematic summary of the doping and temperature dependence of spin dynamics across the phase diagram.* T_N *and* T_c *are the AF and SC transition temperatures, the red and purple shaded areas indicate the stability range of static incommensurate uniaxial magnetic order. Inset figures with black lines and shades indicate the simulated dispersion relationships.*

Unpublished work by Gull and Millis starts from the well-known 2D Hubbard model and uses dynamical mean field theory (DMFT) to calculate the spin excitations in cuprates [82]. A comparison of this simulation with the dispersion of UD71 is shown in Figure 3.32. The two agree quite well with each other, although it needs to be noted that the simulation was performed above the PG temperature.

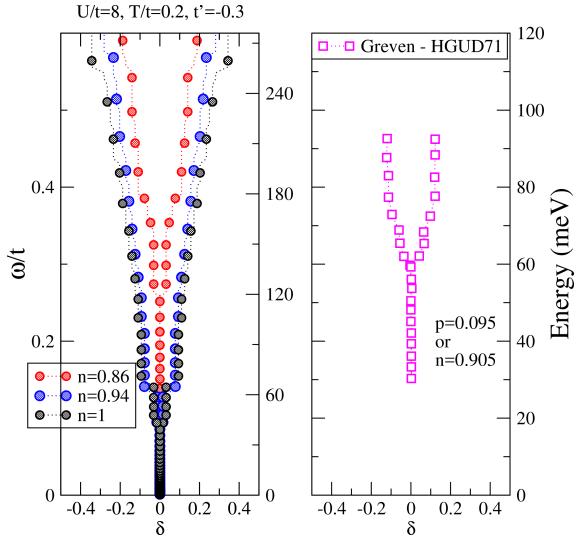

Figure 3.32: *DMFT calculation for the 2D Hubbard Model compared with dispersion relationship of Hg1201. Left: dispersion of AF response calculated for the 2D Hubbard Model at doping levels n = 1 - p = 0.86 (red), 0.94 (blue) and 1 (black), with parameters as indicated. Right: experimental data at 5 K for UD71 (doping level p = 0.905), as discussed in Section 3.2.2.*

Chapter 4

IUC Magnetic Order

Numerous studies indicate that the mysterious PG regime of phase diagram is a distinct phase of matter, including circularly-polarized photoemission [83], polarized-neutron diffraction (PND) [38, 39, 84–91], polar Kerr effect [92], scanning tunnelling microscopy (STM) [93], resonant ultrasound [93], optical birefringence [94], second-harmonic-generation optical response [95], torque magnetometry [96, 97], transport anisotropy in thin films [96], and muon spin relaxation (μSR) [98]. The PND measurements are of particular significance, because they apan a wide range of compounds and doping levels, and reveal unusual magnetic order that preserves the lattice symmetry (referred to as intra-unit-cell (IUC) order, or $\mathbf{q} = 0$ order), which might be the order parameter of the PG phase. In this Chapter, I will first introduce previous PND measurements and several proposed theoretical models. I will then report on our most recent quantitative measurement of the spatial orientation of the IUC magnetic moment, which provides important constraints on the theoretical models.

4.1 Previous Results

The prior PND experiments span four cuprate families - YBCO, Hg1201, LSCO and $Bi_2Sr_2CaCu_2O_{8+\delta}$ (BSCCO) - and point to unusual IUC magnetic order below a doping-dependent characteristic temperature (often denoted T_{mag} or $T_{\mathbf{q}=0}$) that matches the characteristic PG temperature (T^*) determined from planar resistivity measurements. This Section summarizes the results of previous PND experiments.

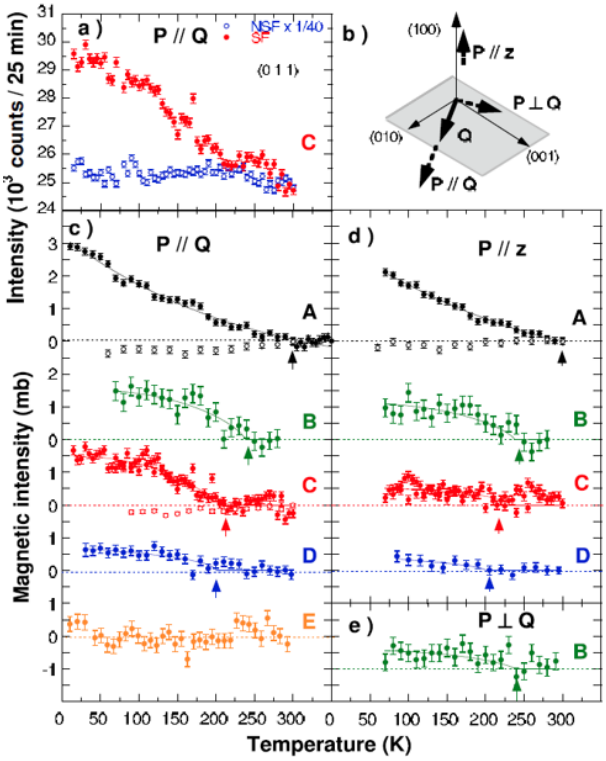

Figure 4.1: *Original PND evidence for IUC magnetic order in YBCO [38]. (a) Temperature dependences of the raw SF and NSF intensity with* $\mathbf{P} \parallel \mathbf{Q}$ *measured at* $\mathbf{Q}$ = *(0, 1, 1) in a sample with* T_c = *64 K. (b) Sketch of the scattering geometry, showing the three polarization directions. (c) Temperature dependences of the extracted magnetic intensity,* I_{mag}*, for* $\mathbf{P} \parallel \mathbf{Q}$ *for four underdoped samples and one overdoped sample (E). (d) Temperature dependences of the magnetic intensity at* $\mathbf{Q}$ = *(0, 1, 1) (solid symbols), as well as* $\mathbf{Q}$ = *(0, 0, 2) (open symbols) for* $\mathbf{P} \parallel \mathbf{z}$*. (e) Temperature dependences of* I_{mag} *at* $\mathbf{Q}$ = *(0, 1, 1) for an underdoped sample with* T_c = *61 K for* $\mathbf{P} \perp \mathbf{Q}$*.*

The first such measurements were performed in YBCO by Fauqué *et al.* [38]. The experiments were carried out on the spin-polarized cold-neutron spectrometer 4F1 at the Laboratoire Léon Brillouin, France. A polarization analysis is necessary for such measurements, since the observed IUC order preserves the translational symmetry of the crystal lattice, and therefore magnetic and nuclear Bragg signals coincide. Quite

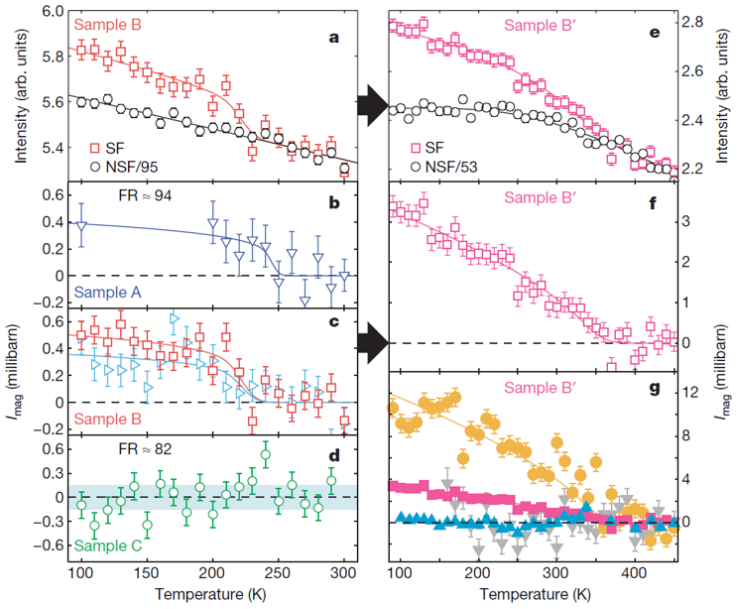

Figure 4.2: *Original PND result for IUC magnetic order in Hg1201, four samples with* T_c *= 61 K (Sample* B′*), 71 K (Sample A), 85 K (Sample B) and 95 K (Sample C) were measured. (a)&(e) Raw data for samples B and* B′*. Magnetic signal appears as additional intensity in the SF channel compared with background intensity due to nuclear Bragg scattering. (b)(d)&(f) Temperature dependence of net intensity* I_{mag}*, which is obtained after the removal of the background, for sample A, B, and C. (g) Intensity measured on different Bragg peaks in the most underdoped sample. Yellow circles, (100); red squares, (101); blue triangles, (201); grey inverted triangles, (102). Data in (a)(f) are collected on the Bragg peak* $\mathbf{Q}$ *= (101), with the neutron spin parallel to* $\mathbf{Q}$*. In (c), data are also collected with the neutron spin perpendicular to Q in the scattering plane (red squares,* $\mathbf{P} \parallel \mathbf{Q}$*; blue triangles,* $\mathbf{P} \perp \mathbf{Q}$*).*

generally, magnetic scattering is weaker than nuclear scattering. Moreover, the magnetic neutron scattering cross section falls off relatively quickly with increasing momentum transfer $|\mathbf{Q}|$, as it is proportional to the square of the magnetic form factor, $|f(\mathbf{Q})|^2$ (see Section 1.2.2). It is therefore important to perform the experiment (i) at relatively weak nuclear Bragg peaks, (ii) at small values of $|\mathbf{Q}|$, and (iii) to minimize leakage of nuclear scattering in the SF geometry, i.e., to achieve as high a flipping ratio (FR) as possible

(see Section 2.2.2). Considering these restrictions, the relatively weak Bragg peak (0, 1, 1) was used in [38], and a rather high FR of ~ 40 was obtained. Figure 4.1 shows the original PND result for the IUC magnetic order in YBCO. Four underdoped samples with $T_c = 54$ K, 61 K, 64 K and 78 K, and one overdoped sample with $T_c = 75$ K were studied. SF and NSF neutron scattering intensities with incident neutron polarization $\mathbf{P}\|\mathbf{Q}$, $\mathbf{P} \perp \mathbf{Q}$, and $\mathbf{P}\|\mathbf{z}$ were measured (see Section 2.2.2 and Figure 4.1b). The FR at room temperature, where no magnetic signal is expected (the pseudogap temperature T^* is below 300 K for all doping levels), was determined and used to rescale the NSF intensities at all temperatures to estimate the non-magnetic background. One can see that the SF intensities systematically deviate from the background below a doping dependent characteristic temperature T_{mag}, and the magnetic signal strength increases as the temperature decreases. No magnetic signal was observed in the overdoped sample. The data were overall found to be consistent with the prior theoretical proposal of loop-current order in the PG state [33]; T_{mag} was found to be consistent with the PG temperature T^* obtained from other experiments.

Nevertheless, the unusual nature of the observed magnetism and the relatively high noise level of the data for YBCO called for a confirmation in another cuprate. This motivated measurements on Hg1201, summarized in Figure 4.2. In the original work on Hg1201 [39], samples with four different doping levels ($T_c = 61$ K, 71 K, 85 K and 95 K) were measured and a very high FR of nearly 100 was achieved. It was shown that the magnetic signal is most significant in underdoped samples and disappeared in the $T_c =$ 95 K sample. These results for Hg1201 are highly consistent with the original findings for YBCO. Subsequent measurements of LSCO [84] and $Bi_2Sr_2CaCu_2O_{8+x}$ (Bi2212) [110] further confirmed the existance of IUC magnetic order in the PG phase.

4.2 Theoretical Models

The IUC magnetic order does not produce a net magnetization and can be naively thought of as a simple superposition of an even number of moments that cancel out within each primitive cell. A state that gives rise to such magnetism was theoretically predicted [33, 34] prior to the experimental findings (Figure 4.3a). In this loop-current (LC) model, spontaneous LCs develop within each square Cu-O plaquette. Orbital

magnetism may arise from either two or four counter-circulating LCs in each plaquette. The PND data are qualitatively consistent with the two-LC scenario, which is also supported by variational Monte Carlo calculations [100]. Whereas in the original model the orbital moments point perpendicular to the CuO_2 planes, the PND data indicate a significant in-plane component, albeit with rather large experimental uncertainty [38,84, 85,88,89]. In a revised version of the original planar LC model, it was argued that such an effective in-plane magnetic signal might originate from a quantum superposition of (classical) LC patterns [101]. Alternatively, the LCs might flow on the faces of the CuO_6 octahedra that surround Cu sites in a single-layer materials such as Hg1201 and LSCO (Figure 4.3b), or on the faces of the CuO_5 pyramids in double-CuO_2-layer compounds such as YBCO and Bi2212. Two distinctly different microscopic pictures involve planar oxygen moments [38] and Dirac (or magneto-electric) multipoles [35–37] (Figure 4.3 c&d, respectively).

Whereas the microscopic nature of the IUC magnetism remains an open question, its existence has been firmly established through PND experiments performed on four different cuprate families. Perhaps the most important theoretical question is the relation between the IUC order and the pseudogap. The original LC model faces a problem: it can explain the IUC order reported by various measurements, but not the opening of the pseudogap, since the order does not break the lattice translational symmetry. However, it has been argued that this may not be a problem if the order is not truly long-range [102]. On the other hand, it has been argued that topological order can open a pseudogap and give rise to an emergent LC phase, with a symmetry consistent with experiment [103]. Furthermore, various models imply charge- or pair-density-wave instabilities, e.g., with a composite d-wave superconducting and charge-density wave with emergent SU(2) symmetry [104,105]. In these models, the pseudogap can be viewed as a phase of fluctuating superconducting correlations, and T^* may be a crossover temperature. However, a preemptive phase that breaks both parity and time-reversal symmetry, such as the original LC phase, is expected at T^* [104]. A very recent proposal [108], which is based on the experimental facts that the pseudogap is spatially inhomogenous [106] and that no large thermodynamic anomaly is observed at T^* [107], argues that the pseudogap formation is a percolative phenomenon associated with gradual, inhomogeneous charge localization of one hole per CuO_2 unit. In this scenario, the IUC

order is an emergent phenomenon that affects the electronic density of states at the Fermi level only gradually upon cooling. The putative percolation transition at T^* is naturally a $\mathbf{q} = 0$ transition. In this model, IUC charge localization (and possibly also magnetic order) starts at higher temperature, prior to subsequent instabilities.

In the next Section, we wish to better characterize the IUC order in the simple-tetragonal model experimental system Hg1201, with particular focus on the question how to describe this state in terms of either LCs or magnetic multipoles.

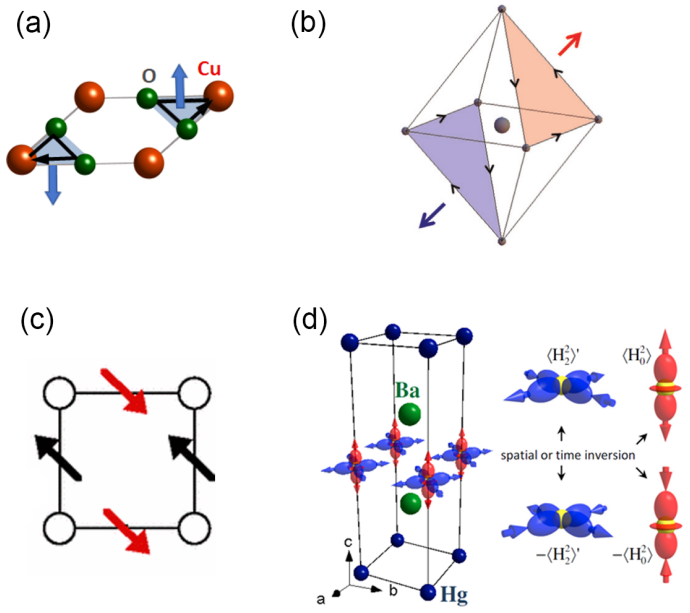

Figure 4.3: *Schematics of four microscopic scenarios of IUC magnetic order. (a) Original in-plane LC model [33, 34]. (b) Revised LC model with charge currents along the surface of CuO_6 octahedra [109]. (c) Schematic microscopic picture that involves planar oxygen moments [38]. (d) Schematic microscopic picture that involves Dirac (or magneto-electric) multipoles [36, 37].*

4.3 Orientation of the Magnetic Moment

4.3.1 Experiment Configuration

In order to help distinguish among the theoretical scenarios described in previous Section, it is important to experimentally determine the orientation of the IUC moments with high precision. This would be best achieved in a structurally simple cuprate compound. Hg1201 is the ideal system for this measurement due to its simple tetragonal crystal structure. From previous work on Hg1201 [39, 86], we already know that the IUC order is strong in underdoped samples, and very small or absent in optimally-doped samples. Therefore, two samples with $T_c = 71$ K and 95 K (denoted UD71 and OP95) are used, the latter, nearly-optimally-doped sample as a reference for background correction. The doping levels of the two samples can be discerned from in the phase diagram shown in Figure 4.4(a). Unlike the previous PND studies of Hg1201, which focused on (1 0 L) reflections with nonzero integer L, we choose the high-symmetry reflection (1 0 0) in this work, as this enables improved polarization analysis. In particular, any wave vector $\mathbf{Q} = (H\ K\ L)$ with nonzero out-of-plane component L results in the measurement of a complex superposition of in-plane and out-of-plane magnetic moments, rendering them difficult to distinguish in the polarization analysis. Moreover, (H 0 0)-type reflections have a unit-cell structure factor for magnetic neutron diffraction that is identically zero for axial dipoles and uniquely sensitive to Dirac multipoles [37].

Most of the spin-polarized neutron diffraction experiments were performed on the cold neutron multi-detector diffractometer D7 at the Institute Laue-Langevin, Grenoble, France, which has a slightly different incident neutron polarization coordinate system than the **xyz** basis used for the previous measurements (see Section 2.2.2 for details). The relavent **XYZ** coordinate system is dipicted in Figure 4.4(c). The experimental set-up was similar to that of a previous study of $YBa_2Cu_3O_{6+x}$ on D7 [89]. Genuine magnetic scattering can be obtained through LPA. In order to minimize neutron absorption of Hg, the incident neutron beam was monochromated to a relatively long wavelength (incident neutron energy of $E_i = 20$ meV, incident wavelength 3.1 Å, or wave vector ≈ 2.02 Å^{-1}).

Additional measurements were performed on the triple-axis spectrometer 4F1 at LLB. This instrument was used in most of the measurements introduced in Section 4.1.

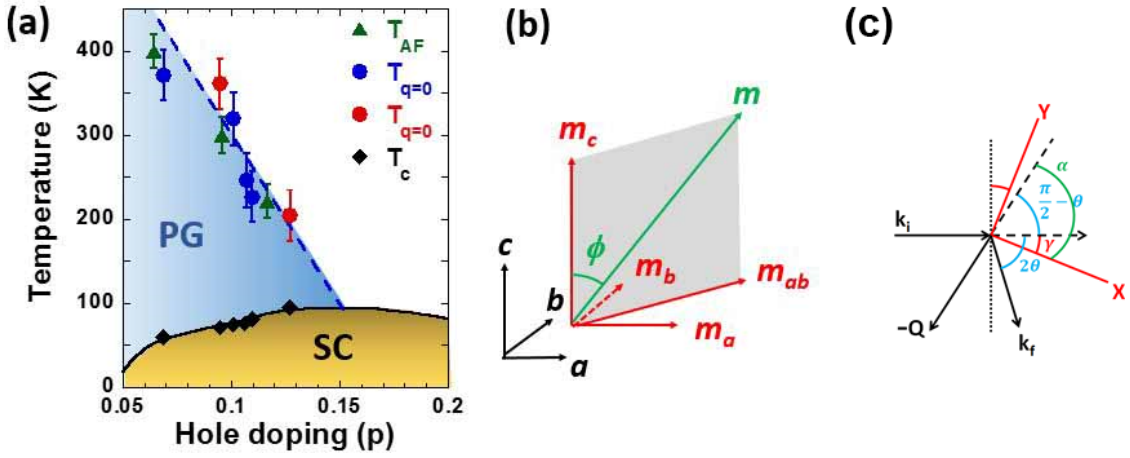

Figure 4.4: *Hg1201 Phase diagram and coordinate system for the D7 experiment. (a) Phase diagram of Hg1201. Red symbols pertain to the samples studied with PND in this Chapter. The superconducting (SC) phase is shown in yellow. The hole doping level (p) is determined from the $T_c\,(p)$ relationship according to [55]. Neutron scattering experiments reveal two characteristic temperatures associated with the pseudogap (PG) phase (light blue area): $T_{q=0}$ and the enhancement of the antiferromagnetic fluctuations at T_{AF} (see Chapter 3). These temperatures are consistent with the characteristic pseudogap temperature T^* obtained from charge transport measurements [13]. (b) Definition of magnetic moment components along different crystal lattice directions relevant to the D7 experiment; ϕ is defined as the angle between the c-axis and the total magnetic moment ($\mathbf{m}$). (c) Schematic of scattering plane, defined by the incident ($\mathbf{k_i}$) and scattered ($\mathbf{k_f}$) neutron wave vectors, along with the definition of the polarization directions $\mathbf{X}$ and $\mathbf{Y}$ ($\mathbf{Z}$ is perpendicular to the scattering plane). The angle $\gamma = 41.6^{\circ}$ is the default configuration on the D7 spectrometer at the ILL, 2θ is the scattering angle, and α is defined as the acute angle between the momentum transfer $\mathbf{Q} = \mathbf{k_i} - \mathbf{k_f}$ and the polarization direction $\mathbf{X}$.*

An incident wave vector $\mathbf{k}_i = 2.57$ Å^{-1} (E_i=13.7 meV) was chosen and higher-harmonic neutrons were removed by a pyrolithic graphite filter placed before the polarizing supermirror. The final neutron energy and polarization were analysed with a Heusler crystal.

As discussed extensively [91], the main difficulty is such an experiment is the determination of the temperature dependence of the bare flipping ratio FR. FR is primarily a function of the sample environment and instrument, but also of the sample itself (shape, mosaicity). Due to imperfections in the neutron optics, the polarization is somewhat spatially inhomegenous. Therefore, FR inevitably evolves with temperature, because the sample is slightly displaced within the polarized beam when the temperature is changed. In practice, FR is determined at a Bragg reflection where no magnetic signal is expected. On a triple-axis spectrometer, this can be achieved with the same neutron path (analyzser/detector) after the sample by moving the analyzer arm to Bragg positions where no magnetic signal is expected and/or seen in previous studies. This is generally not always possible on D7 due to geometrical constraints, and because each scattering angle is typically associated with a specific bender/detector. Therefore, although the statistical error is smaller on D7, the triple-axis instrument allows a better determination of thermal drift of FR, limiting systematic errors on the magnetic intensity. In summary, the two rather distinct instruments D7 and 4F1 have different types of limiting factors. On D7, it is the inability to accurately determine the baseline of the inverse of the flipping ratio (1/FR), which inevitably drifts with temperature, and thus causes a systematic error. This precluded an accurate determination of the magnetic intensity in OP95. However, as we will show, the OP95 data serve as an excellent reference for the underdoped UD71 sample. The statistical errors are smaller on D7 than on 4F1, which leads to a better accuracy in the determination of the tilt angle.

4.3.2 Polarization Analysis Methods

We define $\mathbf{m}$ to be the total magnetic moment of the system, $\mathbf{m_{a,b,c}}$ the moment projections onto the three unit cell axes a, b and c, and $\mathbf{M_{X,Y,Z}}$ the magnetic signals probed with neutron-spin polarization directions along the XYZ directions, as shown in Figure 4.4(c). Note that Hg1201 has tetragonal symmetry. Therefore, its a and b axes are equivalent, and we can write $\mathbf{m_{ab}}^2 = 2\mathbf{m_a}^2 = 2\mathbf{m_b}^2$ (see Figure 4.4(b)). Then, with

the high-symmetery reflection wave vector $\mathbf{Q} = (1\ 0\ 0)$, we have:

$$\begin{aligned} \mathbf{M_Z} &\propto \mathbf{m_c}^2, \\ \mathbf{M_Y} &\propto \frac{1}{2}\mathbf{m_{ab}}^2 + \sin^2\alpha\ \mathbf{m_c}^2, \\ \mathbf{M_X} &\propto \frac{1}{2}\mathbf{m_{ab}}^2 + \cos^2\alpha\ \mathbf{m_c}^2, \end{aligned} \tag{4.1}$$

where α is the angle between the momentum transfer $\mathbf{Q}$ and the polarization direction $\mathbf{X}$ (see Figure 4.4(c)). For $\alpha = 0$, the magnetic intensity follows the sum-rule $\mathbf{M_X} = \mathbf{M_Y} + \mathbf{M_Z}$ discussed in previous reports using LPA on triple-axis spectrometers. On the diffractometer D7, $\alpha = 108.2^o \pm 5^o$ for $\mathbf{Q} = (1\ 0\ 0)$.

The prior PND work revealed an order-parameter-like temperature dependence [39, 86] for the magnetic moment, and we can therefore write:

$$\begin{aligned} \mathbf{m_{a,b,c}}(T) &= \mathbf{m_{a,b,c}}\left(1 - \frac{T}{T_{\mathbf{q}=0}}\right)^{\beta}, \quad if\ T < T_{\mathbf{q}=0} \\ &= 0, \quad otherwise, \end{aligned} \tag{4.2}$$

where $T_{q=0}$ is the onset of the IUC order (also written as T_{mag} in previous work), $\mathbf{m_{a,b,c}}$ are zero-tempearture magnetic moments, and β is the effective exponent that describes the observed power-law-like temperature dependence.

In order to extract $\mathbf{m_{a,b,c}}$ from measured neutron scattering intensity in the SF channel, $I^{SF}_{X,Y,Z}(T)$, and NSF channel, $I^{NSF}_{X,Y,Z}(T)$, several factors need to be taken into account. First, a thermal envelope function $f(T)$ is included for both SF and NSF data. This function captures contributions to the measured intensity due to thermal effects, such as the relative motion of the sample with regard to the incident beam (and hence the projection of the scattered beam onto the detector) due to thermal contraction/expansion of the sample stick, as well as the Debye-Waller factor. Also, the thermal dependence of the lattice parameters is not fully captured by the momentum resolution at all temperatures. With these combined thermal effects captured by the envelope function, the corrected NSF intensity then becomes independent of temperature and equal to the intrinsic value $I^{NSF}_{X,Y,Z}(T = 0)$ given by Bragg scattering at $T = 0$, whereas

the SF intensity contains a background term as well as magnetic signal:

$$\begin{aligned} I^{NSF}_{X,Y,Z}(T) &= I^{NSF}_{X,Y,Z}(T=0)\, f(T)\,, \\ I^{SF}_{X,Y,Z}(T) &= [BG^{SF}_{X,Y,Z} + M_{X,Y,Z}(T)] f(T)\,. \end{aligned} \tag{4.3}$$

Second, we assume that $BG^{SF}_{X,Y,Z}$ is purely due to leakage of NSF scattering into the SF channel, which can be estimated from the temperature dependent $FR(T) = FR(T=0)\, g(T)$:

$$BG^{SF}_{X,Y,Z} = \frac{I^{NSF}_{X,Y,Z}(T=0)}{FR_{X,Y,Z}(T)} = \frac{I^{NSF}_{X,Y,Z}(T=0)}{FR_{X,Y,Z}(T=0)} g(T)\,. \tag{4.4}$$

We note that this analysis constitutes an improvement over the early work [38, 39], in which FR was taken to be independent of temperature. Moreover, although both thermal factors originate from imperfections of the experiment, we note that $g(T)$ is different from $f(T)$ in the sense that the former arises during the spin-polarization and detection process, whereas the latter results from the thermal variation of both instrument position and sample lattice parameters. Putting everything together, and inserting the value of α, we get the full expressions for the SF intensities:

$$\begin{aligned} \frac{I^{SF}_X(T)}{f(T)} &= \frac{I^{NSF}_X(T=0)}{FR_X(T=0)} g(T) + \left(\frac{1}{2}\mathbf{m_{ab}}^2 + 0.0976\mathbf{m_c}^2\right)\left(1-\frac{T}{T_{q=0}}\right)^{\beta}, \\ \frac{I^{SF}_Y(T)}{f(T)} &= \frac{I^{NSF}_Y(T=0)}{FR_Y(T=0)} g(T) + \left(\frac{1}{2}\mathbf{m_{ab}}^2 + 0.9024\mathbf{m_c}^2\right)\left(1-\frac{T}{T_{q=0}}\right)^{\beta}, \\ \frac{I^{SF}_Z(T)}{f(T)} &= \frac{I^{NSF}_Z(T=0)}{FR_Z(T=0)} g(T) + \mathbf{m_c}^2\left(1-\frac{T}{T_{q=0}}\right)^{\beta}. \end{aligned} \tag{4.5}$$

Finally, two distinct methods are actually used to estimate $g(T)$ and to analyze the scaled SF data:

1. Method 1 is a blind test, which assumes that both UD71 and OP95 exhibit the same linear SF background temperature dependence: $g_{UD71}(T) = g_{OP95}(T)$. An IUC magnetic signal is allowed in this analysis for both samples, i.e., $g(T) = 1 + \eta T$ (assuming linear T-dependence) is inserted into Equation 4.5 in both cases.

2. Method 2 assumes that OP95 exhibits no magnetic Bragg signal (or that the ordered moment is immeasurably small), consistent with prior work [86]. We then use the OP95 data as background to analyze the UD71 result at the same (1 0 0) Bragg peak, i.e., $g_{OP95}(T)$ is first estimated using $I^{SF}_{OP95}(T)$, and then inserted into Equation 4.5 for UD71.

4.3.3 Results and Discussion

Figure 4.5 shows the inverse flipping ratio, 1/FR, which equals I_{SF}/I_{NSF}, for both UD71 and OP95 for the three principle neutron-spin polarization geometries. An enhancement of 1/FR below about 360 K is seen in UD71, whereas there is no effect for OP95, as expected. At a qualitative level, this confirms the existence of IUC magnetism in underdoped Hg1201.

In order to confirm that OP95 indeed exhibits no IUC order, and to test the assumption made for Method 2, the blind test Method 1 is performed. Figure 4.6 shows SF channel data for UD71, OP95, and graphite, after scaling the data with the envolope function $f(T)$ obtained from the NSF response (see Equation 4.3); solid lines are fit results using linear background function for Equation 4.5. It is clear that graphite, UD71 at $\mathbf{Q}$ = (0 0 3), and OP95 at $\mathbf{Q}$ = (1 0 0) show no magnetic signal. This is expected, since graphite is a non-magnetic material, and previous measurements [39,86] showed that the IUC magnetic response is very weak at large out-of-plane momentum transfers and near optimal doping. On the other hand, UD71 at $\mathbf{Q}$ = (1 0 0) shows clear excess intensity on top of a background with the same slope as for OP95 at $\mathbf{Q}$ = (1 0 0). Moreover, the magnetic signal is strongest in the $\mathbf{Y}$-polarization channel, consistent with Equation 4.1. The values of $\mathbf{m_{ab}}$ and $\mathbf{m_c}$, estimated from fits to Equation 4.5, are shown in Table 4.1.

Following these preliminary tests, Method 2 is applied. Figure 4.7 shows the remaining SF intensities for UD71 after removing background intensity obtained from the OP95 data. These processed data contain only pure magnetic scattering intensities. $T_{q=0} \approx 360$ K and $\beta \approx 0.20 \pm 0.05$ are obtained upon fitting the data with Equation 4.5, and the fitted values for $\mathbf{m_{ab}}$ and $\mathbf{m_c}$ are shown in Tabel 4.1.

Recent μSR measurements of YBCO [98] and Bi2212 [99] revealed slow magnetic fluctuations and critical slowing down in the pseudogap phase. In particular, the μSR

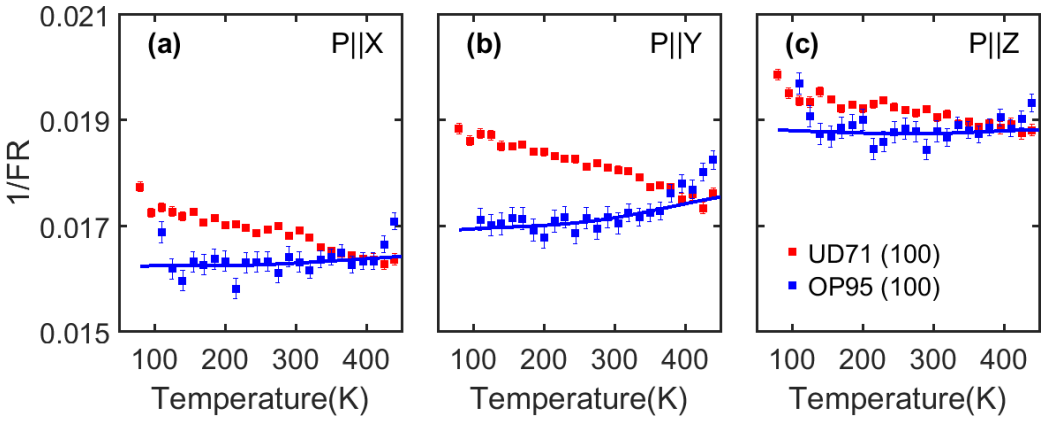

Figure 4.5: *Temperature dependence of 1/FR for UD71 and OP95. (a)-(c) Temperature dependence of the inverse flipping ratio (1/FR) at the (1 0 0) reflection for the three principal incident neutron-spin polarization directions for UD71 (red) and OP95 (blue). A magnetic signal is evident in UD71 from the upturn below* $T_{q=0}$ *= 360 - 380 K. For better visualization, the OP95 results are shifted by about -0.004 (X) -0.005 (Y) and -0.003 (Z) to best match the average of the UD71 data at high temperature between 360 and 400 K. Solid blue lines are smooth polynomial fits to the OP95 data, with less weight given to the high-temperature data (≥ 400 K), where in this particular measurement the uncertainty in the flipping ratio increases due to larger thermal effects and hence the data are less reliable. The error bars indicate a statistical (counting) uncertainty and do not reflect this additional systematic uncertainty.*

longitudinal relaxation rate was found to go through a maximum at the temperature $T_{\mathbf{q}=0}$ (or T_{mag}), a characteristic of critical slowing down typically associated with a second-order phase transition. In a PND study of nearly-optimally-doped $YBCO_{6.85}$ [89], which was also performed on the D7 diffractometer, evidence for critical-like magnetic scattering was reported at $\mathbf{Q}$ = (0.88 0 0), i.e., off the Bragg position (see Figure 4.8b). In Figure 4.8a, we test this observation in Hg1201, by plotting the sum of all SF cross-sections, $\Sigma_{SF} = I^X_{SF} + I^Y_{SF} + I^Z_{SF}$, off the Bragg peak at $\mathbf{Q}$ = (0.88 0 -0.11). For both UD71 and OP95, Σ_{SF} displays a peak at a temperature close to the pseudogap temperature T^*, suggestive of magnetic critical slowing down. For UD71, the characteristic temperature of the maximum of Σ_{SF} is consistent with the ordering

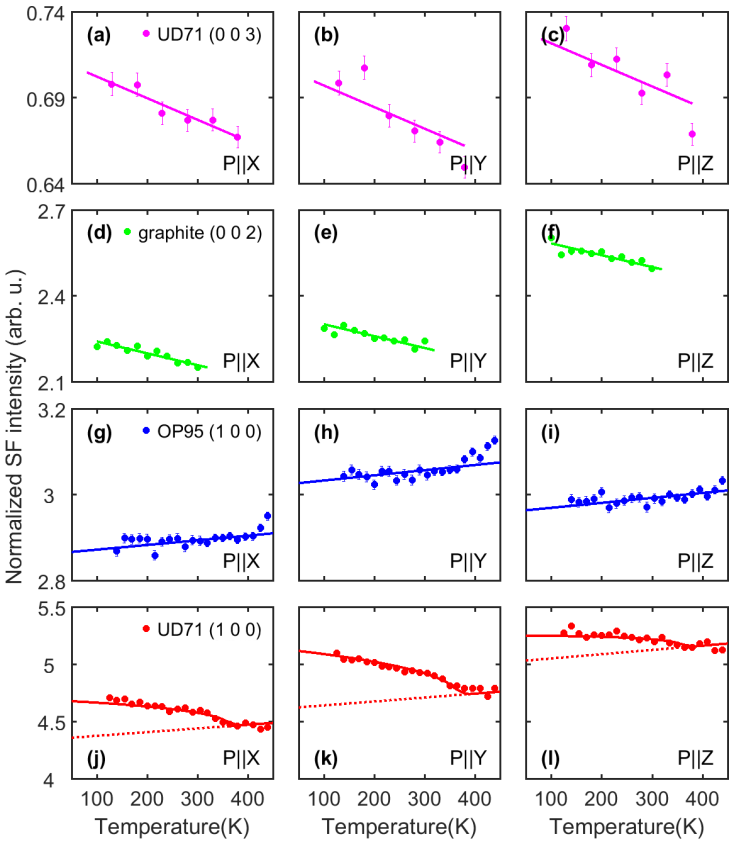

Figure 4.6: *Comparison of SF intensities for UD71, OP91 and graphite - analysis Method 1. Rows from top to bottom: UD71 at (0 0 3), graphite at (0 0 2), OP95 at (1 0 0) and UD71 at (1 0 0). Columns from left to right: incident neutron-spin polarization parallel to X, Y and Z directions (see Figure 4.4c). Solid lines for UD71 at (0 0 3) and graphite are linear fits. Solid lines for OP95 and UD71 at (1 0 0) are the fits using method 1 (blind test). The red dashed lines show the linear background for the fits, which is assumed to be the same for UD71 and OP95.*

temperature obtained at the Bragg position (1 0 0) (Figure 4.7). For OP95, one can define the temperature $T_{\mathbf{q}=0} \approx 200$ K from the enhancement in Figure 4.8a.

In light of the observation for nearly optimally-doped $YBCO_{6.85}$ of short-range rather than long-range magnetic order [90], we propose that the IUC magnetism in OP95 is short-range as well. As a consequence, the magnetic response is redistributed throughout

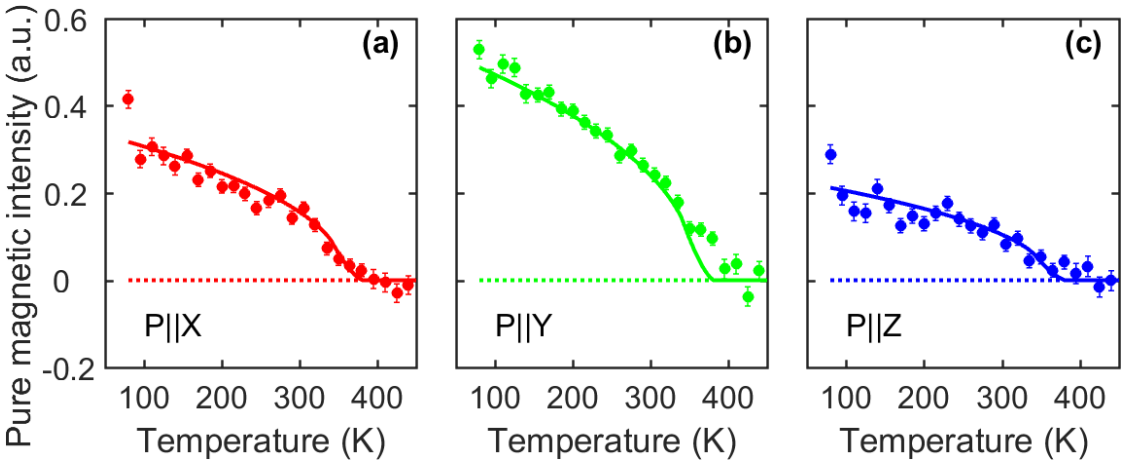

Figure 4.7: *Results for UD71 - analysis Method 2. (a)-(c) Temperature dependence of the (1 0 0) magnetic signal for UD71 for the three principal incident neutron-spin polarization directions. The signal is extracted according to Method 2 (see Section 4.3.2), which simply assumes that no discernible magnetic Bragg signal exists in OP95. The results of fits to Equation 4.5 are shown as solid lines.*

the Brillouin zone and not discernible at $\mathbf{Q} = (1\ 0\ 0)$ with the signal-to-noise ratio on the D7 instrument. In contrast, a complementary measurement of OP95 across the (1 0 0) and (1 0 1) reflections on the triple-axis spectrometer 4F1 at LLB revealed evidence for critical magnetic scattering (see Figure 4.8c). These observations motivated us to search for a weak magnetic signal away from the (1 0 0) Bragg position. Figure 4.8d shows the momentum scans at $\mathbf{Q} = (H\ 0\ -0.4)$ in the SF channel across $H = 1$, obtained at 150 K (below $T_{\mathbf{q}=0}$) and 225 K (above $T_{\mathbf{q}=0}$). Indeed, we are able to discern a net magnetic signal at $H = 1$, consistent with the existence of short-range IUC magnetic order in OP95 (see Figure 4.8e). A rough estimate of the in-plane correlation length yields $\xi \approx 5a$ (where $a = 3.89\,\text{Å}$ is the crystal lattic constant), a value that is even shorter than for YBCO6.85 [90].

We have demonstrated that the observation of a magnetic Bragg signal in the pseudogap state of UD71 is independent of the data analysis method and consistent with a second-order phase transition at $T_{q=0} = 360 \pm 30$ K, accompanied by magnetic critical fluctuations. The current results for Hg1201, obtained on a diffractometer (D7) with

Table 4.1: *Data analysis results for the IUC magnetic moment for UD71 and OP95, obtained from measurements at the (1 0 0) reflection. The same arbitrary units are used for both samples and methods. ϕ is defined as the angle between the total magnetic moment and the crystalligraphic c-axis.*

Fitting Data/Method	$\mathbf{m_c^2}$ (a.u.)	$\mathbf{m_{ab}^2}$ (a.u.)	$\phi = \arctan\left(\frac{\mathbf{m_{ab}}}{\mathbf{m_c}}\right)$
UD71/Method 1	0.20 ± 0.06	0.58 ± 0.14	71° ± 10°
UD71/Method 2	0.24 ± 0.09	0.68 ± 0.16	69° ± 10°
OP95/Method 1	0.06 ± 0.08	0.04 ± 0.04	-

unprecedented signal-to-noise ratio, confirm and go beyond prior work, which employed a triple-axis spectrometer. For OP95, no magnetic Bragg signal is discernible within error, i.e., it is at least one order of magnitude weaker than for UD71 (see Table 4.1).

For UD71, quantitative longitudinal polarisation analysis yields in-plane and out-of-plane magnetic components with unprecedented accuracy. The moment direction is tilted away from the crystallographic c axis by $\phi = 70° \pm 10°$. This value is somewhat larger, yet consistent with those obtained for other cuprates (Table 4.2). Our results (Table 4.1) allow us to rule out models with strictly in-plane ($\phi = 90°$) or out-of-plane ($\phi = 0$) magnetic moments. Specifically, we can rule out all models where ϕ goes to 0 at $L = 0$, in particular the original planar LC model [33, 34], and models where ϕ goes to 90° at $L = 0$, in particular the magneto-electric multipole scenarios with quadratic symmetry in which the out-of-plane moment component is zero [35–37]. However, we cannot rule out variations of these scenarios, either within the LC picture, where an in-plane component might appear due to quantum corrections [101], or quadrupolar order with low, monoclinic symmetry [35, 37]. One can understand the physical meaning of these pictures upon considering that the size of the quadrupolar lobe or the loop current is similar to the neutron wavelength. Within a primitive cell, each quadrupolar lobe (or loop current) exhibits different spontaneous magnetic fields on opposite sides of the Cu atom (see Figure 4.3). The neutron spin moment probes these different microscopic magnetic patterns (and interference between them). An interesting scenario to explain

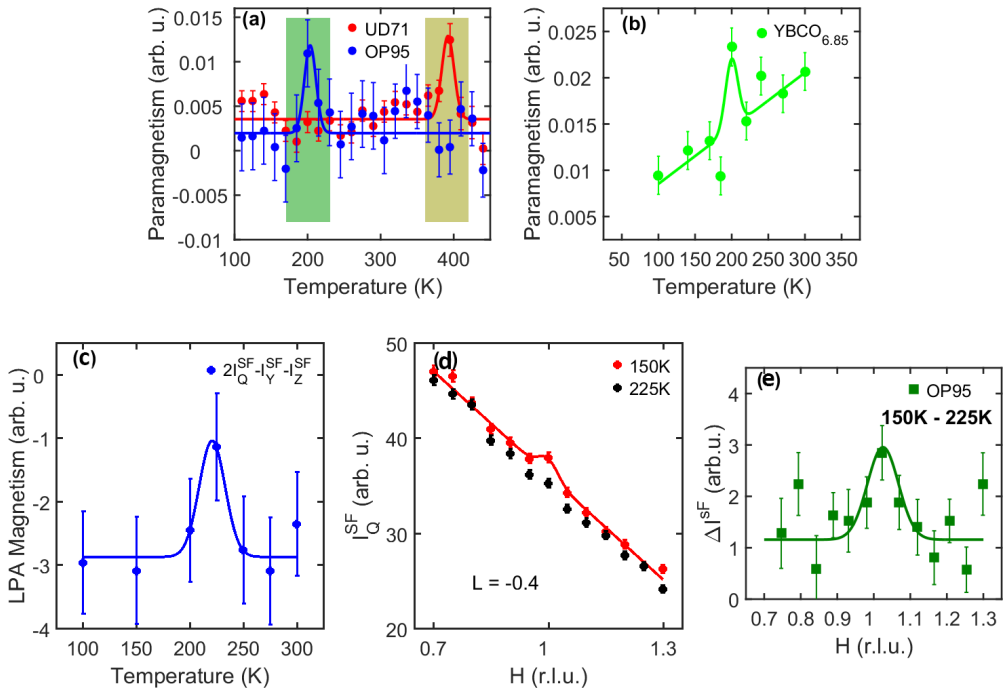

Figure 4.8: *Magnetic critical scattering for UD71 and OP95. (a) Temperature dependence of* $\Sigma_{SF} = I^X_{SF} + I^Y_{SF} + I^Z_{SF}$ *for both UD71 (red) and OP95 (blue). Data are average of 11 points which are centered at momentum transfer* $\mathbf{Q}$ *= (0.88 0 -0.11) for better counting statistics. The peaks at about 370 K for UD71 and about 200 K for OP95, as highlighted by the yellow and green shaded areas, indicate the appearance of a magnetic signal away from the Bragg peak at a temperature consistent with the pseudogap temperature* T^* *obtained from transport measurements (see Figure 4.4). (b) Temperature dependence of* Σ_{SF} *for* $YBCO_{6.85}$ *measured with the same spectrometer with similar analysis method (from [90]); the data show a peak at* T^* *as well. (c) Temperature dependence of LPA of pure magnetic signal measured on spectrometer 4F1 at LLB for the same OP95 sample used on D7, at a momentum transfer* $\mathbf{Q}$ *= (0.9 0 0), off the Bragg peak. (d) Momentum scan across (1 0 -0.4) with incident neutron spin polarized along the momentum transfer* $\mathbf{Q}$ *(*$\mathbf{P} \parallel \mathbf{Q}$*). Red and black symbols: 150 K and 225 K, respectively. (e) Temperature difference of data in d.*

Table 4.2: *Summary of previous estimates of the tilt angle of the magnetic moment for various underdoped cuprates based on measurements at* $\mathbf{Q}$ *= (1 0 L) [38,84,88–91]. The estimated tilt angles fall into the 45 ± 20° range.*

Compound	Sample T_c	Estimated tilt angle	L
$YBa_2Cu_3O_{6.6}$	61 K	35 ± 7°, 55 ± 7°	0, 1
$YBa_2Cu_3O_{6+x}$	54 K, 61 K, 64 K	45 ± 20°	1
$YBa_2Cu_3O_{6.85}$	89 K	40 ± 9°	0.25
$La_{1.915}Sr_{0.085}CuO_4$	22 K	∼ 45°	0
$HgBa_2CuO_{4+\delta}$	75 K	45 ± 25°	1
$Bi_2Sr_2CaCu_2O_{8+\delta}$	85 K	20 ± 20°	3

the data is actually the dual existence of planar LC and magneto-electric quadrupole, as both can be treated on the same ground [111].

Our result also is consistent with a variant of the LC model in which charge currents flow on the faces of the oxygen pyramids/octahedra (Figure 4.3). For Hg1201, this corresponds to an angle of about 64°, as calculated from lattice parameters [39]. Several variants of this scenario have been considered [39, 112–114]. However, most of these variants are inconsistent with our data at the high symmetry point, $L = 0$. Indeed, structure factor calculations show that the variants considered in [39, 112, 113] exhibit out-of-plane and in-plane components at different Bragg positions: only the out-of-plane component contributes to the (1 0 0) reflection, whereas the in-plane component would result in intensity at (0 0 L) Bragg peaks, which has not been observed in experiment. Only the specific variant with two current loops depicted in Figure 4.3 (originally considered in [109]) is consistent both with the neutron and Kerr-effect data [92, 114]; in this scenario, the currents avoid the Cu atoms and flow on opposite faces of the two pyramids that form the CuO_6 octahedra of Hg1201.

YBCO features pairs of CuO_5 pyramids associated with adjacent CuO_2 planes rather than CuO_6 octahedra associated with a single plane. The faces of the pyramids form an angle of about 59° [39] with the CuO_2 planes. According to earlier results for (twin free)

underdoped YBCO [91], the out-of-plane magnetic scattering exhibits an a-b anisotropy, which is furthermore L-dependent. This feature can be accounted for by a crisscrossed stacking of planar LCs, and it eliminates as a possible origin of the out-of-plane magnetic scattering all magnetic patterns that do not break parity, such as magnetism on the oxygen sites. Further, the PND data for nearly optimally-doped YBCO show the absence of a tilt ($\phi = 0$) at high temperature, where magnetic correlations develop, and that ϕ acquires a nonzero value of $40 \pm 9^\circ$ at $T_{q=0}$ [89]. This variation of ϕ as a function of temperature is consistent with a crossover from classical to quantum planar LC correlations [101], with the coexistence of planar LC order and another form of $\mathbf{q} = 0$ magnetic order (the latter controlling the in-plane magnetic scattering intensity, e.g., multiple orderes), and with a crossover from planar to out-of-plane LC order. The temperature dependence of ϕ would also explain why the extracted tilt angle can vary with the L index of Bragg peaks (Table 4.2). Because if we assume that the magnetic moment has different in-plane and out-of-plane origins (thus different structural form factor), then either changing temperature (resultingly, changing the lattice constants) or the L value in momentum transfer would change the ratio of the magnitudes of in-plane and out-of-plane moments, thus changing the tilt angle. In the latter two scenarios, the tilt angle reflects the degree of admixture either of different kinds of IUC order, or of planar and out-of-plane currents, which might change not only with temperature, but also with doping. In this regard, it is interesting to note that ϕ is quite large for the underdoped Hg1201 sample, reaching $70 \pm 10^\circ$, whereas, for a nearly optimally-doped Bi2212 the angle was found to be as small as $20 \pm 20^\circ$ below $T_{q=0}$ (Table 4.2).

In conclusion, we have conducted a quantitative polarized-neutron diffraction study of the model cuprate Hg1201. Consistent with prior work, we observe robust IUC magnetic order in the pseudogap state of a moderately-doped sample with $T_c \approx 71$ K, and evidence for short-range correlations in a nearly optimally-doped sample with $T_c \approx 95$ K. In the former case, analysis of the data obtained at the (1 0 0) reflection yields the estimate $\phi = 70^\circ \pm 10^\circ$ for the tilt direction of the magnetic moment away from the c-axis. This estimate constitutes a significant improvement over prior results and places a new constraint on the microscopic origin of the observed IUC magnetism. One possibility is a specific variant of the loop-current scenario in which the currents flow on the faces of the CuO_6 octahedra.

Chapter 5

Ising-like Mode

5.1 Introduction

A dispersionless mode at about 55 meV was first discovered by Yuan Li *et al.* [42]. The discovery was motivated by the prior observation of nominal "background" intensity that decreased with increasing temperature during measurements of the magnetic resonance mode in optimally-doped Hg1201 [67]. Subsequently, a similar mode was observed in the 30 - 40 meV range [43]. Figure 5.1 shows evidence for the magnetic nature of the two excitations in the T_c = 65 K and 95 K Hg1201 samples (denoted UD65 and OP95). In both cases, the onset temperature was found to match the PG temperature T^*. Figure 5.2 shows that the energy of these modes does not exhibit strong momentum dependence, i.e., the energy-momentum dispersion relationship is almost flat throughout the Brillouin zone. Moreover, their intensities follow distinct momentum dependences, indicative of different structure factors and possibly different microscopic origins. The high-energy mode is strongest at large L values and small H and K values (i.e., when $\mathbf{Q}$ is mostly out of the CuO_2 plane). On the other hand, the low-energy mode is strongest at small L values and large H and K values ($\mathbf{Q}$ is mostly within the CuO_2 plane). The statistical physics of the loop-current (LC) model by Varma is that of the Ising-like Ashkin-Teller model and, as a result, two dispersionless modes are expected [40,41,115]. We therefore refer to the dispersionless excitations as Ising-like modes, or flat modes.

The previous measurements, although detailed and elegant, were not complete. This Chapter focuses on the systematic neutron scattering study of the high-energy Ising-like

mode, including its doping- and momentum-dependence, and an initial effort to see an $^{16}O \rightarrow {}^{18}O$ isotope exchange effect.

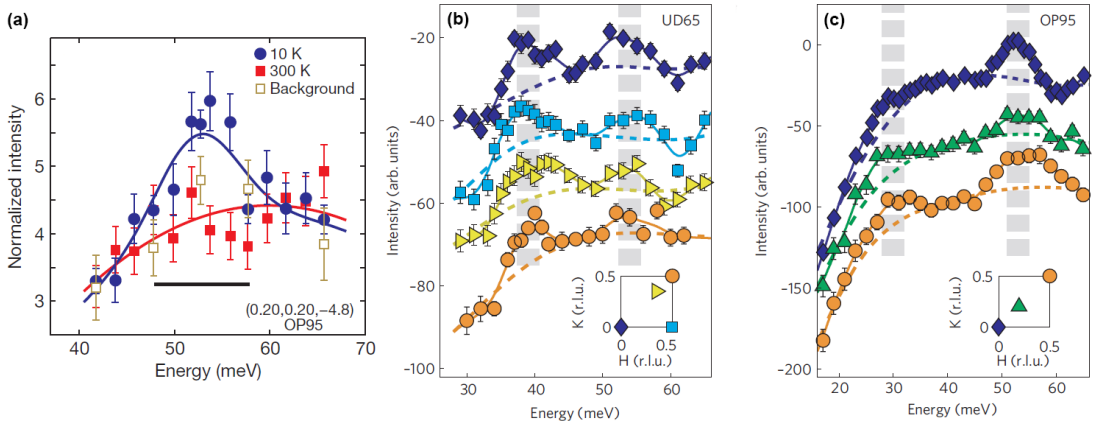

Figure 5.1: *Two Ising-like Modes [42, 43]. (a) Spin-flip energy scans at (0.2, 0.2, -4.8) for sample OP95. Background (open squares) at 10 K estimated using Equation 2.8 (see Section 2.2.2) together with data at 300 K (red squares) are approximated by a parabolic baseline (red line). The 10 K data are fitted to a Gaussian (blue line) above this baseline, with a small offset to allow for a possible background increase with temperature. (b) Intensity difference between 4 K and 330 K (top three) and between 4 K and 300 K (bottom) for UD65 at* $\mathbf{Q}$ *= (0 0 4.6), (0.5 0 4.6), (0.35 0.35 4.6) and (0.5 0.5 4.4), from top to bottom. The pseudogap temperature is* $T^* \approx 380$ *K for this sample [13]. (c) Intensity difference between 4 K and 230 K (top) and between 4 K and 200 K (bottom two) for OP95 at* $\mathbf{Q}$ *= (0 0 4.6), (0.2 0.2 4.4) and (0.5 0.5 4.4), from top to bottom. Data were measured on different spectrometers and rescaled for comparison. The pseudogap temperature is* $T^* \approx 200$ *K for this sample [13]. In (b) and (c), the lines are guides to the eye, and the data are offset for clarity (top data sets are without offset). The insets indicate the measured 2D momentum positions.*

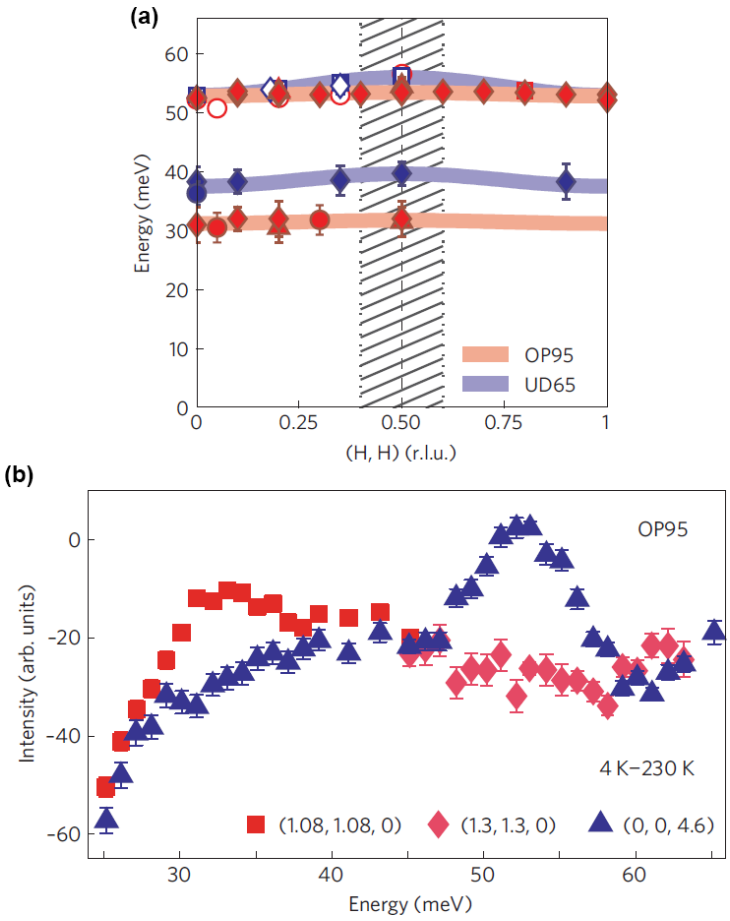

Figure 5.2: *Dispersion of the two Ising-like modes [42, 43]. (a) Dispersion along [H, H] of the two excitations observed for UD65 and OP95. Different symbols indicate on which spectrometers the measurements were performed (diamonds: IN8; circles: IN20; squares: PUMA; triangles: 2T). The hatched area indicates where antiferromagnetic spin fluctuations are expected (see Chapter 3). Error bars indicate the confidence range for the estimated energies. (b) Intensity difference between 4 K and 230 K from energy scans for OP95. The magnitudes of the momenta (1.3, 1.3, 0) and (0, 0, 4.6) are identical. The low-energy excitation is most prominent at* $\mathbf{Q}$ *= (0, 0, 4.6) and the high-energy excitation is most prominent at* $\mathbf{Q}$ *= (1.08, 1.08, 0).*

5.2 Systematic Study of the High-Energy Mode

5.2.1 Doping Dependence

As described in Section 5.1, previous measurements revealed two weakly dispersive modes in the Hg1201 UD65 and OP95 samples [42, 43]. A discrepency between the observation and the LC model explanation is that the high-energy mode is stronger in the OP95 sample (Figure 5.2(b)& (c)), whereas it should be weaker if the mode is strictly connected to the PG phase, which is less prominent as doping increases. In this Chapter, data for the high-energy mode at five additional doping levels (see Table 5.1) will be presented.

Table 5.1: *Seven samples measured in the study of the high-energy the Ising-like mode. The numbers in the sample name represent the respective T_c. UD65 and OP95 were studied previously [42, 43]. The UD45, UD55, UD71, UD88 and OV88 samples are newly studied in this Thesis. Doping levels are estimated from [55].*

Sample Name	Doping level p	Spectrometer	Sample Mass
UD45	0.057	ARCS	1.72g
UD55	0.064	IN8	2.0g
UD65	0.075	IN8	1.8g
UD71	0.090	ARCS	2.0g
UD88	0.115	2T	1.26g
OP95	0.127	ARCS, 2T, IN8	3.0g(ARCS) 2.0g (2T), 2.2g (IN8)
OV88	0.186	2T	1.45g

The measurements were performed on a number of different spectrometers: UD45, UD55 and UD71 were measured on the time-of-flight spectrometer ARCS at Oak Ridge National Laboratory (ORNL); UD65 and UD88 were measured on the triple-axis spectrometer IN8 at the Institut Laue-Langevin (ILL), France; OV88 was measured on the triple-axis spectrometer 2T at Laboratoire Léon Brillouin (LLB), France; OP95 was measured on all three spectrometers. The intensities were rescaled for quantitative

comparison among samples in the following way: all data were first rescaled by their mass in order to obtain the high-energy mode intensity per gram; then, the OP95 data measured on 2T and ARCS were normalized to the mode intensity on IN8; finally, the data for all other samples measured on 2T and ARCS were rescaled using the same scale factor as for OP95. We note that although the same in-plane momentum transfer $\mathbf{q} = (H, K) = (0.2, 0.2)$ was used, the L values are not always the same. UD45, UD55 and UD71 were measured on ARCS, so the L value is coupled to ω at fixed $\mathbf{q}$; for the other four samples, $L = 4.6$.

Data for the high-energy Ising-like mode for all measured samples are shown in Figure 5.3a-c. The doping dependence of the normalized mode intensity is shown in Figure 5.3d. In UD45, the mode is not dicernible within the error of the experiment. The mode strength increases almost linearly with doping, except for OV88, which exhibits very high intensity. Therefore, the strength of high-energy mode is anti-correlated with the strength of PG phase (T^* extrapolates to zero at $p \approx 0.20$).

5.2.2 Momentum Dependence

A detailed measurement of the momentum dependence of the Ising-like mode should provide constrains on its microscopic origin. In this Section, two aspects of the momentum dependence are shown. First, Figure 5.4a shows a strong peak for out-of-plane $\mathbf{Q} = (0\ 0\ 4.6)$, and the absence of the mode for in-plane $\mathbf{Q}$, indicating that the mode is polarized along the c-axis. Second, the L-dependence shown in Figure 5.4 follows a surprising non-monotonic L-dependence, with a broad maximum at $L \approx 8$ r.l.u. This unusual dependence does not match the magnetic form factor of either the IUC magnetic order or the Cu^{2+} $3d^9$ moment. The former falls off rather quickly with L, since the IUC magnetism is no longer discerned at (1 0 2) and (1 0 3) [39, 86]. The latter decreases monotonically with increasing $|\mathbf{Q}|$ and is specified in [48]. Therefore, the high-energy Ising-like mode does not appear to be purely magnetic. In fact, the strong L-dependence at low L values is reminiscent of the $|\mathbf{Q}|^2$ dependence of a c-axis polarized optic phonon mode. Even though the data in Figure 5.1a indicate a magnetic contribution, the mode must have dual magnetic and structure character.

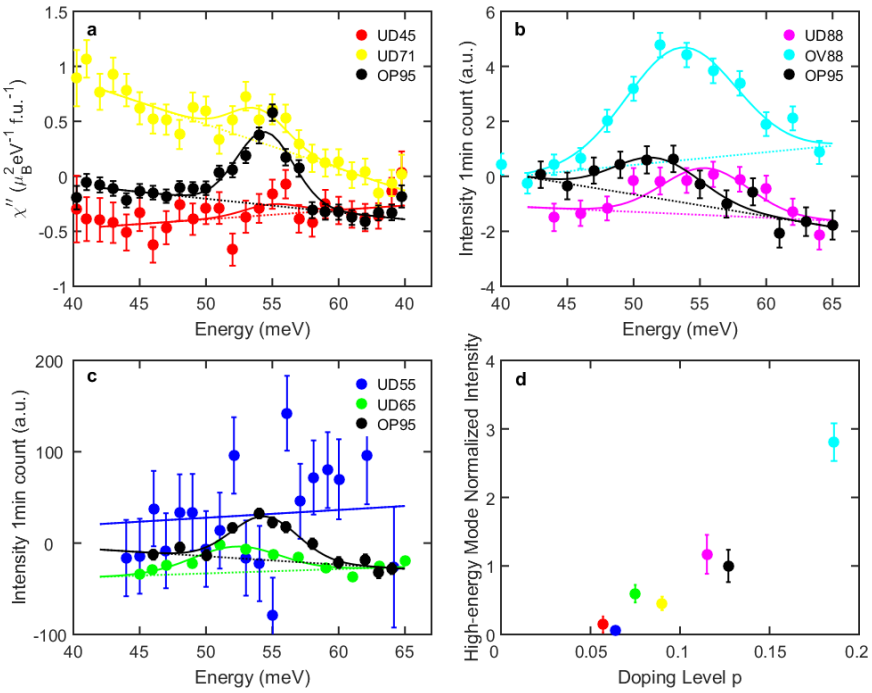

Figure 5.3: *Doping dependence of the high-energy Ising-like mode. (a)-(c) High-energy Ising-like mode for samples measured on (a) ARCS, (b) 2T and (c) IN8. Different colors represent different samples, as indicated. Solid lines are Gaussian fits to the data, and dashed lines are the estimated (linear) background. (d) Doping dependence of the normalized intensity of the fitted peak amplitude of the high-energy Ising-like mode, with the intensity of OP95 sample set to 1. Colors are the same as in (a)-(c). Data for OV88 (light blue) are scaled by a factor of 1/3 for better view.*

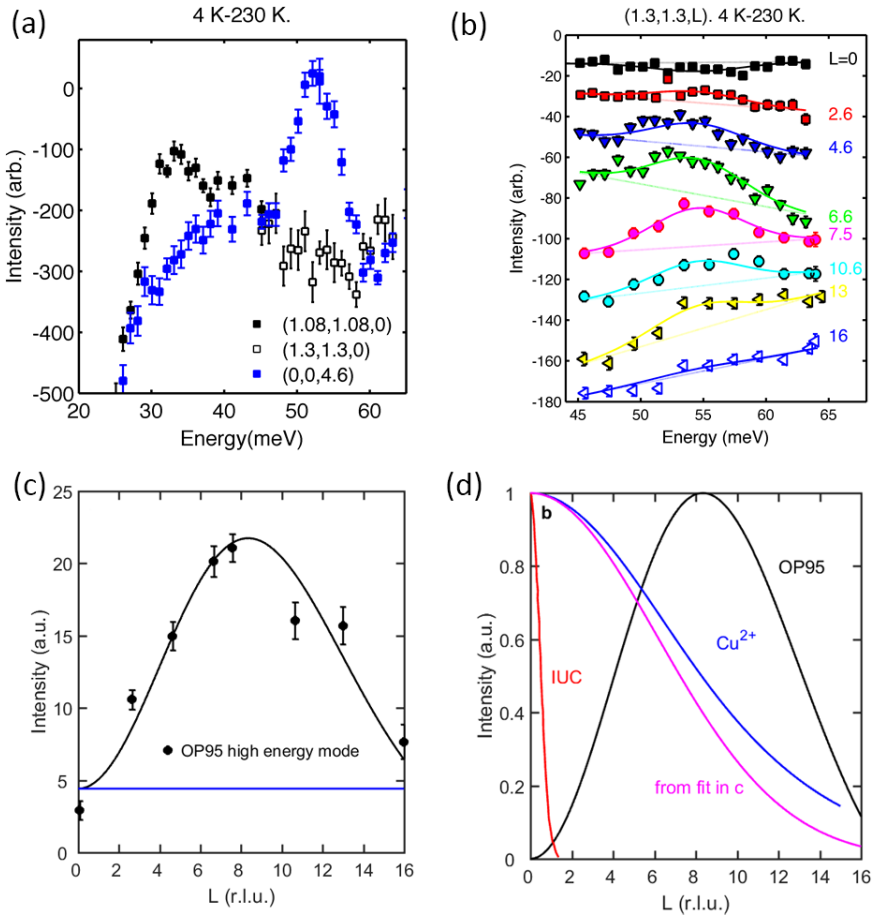

Figure 5.4: *Momentum dependence of the high-energy Ising-like mode in OP95. (a) Net intensity* $I\,(4K)$ - $I\,(230K)$ *of energy scans in the 20-65 meV range for different in-plane and out-of-plane momentum transfers (same data as in Figure 5.2b). The Ising-like mode at* $\sim$ *55 meV is only observed if* $\mathbf{Q}$ *has a non-zero out-of-plane component L. For OP95,* T^* $\approx$ *200 K. As demonstrated in Figure 5.1a, the mode is not discernible above* T^**. (b) Net intensity for* $\mathbf{Q}$ = *(1.3, 1.3, L) measured at L values in the range from 0 to 16. Solid lines are Gaussian fits to the data with a linear background (dashed lines). (c) L-dependence of the magnitude of the Gaussian amplitudes from the fits in (b). Black line is a fit to the heuristic function* $I = \left(AL^2 + B\right) \times e^{-\frac{L^2}{FWHM^2}} + BG$*, where* $A = 0.72$*,* $B = 4.45$*, and* $FWHM = 14.5$*, center of Gaussian is fixed to be at zero, BG the background as indicated by blue solid line. (d) Comparison of the estimated L-dependence of the IUC magnetic order (blue, see Chapter 4), the* Cu^{2+} $3d^9$ *magnetic form factor [48], and of the Ising-like mode, with their maxima normalized to 1.*

5.2.3 Microscopic Origin

The high-energy Ising-like mode behaves strangely. It has dual magnetic and structural character, an unusual momentum dependence, and its strength is anti-correlated with the PG phase. It is clear that loop currents cannot generate such a mode. We now consider several scenarios to attempt to explain its microscopic origin.

1. *Vibration of H or Hg atoms.* Let us first consider vibrations of atoms that have strong magnetic neutron scattering cross sections, which would be either H or Hg in Hg1201. The samples may contain hydrogen as a result of the growth process, as H_2O molecules may enter the system. The possibility of H atom vibrations was examined by re-annealing the UD45 sample, where the mode was found to be absent (data in Figure 5.3a), to UD88 in a water-free oxygen atmosphere. Our subsequent measurement of this new UD88 sample (Figure 5.3(b)) indicated the re-appearance of the high-energy mode, which rules out the possibility of spurious effects due to hydrogen. On the other hand, the cross section for a local vibrational mode of Hg can be estimated via [116]:

$$\left(\frac{d^2\sigma}{d\Omega d\omega}\right)_{incoherent}^{inelastic} = \frac{k_f}{k_i}\sum_d \left(\overline{|b_d|^2} - |\overline{b_d}|^2\right) e^{-2W_d(\kappa)} \frac{1}{M_d}\sum_{j,q} |\kappa\sigma_d^j(\mathbf{q})|^2 S_j(\mathbf{q},\omega) \tag{5.1}$$

where d corresponds to the d^{th} atom (in this case, we only consider Hg), the exponential term is the Debye-Waller factor (which is neglected in our estimation), the effective incoherent scattering length $\overline{|b_d|^2} - |\overline{b_d}|^2$ can be expressed as $\frac{\sigma_{inc}}{4\pi}$ (where $\sigma_{inc} = 6.6$ barns for Hg), and M_d is the atomic mass of Hg (200.59 g/mol). We simply rewrite the structure factor $S(\mathbf{q},\omega)$ as $\frac{1}{2\omega_0}\delta(\omega-\omega_0)$, so Equation 5.1 changes to:

$$\left(\frac{d^2\sigma}{d\Omega d\omega}\right)_{incoherent}^{inelastic} = \frac{\sigma_{inc}}{4\pi}\frac{1}{M_{Hg}}|\mathbf{Q}|^2\frac{1}{2\omega_0}\delta(\omega-\omega_0) \tag{5.2}$$

where ω_0 is the characteristic energy of high-energy mode. Inserting each quantity on the right side, we estimate about 0.86 mbarn for the cross section of a vibrational Hg mode, which is far below the observed value at higher doping (about 5

mbarn). Moreover, the Hg atom is very heavy, which does not favor a mode with such a high excitation energy. Therefore, the possibility of Hg atom vibration is also ruled out.

2. *Multiple scattering.* We now consider multiple scattering [117] as a potential explanation of the high-energy Ising-like mode. One would need a magnetic scattering process from a magnetic Ising-like mode (e.g., generated by the LC) as well as a non-magnetic incoherent elastic scattering process. Let us consider the **Q** dependence of such scattering process and assume that the magnetic and non-magnetic incoherent scattering cross sections are simply:

$$S_{mag}(Q,\omega) = I_{mag}\delta(\omega-\omega_0)\, e^{-AQ^2}, \tag{5.3}$$

$$S_{inc}(Q,\omega) = I_{inc}\delta(\omega)\, e^{-BQ^2}, \tag{5.4}$$

where I_{mag} and I_{inc} are energy- and momentum-independent scattering cross sections, ω_0 the mode energy, and A and B are coefficients. The exponential term e^{-AQ^2} describes the magnetic form factor, and e^{-BQ^2} is the Debye-Waller factor, both with isotropic Q-dependence for simplicity. When both are taken into consideration, the total cross section is given by (considering energy and momentum conservation):

$$\begin{aligned} S_{tot}(Q,\omega) &= \int_{-\infty}^{\infty} \delta(Q-Q_1-Q_2)\,\delta(\omega-\omega_1-\omega_2) \\ &\quad \times S_{mag}(Q_1,\omega_1)\, S_{inc}(Q_2,\omega_2)\, d^3Q_1 d^3Q_2 d\omega_1 d\omega_2 \end{aligned} \tag{5.5}$$

which simplifies to:

$$S_{tot}(Q,\omega) = I_{inc}I_{mag}\delta(\omega,\omega_0)\, e^{-\frac{AB}{A+B}Q^2} \tag{5.6}$$

The momentum dependent part still has factor of e^{-Q^2}, which cannot explain the observed non-monotonic L-dependence. On the other hand, a c-axis polarized

phonon, which would have $\propto\ L^2$ dependence, in combination with elastic incoherent magnetic scattering that follows $|f(\mathbf{Q})|^2\ \propto\ e^{-CQ^2}$, might account for the observed scattering.

3. *Oxygen-related bosonic mode.* An STM measurement of Bi2212 observed a local bosonic mode that displays an energy shift upon exchange ^{16}O by ^{18}O (see Figure 5.5a) [118]. Such a mode was also proposed to be a candidate for the pairing glue in cuprates [118]. We compare the energy scale of the bosonic mode in Bi2212 with the high- energy mode in Hg1201 OP95 in Figure 5.5a, and find agreement between the two, indicative of an underlying connection. We then annealed a T_c = 87 K sample (denoted UD87) in an ^{18}O atmosphere, and measured the high-energy mode. The result in comparison with those for OP95 and UD88 samples (which had only ^{16}O) are shown in Figure 5.5b. Unfortunately, we did not observe an energy shift in the ^{18}O exchanged sample. This is inconsistent with the STM bosonic mode measurements. However, it could be the case that the isotope exhange was incomplete, so further tests are needed.

4. *Vibration of oxygen chains.* It has been known that the interstitial oxygen atoms forms Cu-O chains in the YBCO system [119]. In Hg1201, oxygen chains are also observed, but have a different origin [120]. Our Hg1201 crystals exhibit Hg vacancies [50] and, in unpublished work, we have found that these Hg vacancies form chains with typical lengths of about 10-20 lattice constants. This was documented by synchrotron X-ray scattering [120] and transmission electron microscopy (TEM). The X-ray data are consistent with the formation of molecular oxygen within the Hg vacancy chains. Molecular oxygen is magnetic [121]. Therefore, a magneto-vibrational mode of molecular oxygens in the oxygen chain might potentially explain the strange **Q**-dependence of the high-energy mode. The X-ray data demonstrate that this peculiar ordering phenomenon in the Hg-O layer increases in strength as oxygen/hole doping increases, which is qualitatively consistent with the doping dependence of the high-energy mode (Figure 5.3).

In summary, we have demonstrated that the high-energy Ising-like mode in Hg1201 is not associated with the PG phenomenon. Instead, it appears to be a peculiarity of the Hg1201 system, possibly associated with Hg vacancy or O_2 chain formation. This does

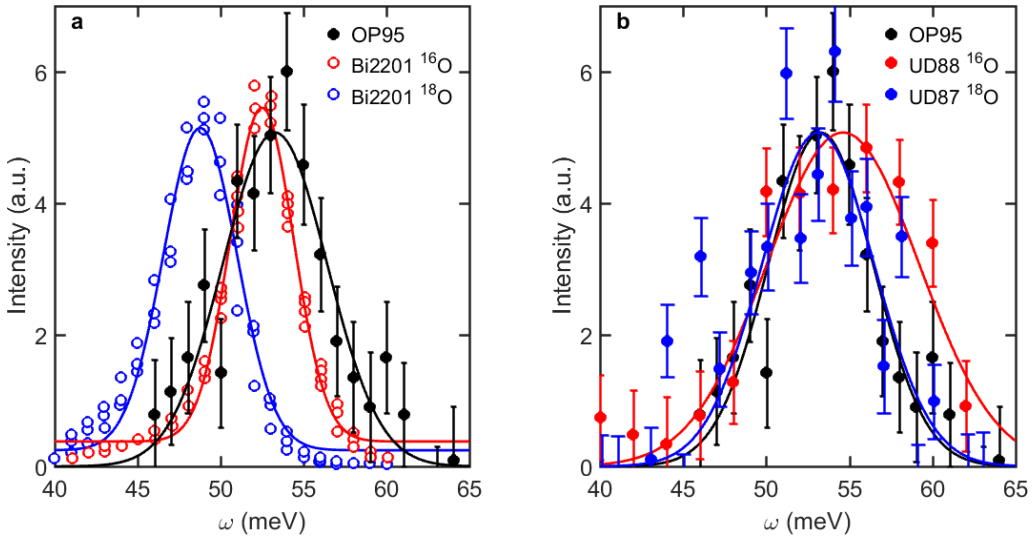

Figure 5.5: *Bosonic mode in Bi2212 and isotope exchange results for Hg1201 OP95. (a) Bosonic mode determined from STM with ^{16}O (red) and ^{18}O (blue) in the Bi2212 system [118], and the high-energy mode in Hg1201 OP95 sample with ^{16}O (black). Solid lines are Gaussian fits to the data, with centers at 48.8 meV, 52.5 meV and 53.3 meV for Bi2212 (^{16}O), Bi2212 (^{18}O) and Hg1201 OP95 (^{16}O), respectively. There exists a remarkably correspondence between the Bi2212 (^{16}O) and Hg1201 OP95 (^{16}O) results, both for the center and the width of the observed modes. (b) High-energy mode measured in Hg1201 OP95 (^{16}O, black), UD88 (^{16}O, red) and UD87 (^{18}O, blue), OP95 and UD87 were measured on IN8 at the ILL, and UD88 was measured on 2T at the LLB. Solid lines are fits to a Gaussian, with centers 53.5 meV, 54.6 meV and 53.1 meV for OP95, UD88 and UD87, respectively. No obvious isotope effect is seen. We can not rule out at this time that only a small portion of ^{16}O was replaced by ^{18}O.*

not rule out the possibility that the low-energy Ising-like mode, whose energy decreases with increasing doping (Figure 5.2a), is indeed associated with the PG phenomenon.

References

[1] H. Kamerlingh Onnes, *Comm. Phys. Lab. Univ. Leiden* No. 122b (1911)

[2] W. Meissner and R. Ochsenfeld, *Naturwissenschaften* **21**, 787 (1933)

[3] https://commons.wikimedia.org

[4] J. Bardeen, L. N. Cooper, and J. R. Schrieffer, *Phys. Rev.* **108**, 1175 (1957)

[5] N. Ashcroft, *Phys. Rev. Lett.* **21**, 1748 (1968)

[6] A. P. Drozdov, M. I. Eremets, I. A. Troyan, V. Ksenofontov, and S. I. Shylin, *Nature* **525**, 73 (2015)

[7] B. Keimer, S. A. Kivelson, M. R. Norman, S. Uchida, and J. Zaanen, *Nature* **518**, 179 (2015)

[8] J. G. Bednorz and K. Müller, *Z. Phys. B* **64**,189 (1986)

[9] P. J. Ray, *Master Thesis*, University of Copenhagen (2015)

[10] M. Nuñez-Regueiro, J. -L. Tholence, E. V. Antipov, J. -J. Capponi, and M. Marezio *Science* **262**, 5130 (1993)

[11] H. Eisaki, N. Kaneko, D. L. Feng, A. Damascelli, P. K. Mang, K. M. Shen, Z.-X. Shen, and M. Greven, *Phys. Rev. B* **69**, 064512 (2004)

[12] J. Haase, D. Rybicki, C.P. Slichter, M. Greven, G. Yu, Y. Li, and X. Zhao, *Phys. Rev. B* **85**, 104517 (2012)

[13] N. Barišić, M. K. Chan, Y. Li, G. Yu, X. Zhao, M. Dressel, A. Smontara, and M. Greven, *Proc. Nat. Acad. Sci.* **110**, 12235 (2013)

[14] S. I. Mirzaei, D. Stricker, J. N. Hancock, C. Berthod, A. Georges, E. van Heumen, M. K. Chan, X. Zhao, Y. Li, M. Greven, N. Barišić, and D. van der Marel, *Proc. Natl. Acad. Sci.* **110**, 5774 (2013)

[15] N. Barišić, S. Badoux, M. K. Chan, C. Dorow, W. Tabis, B. Vignolle, G. Yu, J. Béard, X. Zhao, C. Proust, and M. Greven, *Nat. Phys.* **9**, 761 (2013)

[16] M. K. Chan, M. J. Veit, C. J. Dorow, Y. Ge, Y. Li, W. Tabis, Y. Tang, X. Zhao, N. Barišić, and M. Greven, *Phys. Rev. Lett.* **113**, 177005 (2014)

[17] J. Zaanen, G. A. Sawatzky, and J. W. Allen *Phys. Rev. Lett.* **55**, 418 (1985)

[18] N. Ashcroft and N. D. Mermin, *Solid State Physics*, ISBN 0-03-083993-9

[19] L. F. Mattheiss, *Phys. Rev. Lett.* **58**, 1028 (1987)

[20] V. J. Emery, *Phys. Rev. Lett.* **58**, 2794 (1987)

[21] P. W. Anderson, *Science* **235**, 1196 (1987)

[22] F. C. Zhang and T. M. Rice, *Phys. Rev. B* **37**, 3759 (1988)

[23] A. Damascelli, Z. Hussain, and Z.-X. Shen *Rev. Mod. Phys.* **75**, 473 (2003)

[24] E. Fradkin, *Field Theories of Condensed Matter Physics*, Cambridge University Press (2013)

[25] D. J. Scalapino, *Rev. Mod. Phys.* **84**, 1383 (2012)

[26] S. Nakajima, *Prog. Theor. Phys.* **50**, 1101-1109 (1973)

[27] R. J. Birgeneau, C. Stock, J. M. Tranquada, and K. Yamada, *J. Phys. Soc. Jpn.* **75**, 111003 (2006)

[28] M. Fujita, H. Hiraka, M. Matsuda, M. Matsuura, J. M. Tranquada, S. Wakimoto, G. Xu, and K. Yamada, *J. Phys. Soc. Jpn.* **81**, 011007 (2012).

[29] Y. Sidis, S. Pailhès, V. Hinkov, B. Fauqué, C. Ulrich, L. Capogna, A. Ivanov, L.-P. Regnault, B. Keimer, and P. Bourges, *C. R. Physique* **8**, 745 (2007)

[30] A. Allais, J. Bauer, and S. Sachdev, *Phys. Rev. B* **90**, 155114 (2014)

[31] Y. Wang and A. Chubukov, *Phys. Rev. B* **90**, 035149 (2014)

[32] E. Abrahams, *Int. J. Mod. Phys. B* **24**(20-21), 4150-4180 (2010)

[33] C. M. Varma, *Phys. Rev. B* **55**, 14554 (1997)

[34] C. M. Varma, *Phys. Rev. B* **73**, 155113 (2006)

[35] M. Fechner, M. J. A. Fierz, F. Th ole, U. Staub and N. A. Spaldin, *Phys. Rev. B* **93**, 174419 (2016)

[36] S. W. Lovesey, D. D. Khalyavin, and U. Staub, *J. Phys. Cond. Mat.* **27**, 292201 (2015)

[37] S. W. Lovesey and D. D. Khalyavin, *J. Phys. Cond. Mat.* **29**, 215603 (2017)

[38] B. Fauqué, Y. Sidis, V. Hinkov, S. Pailhès, C. T. Lin, X. Chaud, and P. Bourges, *Phys. Rev. Lett.* **96**, 197001 (2006)

[39] Y. Li, V. Balédent, N. Barišić, Y. Cho, B. Fauqué, Y. Sidis, G. Yu, X. Zhao, P. Bourges, and M. Greven, *Nature (London)* **455**, 372 (2008)

[40] Y. He and C. M. Varma, *Phys. Rev. Lett.* **106**, 147001 (2011)

[41] Y. He and C. M. Varma, *Phys. Rev. B* **85**, 155102 (2012)

[42] Y. Li, V. Balédent, G. Yu, N. Barišić, K. Hradil, R.A. Mole, Y. Sidis, P. Steffens, X. Zhao, P. Bourges, and M. Greven *Nature* **468**, 283 (2010)

[43] Y. Li, G. Yu, M.K. Chan, V. Balédent, Y. Li, N. N. Barišić, K. Hradil, R.A. Mole, Y. Sidis, P. Steffens, X. Zhao, P. Bourges, and M. Greven, *Nat. Phys.* **8**, 404 (2012)

[44] C. G. Shull, W. A. Strauser, and E. O. Wollan, *Phys. Rev.* **83**, 333 (1951)

[45] C. C. Wilson and D. A. Myles, *Single Crystal Neutron Diffraction and Protein Crystallography* Springer, (2006)

[46] A. Senyshyn, M. J. Mühlbauer, K. Nikolowski, T. Pirling, and H. Ehrenberg, *J. Power Sources* **203**, 126-129 (2012)

[47] G. Shirane, S. M. Shapiro, and J. M. Tranquada, *Neutron Scattering with a Triple-Axis Spectrometer*, Cambridge University Press (2002)

[48] A.-J. Dianoux and G. Lander, Neutron Data Booklet, Institute Laue Langevin (2003)

[49] E. V. Antipov, A. M. Abakumov, and S. N. Putilin *Supercond. Sci. Technol.* **15**, R31 (2002)

[50] X. Zhao, G. Yu, Y. Cho, G. Chabot-Couture, N. Barii, P. Bourges, N. Kaneko, Y. Li, L. Lu, E. M. Motoyama, O. P. Vajk, and M. Greven, *Adv. Mater.* **18**, 3243 (2006)

[51] L. Wang, X. Luo, J. Li, J. Zeng, M. Cheng, J. Freyermuth, Y. Tang, B. Yu, G. Yu, M. Greven, and Y. Li, arXiv:1807.08954

[52] F. Schwabl, R. Hilton, and A. Lahee, *Advanced Quantum Mechanics*, Springer (2010)

[53] D. Vaknin, S. K. Sinha, D. E. Moncton, D. C. Johnston, J. M. Newsam, C. R. Safinya, and J. H. E. King, *Phys. Rev. Lett.* **58**, 2802 (1987)

[54] G. Shirane, Y. Endoh, R. J. Birgeneau, M. A. Kastner, Y. Hidaka, M. Oda, M. Suzuki, and T. Murakami, *Phys. Rev. Lett.* **59**, 1613 (1987)

[55] A. Yamamoto, W.-Z. Hu, and S. Tajima, *Phys. Rev. B* **63**, 024504 (2000)

[56] Paul C. Canfield, *Nat. Mater.* **10**, 259261 (2011)

[57] R. Coldea, S. M. Hayden, G. Aeppli, T. G. Perring, C. D. Frost, T. E. Mason, S.-W. Cheong, and Z. Fisk, *Phys. Rev. Lett.* **86**, 5377 (2001)

[58] M. Enoki, M. Fujita, T. Nishizaki, S. Iikubo, D. K. Singh, S. Chang, J. M. Tranquada, and K. Yamada, *Phys. Rev. Lett.* **110**, 017004 (2013)

[59] C. Stock, W. J. L. Buyers, R. A. Cowley, P. S. Clegg, R. Coldea, C. D. Frost, R. Liang, D. Peets, D. Bonn, W. N. Hardy, and R. J. Birgeneau, *Phys. Rev. B* **71**, 024522 (2005)

[60] V. Hinkov, B. Keimer, A. Ivanov, P. Bourges, Y. Sidis, and C. D. Frost, arXiv:1006.3278

[61] J. M. Tranquada, B. J. Sternlieb, J. D. Axe, Y. Nakamura and S. Uchida, *Nature* **375**, 561563 (1995)

[62] E. Demler and S. C. Zhang, *Nature* **396**, 733 (1998)

[63] J. Rossat-Mignod, L. P. Regnault, C. Vettier, P. Bourges, P. Burlet, J. Bossy, J. Y. Henry, and G. Lapertot, *Physica C* **86**, 185 (1991)

[64] P. Bourges, Y. Sidis, H. F. Fong, L. P. Regnault, J. Bossy, A. Ivanov, and B. Keimer, *Science* **288**, 1234 (2000)

[65] H. F. Fong, P. Bourges, Y. Sidis, L. P. Regnault, A. S. Ivanov, G. D. Gu, N. Koshizuka, and B. Keimer, *Nature* **398**, 588 (1999)

[66] H. He, P. Bourges, Y. Sidis, C. Ulrich, L.P. Regnault, S. Pailhès, N.S. Berzigiarova, N.N. Kolesnikov, and B. Keimer, *Science* **295**, 1045 (2002)

[67] G. Yu, Y. Li, E. M. Motoyama, X. Zhao, N. Barišić, Y. Cho, P. Bourges, K. Hradil, R. A. Mole, and M. Greven, *Phys. Rev. B* **81**, 064518 (2010)

[68] G. Yu, Y. Li, E. M. Motoyama and M. Greven, *Nat. Phys.* **5**, 873 (2009)

[69] K. Yamada, S. Wakimoto, G. Shirane, C. H. Lee, M. A. Kastner, S. Hosoya, M. Greven, Y. Endoh, and R. J. Birgeneau, *Phys. Rev. Lett.* **75**, 1626 (1995)

[70] D. Haug, V. Hinkov, Y. Sidis, P. Bourges, N. B. Christensen, A. Ivanov, T. Keller, C. T. Lin and B. Keimer, *New J. Phys.* **12**, 105006 (2010)

[71] V. Hinkov, D. Haug, B. Fauque, P. Bourges, Y. Sidis, A. Ivanov, C. Bernhard, C. T. Lin, and B. Keimer, *Science* **319**, 597 (2008).

[72] W. Tabis, Y. Li, M. Le Tacon, L. Braicovich, A. Kreyssig, M. Minola, G. Dellea, E. Weschke, M. J. Veit, M. Ramazanoglu, A. I. Goldman, T. Schmitt, G. Ghiringhelli, N. Barišić, M. K. Chan, C. J. Dorow, G. Yu, X. Zhao, B. Keimer, and M. Greven, *Nat. Commun.* **5**, 5875 (2014)

[73] W. Tabis, B. Yu, I. Bialo, M. Bluschke, T. Kolodziej, A. Kozlowski, E. Blackburn, K. Sen, E. M. Forgan, M. v. Zimmermann, Y. Tang, E. Weschke, B. Vignolle, M. Hepting, H. Gretarsson, R. Sutarto, F. He, M. Le Tacon, N. Barišić, G. Yu, and M. Greven, *Phys. Rev. B* **96**, 134510 (2017)

[74] K. B. Efetov, H. Meier and C. Pépin, *Nat. Phys.* **9**, 442 (2013)

[75] W. A. Atkinson, A. P. Kampf, and S. Bulut, *New J. Phys.* **17**, 013025 (2015)

[76] H. Eisaki, N. Kaneko, D. L. Feng, A. Damascelli, P. K. Mang, K. M. Shen, Z.-X. Shen, and M. Greven, *Phys. Rev. B* **69**, 064512 (2004)

[77] N. Barišić, Y. Li, X. Zhao, Y. C. Cho, G. Chabot-Couture, G. Yu, and M. Greven, *Phys. Rev. B* **78**, 054518 (2008)

[78] M. K. Chan, C. J. Dorow, L. Mangin-Thro, Y. Tang, Y. Ge, M. J. Veit, G. Yu, X. Zhao, A. D. Christianson, J. T. Park, Y. Sidis, P. Steffens, D. L. Abernathy, P. Bourges, and M. Greven, *Nat. Commun.* **7**, 10819 (2016)

[79] M. K. Chan, Y. Tang, C. J. Dorow, J. Jeong, L. Mangin-Thro, M. J. Veit, Y. Ge, D. L. Abernathy, Y. Sidis, P. Bourges, and M. Greven, *Phys. Rev. Lett.* **117**, 277002 (2016)

[80] M. Fujita, K. Yamada, H. Hiraka, P. M. Gehring, S. H. Lee, S. Wakimoto, and G. Shirane, *Phys. Rev. B* **65**, 064505 (2002)

[81] F. Onufrieva, *Phys. Rev. B* **95**, 125110 (2017)

[82] Unpublished results.

[83] A. Kaminski, S. Rosenkranz, H. M. Fretwell, J. C. Campuzano, Z. Li, H. Raffy, W. G. Cullen, H. You, C. G. Oison, C. M. Varma, and H. Hchst, *Nature (London)* **416**, 610 (2002)

[84] H. A. Mook, Y. Sidis, B. Fauqué, V. Balédent, and P. Bourges, *Phys. Rev. B* **78**, 020506 (2008)

[85] V. Balédent, B. Fauqué, Y. Sidis, N. B. Christensen, S. Pailhs, K. Conder, E. Pomjakushina, J. Mesot, and P. Bourges, *Phys. Rev. Lett.* **105**, 027004 (2010)

[86] Y. Li, V. Balédent, N. Barišić, Y. C. Cho, Y. Sidis, G. Yu, X. Zhao, P. Bourges, and M. Greven, *Phys. Rev. B* **84**, 224508 (2011)

[87] P. Bourges and Y. Sidis, *C. R. Physique* **12**, 461 (2011)

[88] L. Mangin-Thro, Y. Sidis, P. Bourges, S. De Almeida-Didry, F. Giovannelli, and I. Laffez-Monot, *Phys. Rev. B* **89**, 094523 (2014)

[89] L. Mangin-Thro, Y. Sidis, A. Wildes, and P. Bourges, *Nat. Commun.* **6**, 7705 (2015)

[90] L. Mangin-Thro, Yuan Li, Y. Sidis, and P. Bourges, *Phys. Rev. Lett.* **118**, 097003 (2017)

[91] P. Bourges, Y. Sidis, and L. Mangin-Thro, *Phys. Rev. B* **96**, 214504 (2017)

[92] J. Xia, E. Schemm, G. Deutscher, S. A. Kivelson, D. A. Bonn, W. N. Hardy, R. Liang, W. Siemons, G. Koster, M. M. Fejer, and A. Kapitulnik, *Phys. Rev. Lett.* **100**, 127002 (2008)

[93] A. Shekhter, B. J. Ramshaw, R. X. Liang, W. H. Hardy, D. A. Bonn, F. F. Balakirev, R. D. McDonald, J. B. Betts, S. C. Riggs, and A. Migliori, *Nature* **498**, 75-77 (2013)

[94] Y. Lubashevsky, L. Pan, T. Kirzhner, G. Koren, and N.P. Armitage, *Phys. Rev. Lett.* **112**, 147001 (2014).

[95] L. Zhao, C. A. Belvin, R. Liang, D. A. Bonn, W. N. Hardy, N. P. Armitage, and D. Hsieh. *Nat. Phys.* **13**, 250 (2017)

[96] H. Murayama, Y. Sato, S. Kasahara, Y. Mizukami, Y. Kasahara, H. Uchiyama, A.Yamamoto, E.-G.Moon, J. Cai, J. Freyermuth, M. Greven, T. Shibauchi, and Y. Matsuda, arXiv:1805.00276v1

[97] Y. Sato, S. Kasahara, H. Murayama, Y. Kasahara, E.-G. Moon, T. Nishizaki, T. Loew, J. Porras, B. Keimer, T. Shibauchi, and Y. Matsuda, *Nature Physics* **13**, 1074 (2017)

[98] J. Zhang, Z. F. Ding, C. Tan, K. Huang, O. O. Bernal, P.-C. Ho, G. D. Morris, A. D. Hillier, P. K. Biswas, S. P. Cottrell, H. Xiang, X. Yao, D. E. MacLaughlin, and L. Shu, *Sci. Adv.*, **4**, 5235 (2018)

[99] A. Pal, S.R. Dunsiger, K. Akintola, A. Fang, A. Elhosary, M. Ishikado, H. Eisaki, and J. E. Sonier, *Phys. Rev. B* **97**, 060502 (2018)

[100] C. Weber, T. Giamarchi, and C. M. Varma, *Phys. Rev. Lett.* **112**, 117001 (2014)

[101] Y. He and C.M. Varma, *Phys. Rev. B* **86**, 035124 (2012)

[102] C. M. Varma, *J. Phys.: Condens. Matter*, **26**, 505701 (2014)

[103] S. Chatterjee and S. Sachdev, *Phys. Rev. B* **95**, 205133 (2017)

[104] D. F. Agterberg, Drew S. Melchert, and M. K. Kashyap, *Phys. Rev. B* **91**, 054502 (2015)

[105] C. Morice, D. Chakraborty, X. Montiel, and C. Pépin, arXiv:1707.08497

[106] J. W. Alldredge, K. Fujita, H. Eisaki, S. Uchida, and K. McElroy, *Phys. Rev. B* **87**, 104520 (2013)

[107] J.W. Loram, K.A. Mirza, J.R. Cooper, and W.Y. Liang, *Phys. Rev. Lett.* **71**, 1740 (1993)

[108] D. Pelc, P. Popčević, G. Yu, M. Požek, M. Greven, and N. Barišić, arXiv:1710.10221

[109] Y. Li, *PhD Thesis*, Stanford University (2010)

[110] S. De Almeida-Didry, Y. Sidis, V. Balédent, F. Giovannelli, I. Monot-Laffez, and P. Bourges, *Phys. Rev. B* **86**, 020504 (2012)

[111] S. Di Matteo and M. Norman, *Phys. Rev. B* **85**, 253143 (2012)

[112] C. Weber, A. Luchli, F. Mila, and T. Giamarchi, *Phys. Rev. Lett.* **102**, 017005 (2009)

[113] S. Lederer and S. A. Kivelson, *Phys. Rev. B* **85**, 155130 (2012)

[114] V. M. Yakovenko, *Physica B* **460**, 159 (2015)

[115] Y. He and C. M. Varma, *Phys. Rev. B* **86**, 035124 (2012)

[116] L. Mangin-Thro and P. Bourges, *private consideration*

[117] I. A. Blech and B. L. Averbach, *Phys. Rev.* **137**, A1113 (1965)

[118] J. Lee, K. Fujita, K. McElroy, J. A. Slezak, M. Wang, Y. Aiura, H. Bando, M. Ishikado, T. Masui, J.-X. Zhu, A. V. Balatsky, H. Eisaki, S. Uchida, and J. C. Davis, *Nature* **422**, 546-550 (2006)

[119] H. W. Seo, Q. Y. Chen, M. N. Iliev, Tom H. Johansen, N. Kolev, U. Welp, C. Wang, and W.-K. Chu, *Phys. Rev. B* **72**, 052501 (2005)

[120] G. Chabot-Couture, *PhD Thesis*, Stanford University (2010)

[121] G. C. DeFotis, *Phys. Rev. B* **23**, 4714 (1981)